

**INVESTIGATION OF PLASMAS SUSTAINED BY HIGH REPETITION
RATE SHORT PULSES WITH APPLICATIONS TO LOW NOISE
PLASMA ANTENNAS**

by

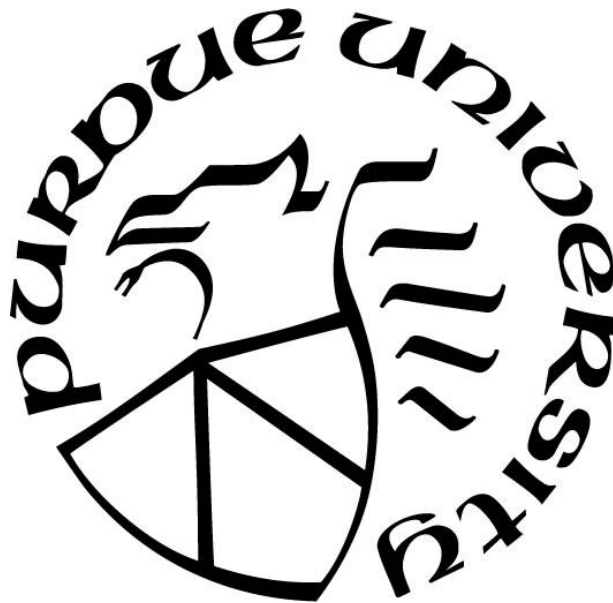
Vladlen A. Podolsky

A Dissertation

Submitted to the Faculty of Purdue University

In Partial Fulfillment of the Requirements for the degree of

Doctor of Philosophy



School of Aeronautics and Astronautics

West Lafayette, Indiana

December 2019

THE PURDUE UNIVERSITY GRADUATE SCHOOL

STATEMENT OF COMMITTEE APPROVAL

Dr. Sergey Macheret, Chair

School of Aeronautics and Astronautics

Dr. Alexey Shashurin

School of Aeronautics and Astronautics

Dr. Allen Garner

School of Nuclear Engineering

Dr. Dimitrios Peroulis

School of Electrical and Computer Engineering

Approved by:

Dr. Gregory A. Blaisdell

To my family

ACKNOWLEDGMENTS

I would first like to thank my advisor, Dr. Sergey Macheret, for his guidance and support in my research, academic, and professional endeavors during my time at Purdue. His passion for research and plethora of ideas always engaged and excited me throughout my Ph.D. I must also thank Dr. Andrei Khomenko and Dr. Alexey Shashurin for sharing their experimental knowledge and instilling in me good research practices. All the work with the plasma antenna could not have happened without the help of Dr. Abbas Semnani. Moreover, a big thank you to Dr. Anthony Cofer for his aid in setting up our lab during my early years at Purdue. I would also like to thank Dr. Allen Garner for his guidance in my research and professional career.

These past four years would not have been possible without the wonderful friends I have made at Purdue. I will always remember the good times we had at our dinners and nights out, the times spent with the Magnificent Seven studying for quals, and the support received whenever it was needed. You all helped keep me sane and driven.

Lastly, I would be remiss to not thank my wife Lida for the love and encouragement that she provides every day. You are always willing to listen and remind me of the things for which I should be grateful. Your patience with me throughout the most hectic years of my Ph.D. is truly saintly. I will fondly and happily remember our time at Purdue together (and with Maisy).

This work was supported by the National Science Foundation under Grant No. ECCS-1619547.

TABLE OF CONTENTS

LIST OF TABLES	8
LIST OF FIGURES	9
ABSTRACT.....	16
1. INTRODUCTION	19
1.1 Background.....	19
1.1.1 Plasma Antenna Sources.....	22
1.1.2 Brief Overview of Surface Waves.....	24
1.2 Motivation.....	27
2. DIAGNOSTICS OF NANOSECOND PULSED PLASMA.....	32
2.1 General Facility Development	32
2.2 Voltage and Current Measurements.....	33
2.3 Microwave Interferometry System	35
2.4 Experiment Results and Discussion.....	38
3. KINETIC MODELING	45
3.1 Kinetic Model Introduction.....	45
3.2 Model Description	46
3.3 Electron Energy Equation	48
3.4 Continuity Equation	52
3.4.1 Rate Equations	53
3.4.2 Solving the Balance Equations	56
3.5 Results and Discussion	57
3.5.1 Electron Temperature Decay	58

3.5.2	Comparison to Experimental Data.....	60
3.6	Conclusion	66
4.	CONDUCTIVITY AND PERMITTIVITY IN THE PLASMA AFTERGLOW.....	67
4.1	Model Description	67
4.2	Results and Discussion	68
5.	COST OF IONIZATION.....	72
5.1	Introduction.....	72
5.2	Experimental setup.....	75
5.2.1	Determining Uncertainty	81
5.3	Results and Discussion	82
5.3.1	RGA Analysis	82
5.3.2	Voltage and Current Measurements	82
5.3.3	Energy Deposited and Measured Change in Electron Density.....	88
5.3.4	Cost of Ionization	97
5.4	Conclusion	103
6.	PLASMA SUSTAINED BY RF BURSTS	105
6.1	Experimental Setup.....	105
6.2	Results and Discussion	106
6.3	Conclusion	110
7.	PLASMA ANTENNA EXPERIMENTS	112
7.1	Loop Antenna.....	112
7.2	Monopole Antenna.....	115
7.2.1	Measuring the Reflection Coefficient.....	115

Fluorescent Light Bulb Monopole	117
Variable Pressure Antenna	119
7.2.2 Determining Gain	125
Reference Antenna	125
Variable Pressure Plasma Antenna	128
7.2.3 Antenna Resistance and Skin Depth Analysis.....	134
7.2.4 Measuring Variable Pressure Antenna n_e	139
8. FUTURE WORK.....	144
8.1 Fundamental Experiments	144
8.2 Plasma Antenna Future Work.....	146
APPENDIX A. CONDUCTIVITY AND PERMITTIVITY IN PURE ARGON	149
APPENDIX B. ARGON IONIZATION COST VOLTAGE AND CURRENT MEASUREMENTS.....	154
REFERENCES	155
PUBLICATIONS.....	162

LIST OF TABLES

Table 2.1. Measured dissociative recombination rates and their comparison to the literature data.	42
Table 3.1. Reactions considered in this model. The reactions marked in bold font were shown to be negligible for electron recombination at the experimental conditions [66].	47
Table 6.1. The energy deposited, change in electron number density, and ionization cost for the maximum absorbed power indicated. Air plasma at 2 Torr sustained by 50 MHz, 50 μ s, RF bursts applied every 25 μ s.	108
Table 6.2. The energy deposited, change in electron number density, and ionization cost for the indicated burst duration. Air plasma at 2 Torr sustained by 50 MHz, RF bursts applied every 25 μ s for -6 dBm commanded power (25.1 W maximum absorbed).	109
Table 6.3. The energy deposited, change in electron number density, and ionization cost for the time between bursts. Air plasma at 2 Torr sustained by 50 MHz, 50 μ s RF bursts for -6 dBm commanded power (25.1 W maximum absorbed).	110
Table 7.1. The slope inferred from a linear fit of the data in figure 7.27.	142

LIST OF FIGURES

Figure 1.1. Examples of commercial fluorescent light bulbs that have been used as a dipole ((a) and (c)) and monopole (b) antenna. (a) Reprinted from [20] with the permission of AIP Publishing, (b) reproduced from [18] courtesy of The Electromagnetics Academy, and (c) reprinted from [17], © 2016 IEEE..... 20

Figure 1.2. Samples of custom antenna structures fabricated for research purposes. (a) is a plasma reflector antenna and (b) a loop antenna while (c) is a monopole antenna developed by [12]. (a) reprinted from [25], © 2016 IEEE, (b) reprinted from [26], © 2007 IEEE, and (c) reprinted from [27]..... 21

Figure 1.3. The effects of varying pressure on the plasma shape and corresponding antenna patterns: (a) $\sim 0.023\text{-}0.23$ Torr, (b) $>\sim 0.4$ Torr. All radiation patterns reprinted from [22], with the permission of AIP Publishing, while the antenna images are reprinted from [21], with the permission of AIP Publishing. 22

Figure 1.4. Example of the surfaguide plasma generation technique. 23

Figure 1.5. Plasma antenna configurations in which a single (a) and two (b) coupling sleeves are used. (a) Reprinted from [12], with the permission of AIP Publishing and (b) reprinted from [9], © 2004 IEEE..... 24

Figure 1.6. The B and E field for a TM surface wave propagating in the z -direction. $k \parallel$ is the surface wave vector parallel to the direction of propagation..... 25

Figure 1.7. Electric field profiles in and out of the plasma column. (a) © IOP Publishing. Reproduced with permission. All rights reserved. It was reprinted from [4] where (---) corresponds to $|E_z|$ and (—) corresponds to $|E_r|$. The change in dominating electric field inside and outside the glass is apparent. (b) © IOP Publishing. Reproduced with permission. All rights reserved. The figure was reprinted from [36], where A corresponds to $|E_z|$ and B to $|E_r|$. This shows the rapid drop in $|E_r|$ away from the dielectric interface in the plasma column..... 26

Figure 1.8. Limits of ω/ω_p in different conditions at which surface waves cease to propagate as a function of the wavenumber, β . Here, a is the radius of the dielectric tube and β_o the free space wavenumber. The overshoot may sometimes occur due to radial inhomogeneity of n_e [4]. This figure was reprinted from [37]. © IOP Publishing. Reproduced with permission. All rights reserved. 27

Figure 1.9. Example of a nanosecond pulse train. V_p , PRF, and P_w values indicated are particular to our FID pulsers. 29

Figure 1.10. A representation of a quasi-steady electron number density possible at high enough PRF. Decay between pulses is such that n_e is always within the same order of magnitude. 30

Figure 1.11. Chopped RF plasma antenna scheme. 31

Figure 2.1. The complete experimental setup. The numbered components are as follows: 1) FID HV nanosecond pulser; 2) LeCroy 8254M oscilloscope; 3) Back current shunt; 4) Positive

electrode; 5) Electrode connected to the shield; 6) Mass flow controller; 7) Gas supply; 8) 10 Torr Baratron; 9) Throttle valve; 10) Rotary vane pump; 11) Microwave interferometry system..... 33

Figure 2.2. A comparison of the measured voltage and current profiles using various probing techniques. 34

Figure 2.3. The microwave interferometry system used to measure n_e . The numbered components are as follows: 1) 14.525 GHz fixed oscillator; 2) 4x frequency multiplier/amplifier; 3) Isolator; 4) Directional coupler; 5) Variable attenuator; 6) Variable phase shifter; 7) Transmitting antenna; 8) Plano-convex Teflon lens; 9) Pyrex cylinder; 10) Measured plasma; 11) 2 cm aperture; 12) Receiving antenna; 13) I-Q mixer; 14) Oscilloscope. The lines represent the WR15 waveguides used to connect the components. 36

Figure 2.4. IQ plane showing how I and Q signals taken with plasma and without it, along with the center DC offset, are related to one another and can be used to determine the phase shift induced by the presence of a plasma. 38

Figure 2.5. Raw BCS data indicating pulse reflections in the system. 39

Figure 2.6. Voltage and current profiles of the first plasma pulse..... 39

Figure 2.7. Electron number density vs time in (a) argon and (b) nitrogen plasma at different PRF for $p=3$ Torr, $\dot{m}=1.45$ g/min..... 40

Figure 2.8. Inverse electron number density as a function of time in (a) argon and (b) nitrogen plasma at different PRF for $p=3$ Torr, $\dot{m} =1.45$ g/min..... 41

Figure 3.1. Effect of Ar electronic excitation on the relaxation rate of electron temperature. 58

Figure 3.2. Rate constant of electron-argon momentum transfer collisions. 59

Figure 3.3. Computed electron temperature decay with differing concentrations of H₂O..... 60

Figure 3.4. Comparison of kinetic model to the experimental data taken at 3 Torr, $\dot{m}=1.45$ g/min without considering H₂O impurities. 61

Figure 3.5. Comparison of kinetic model with the experimental argon data taken at 3 Torr, $\dot{m}=1.45$ g/min at 0.0415% H₂O..... 63

Figure 3.6. Modeled electron and ion densities for argon/water mixture at 3 Torr, $\dot{m}=1.45$ g/min with 0.0415% H₂O..... 63

Figure 3.7. Frequency of electron losses at 3 Torr, $\dot{m}=1.45$ g/min with 0.0415% H₂O. Initial losses are due to ambipolar diffusion for the first ~ 4 μ s and subsequently due to dissociative recombination (DR) with H₃O⁺. Losses due to attachment (v_{a,H_2O}) are insignificant..... 64

Figure 3.8. Comparison of kinetic model with experimental data taken at 3 Torr, 0.024% H₂O, $\dot{m}=2.90$ g/min..... 65

Figure 3.9. Comparison of kinetic model with experimental data taken at 5 Torr. 65

Figure 4.1. Conductivity for RF=30 MHz, 100 MHz, and 300 MHz in the afterglow of argon plasma. The experimentally measured n_e and corresponding modeled T_e correspond to plasma at 3 Torr argon with 450 ppm of H₂O..... 69

Figure 4.2. Permittivity for RF=30 MHz, 100 MHz, and 300 MHz in the afterglow of argon plasma. The experimentally measured n_e and corresponding modeled T_e correspond to plasma at 3 Torr argon with 450 ppm of H_2O	71
Figure 5.1. (a) Example of a high voltage, nanosecond pulse train applied at high PRF and (b) an illustration of the quasi-steady electron number density that it can sustain. n_e decay between the pulses is relatively small, less than by an order of magnitude.....	74
Figure 5.2. Theoretical cost of ionization, in eV per newly produced electron, for both argon and air as a function of applied E/N. The dashed line indicates each gas's Stoletov's point and corresponding cost.	74
Figure 5.3. The experimental setup is in 3a while the voltage and current schematic is shown in 3b. The numbered components are as follows: (1) FID HV nanosecond pulser; (2) LeCroy 8254 M and 735 ZI oscilloscopes; (3) back current shunt; (4) resistive divider HV probe; (5) Bergoz FCT; (6) positive electrode; (7) electrode connected to shield; (8) mass flow controller; (9) 10 Torr Baratron; (10) rotary vane pump; (11) gas supply; (12) dosing valve; (13) RGA system; (14) microwave interferometry system.....	77
Figure 5.4. Energy and direction of pulse propagation.....	78
Figure 5.5. Raw BCS signal profile. Each peak labeled with IN refers to the incident pulse onto the discharge and with B refers to the reflected pulse from the discharge.	79
Figure 5.6. Cumulative energy extracted by the BCS technique.	79
Figure 5.7. (a) The specific species detected by the RGA at pressures of 2, 3, 5, and 10 Torr. (b) the percent composition of the most dominant gases found during experiments in argon at the pressure tested.....	82
Figure 5.8. BCS measurement of pulse traveling to and from the plasma for a commanded voltage of 2.5 kV. The profiles have been normalized by the peak measured voltage. (a) Argon, 0.1 kHz, pressure varied (b) Argon, 10 Torr, <i>PRF</i> varied.....	83
Figure 5.9. Pulse voltage profiles applied to the plasma, reconstructed from the BCS measurements of figure 8. The profiles have been normalized by the commanded voltage of 2.5 kV. (a) Argon, 0.1 kHz, pressure varied (b) Argon, 10 Torr, <i>PRF</i> varied.....	84
Figure 5.10. BCS Reconstructed applied voltage and current profiles for indicated commanded voltage pulsed at a repetition frequency of 0.1 kHz onto air plasma at the indicated pressures. .	87
Figure 5.11. BCS reconstructed applied voltage and current profiles of the (a) 1 st and (b) 2 nd pulse for a commanded voltage of 3 kV at a repetition frequency of 0.1 kHz onto air plasma at the indicated pressures.	88
Figure 5.12. Energy deposited by the first and second pulse into air plasma at pressures of 2, 3, 5 and 10 Torr and repetition frequencies of 0.1, 3, 10, and 20 kHz. Data could only be acquired at 2 Torr at <i>PRF</i> =0.1 kHz without a corona forming.....	91
Figure 5.13. Energy deposited by the first and second pulse into argon plasma at pressures of 2, 3, 5 and 10 Torr and repetition frequencies of 0.1, 3, 10, and 20 kHz. Data could only be acquired	

at 2 Torr at PRF=0.1 kHz without a corona forming. Data was not collected at 3 Torr in figure 5.13d for the same reason. 92

Figure 5.14. Total energy deposited onto argon and air plasma at the indicated conditions. Data could only be acquired at 2 Torr at PRF=0.1 kHz without a corona forming. Data was not collected at 3 Torr in figure 5.14d for the same reason..... 93

Figure 5.15. Measured change in electron density by each applied pulse at indicated repetition frequencies and pressures in air plasma..... 94

Figure 5.16. Measured change in electron density by each applied pulse at indicated repetition frequencies and pressures in argon plasma. 95

Figure 5.17. Total electron number density produced by each pulse at indicated pressures and repetition frequencies for argon and air plasmas. 96

Figure 5.18. Effect of varying pulse repetition frequency at constant pressure in air and argon plasma on electron number density..... 97

Figure 5.19. Cost of ionization for the first and second applied pulse in argon plasma. The dashed line is the cost associated with Stoletov’s point..... 98

Figure 5.20. Reproduction of figure 5.19 with total cost of ionization included to compare to the 1st and 2nd pulse. The dashed line is the cost associated with Stoletov’s point. Error bars have been removed for clarity..... 99

Figure 5.21. Cost of electron ionization for the first and second applied pulse in air plasma. The dashed line is the cost associated with Stoletov’s point. 100

Figure 5.22. Reproduction of figure 5.21 with total cost of ionization included to compare to the 1st and 2nd pulse. The dashed line is the cost associated with Stoletov’s point. Error bars have been removed for clarity..... 101

Figure 5.23. Total cost of ionization in air and argon plasma. The top axis shows the V_{peak} corresponding to the V_{peak}/P on the bottom axis. 103

Figure 6.1. (a) Experimental setup (copy of figure 5.3a) and (b) directional coupler used to determine the electron number density and power deposited onto plasma driven by both continuous and pulsed RF waves. 106

Figure 6.2. Power absorbed and n_e in 2 Torr air plasma sustained by 50 MHz, RF bursts applied every 25 μ s for 50 μ s..... 108

Figure 6.3. Power absorbed and n_e in 2 Torr air plasma sustained by 50 MHz RF bursts applied every 25 μ s for 10, 30, and 50 μ s. Commanded power was -6 dBm. 109

Figure 6.4. Power absorbed and n_e in 2 Torr air plasma sustained by 50 MHz RF bursts applied for 50 μ s every 25, 50, and 75 μ s. Commanded power was -6 dBm. 110

Figure 7.1. The loop plasma antenna designed to operate at 1.25 GHz showing successful ignition of the plasma using a nanosecond pulser. 112

Figure 7.2. n_e as a function of applied PRF. The voltage was fixed at 5 kV with 10 ns pulse width, and an FID pulser was used. 113

Figure 7.3. n_e as a function of the measured voltage at the electrodes. A single 100 ns pulse was applied at various voltages from the Eagle Harbor pulser. 113

Figure 7.4. (a) coupler mounted to the plasma antenna and (b) the internal structure of the coupler. 114

Figure 7.5. Circuitry used to apply the power to the plasma antenna, measure the reflection coefficient, measure the power received by the plasma antenna, and measure the power deposited into the plasma. The blue arrow indicates the path of the excitation signal and the red arrow the path of the antenna signal. 116

Figure 7.6. Experimental schematic for measuring the S_{11} of the plasma antenna. (1) RF signal generator: excitation frequency (f_{ex}) source; (2) RF power amplifier; (3) directional coupler; (4) dual directional coupler; (5) oscilloscope; (6) attenuator; (7) high-pass filter; (8) VNA; (9) plasma antenna 117

Figure 7.7. (a) Fluorescent light bulb repurposed as plasma antenna used for initial monopole tests and (b) the coupling scheme used to both generate the plasma and make measurements..... 118

Figure 7.8. S_{11} measurements for indicated deposited power at excitation frequency of 120 MHz. 119

Figure 7.9. The actual variable pressure system used for experiments. (a) shows the system in its entirety during hallway testing with the plasma present while (b) shows a partially ignited plasma column..... 120

Figure 7.10. Schematic of the variable pressure plasma antenna system. System dimensions are shown in (a) and relevant components in (b). In (b): (1) Pyrex glass tube; (2) SMA connector; (3) copper coupling sleeve; (4) aluminum shield box; (5) ground plane; (6) CF 2.75 glass-to-metal sealed flange; (7) threaded rod; (8) CF 2.75 to KF-40 adapter; (9) argon gas supply; (10) mass flow controller; (11) KF-40 to KF-16 4-way cross reducer; (12) pressure gauge; (13) modified open-close valve; (14) vacuum pump 121

Figure 7.11. Copper coupler soldered to SMA cable and connected to a SMA bulkhead. 122

Figure 7.12. Alternative coupler tested. 123

Figure 7.13. Results from Aluminum foil wrapped Pyrex tube to validate S_{11} measurement setup. 123

Figure 7.14. S_{11} response measured for excitation frequencies of (a) 98 MHz and (b) 154.5 MHz at the indicated deposited powers into an argon plasma at 0.3 Torr. The sudden peaks at 309 and 463 MHz in (b) correspond to the 2nd and 3rd harmonics of the excitation frequency leaking into the measurement system. 124

Figure 7.15. Configuration used to determine the gain of the reference antenna. (1) RF signal generator: excitation frequency (f_{ex}) source; (2) RF power amplifier; (3) directional coupler; (4) dual directional coupler; (5) oscilloscope; (6) attenuator; (7) high-pass filter; (8) RF signal generator: frequency sweep (f_{Tx}) source; (10) reference antenna; (11) spectrum analyzer 127

Figure 7.16. (a) Measured gain of the reference antenna for varying transmitted powers, and (b) a comparison of the reference antenna’s measured gain to its gain profile in the antenna datasheet.	128
Figure 7.17. Experimental schematic for measuring the (a) transmitted (P_{Tx}) and (b) received power (P_{Rx}) by the plasma and reference antennas to determine antenna gain. (1) RF signal generator: excitation frequency (f_{ex}) source; (2) RF power amplifier; (3) directional coupler; (4) dual directional coupler; (5) oscilloscope; (6) attenuator; (7) high-pass filter; (8) RF signal generator: frequency sweep (f_{Tx}) source; (9) plasma antenna; (10) reference antenna; (11) spectrum analyzer	130
Figure 7.18. The measured (a) transmitting and (b) receiving gain profile for the plasma antenna. An argon plasma at 0.3 Torr was sustained by the indicated deposited power at $f_{ex}=98$ MHz. .	132
Figure 7.19. The measured transmitting and receiving gain as a function of applied power at a few different signal frequencies. An argon plasma with gas pressure of 0.3 Torr was sustained at $f_{ex}=98$ MHz in each case.	133
Figure 7.20. Gain profile of a plasma antenna as a receiver for varying transmission output powers. An argon plasma with gas pressure of 0.3 Torr was sustained by 64.5 W at $f_{ex}=98$ MHz in each case.....	133
Figure 7.21. Real and imaginary parts of the plasma permittivity for an argon plasma at 0.3 Torr with $n_e \approx 3 \times 10^{11}$ cm ⁻³	135
Figure 7.22. Calculated skin depths for the reference and plasma antenna.	135
Figure 7.23. (a) The plasma antenna conductivity as a function of frequency and (b) the ratio of the reference antenna to the plasma antenna conductivity. The reference antenna conductivity is invariant with frequency.	136
Figure 7.24. The calculated resistance for the reference and plasma antenna.	137
Figure 7.25. The estimated relative gain between the plasma and reference antenna.	138
Figure 7.26. Microwave interferometer used to measure electron number density at $z=3.6$ cm above the shielding box. The red arrow shows the direction of the microwave beam.	139
Figure 7.27. Measured electron number density of an argon plasma at the indicated pressure and excitation frequency as function of power. All data was taken with the Aethercomm amplifier, unless marked with AR which indicates the AR amplifier was used.	142
Figure 7.28. Comparison of the measured n_e in argon plasma between $f_{ex}=90$ MHz and $f_{ex}=500$ MHz at 0.3 Torr and 0.5 Torr.	143
Figure 8.1. (a) Assembled stainless steel vacuum chamber system configured for microwave interferometry, voltage, and current measurements and (b) the teflon insulated electrode structure with embedded aluminum electrodes.....	145
Figure 8.2. (a) Top and (b) front view of microwave interferometry system with 6 in. long foam absorbers inside of the PVC pipe.....	145

Figure 8.3. Preliminary tests with a nanosecond pulsed, direct electrode excitation. (a) antenna consists of an SMA connector soldered to the electrodes of a light bulb, (b) successful ignition with nanosecond pulses of this antenna, (c) setup with ground plane that will allow the light bulb to serve as a plasma antenna. A technique to make S_{11} measurements still needs to be developed.
..... 148

ABSTRACT

In the past two decades, great interest in weakly ionized plasmas sustained by high voltage nanosecond pulsed plasmas at high repetition rates has emerged. For such plasmas, the electron number density does not significantly decay between pulses, unlike the electron temperature. Such conditions are favorable to reconfigurable plasma antennas where the low electron temperature may enable the reduction of the Johnson–Nyquist thermal noise if an antenna is operated in the plasma afterglow. Moreover, it may be possible to sustain such conditions with RF pulses. Doing so could enable a plasma antenna that transmits the driving frequency when the pulse is applied and receives other frequencies with low thermal noise between pulses.

To study nanosecond pulsed plasmas, experiments were performed in a parallel-plate electrode configuration in argon and nitrogen gas at a pressure of several Torr and repetition frequencies of 30-75 kHz. To measure the time-resolved electron number density in the afterglow of each pulse, a custom 58.1 GHz homodyne microwave interferometer was constructed. The voltage and current measurements were made using a back current shunt (BCS). Initial analysis of the measured electron density in both plasmas indicated that the electron thermalization was much faster than the electron decay. In the nitrogen plasma, dissociative recombination with cluster ions was the dominant electron loss mechanism. However, the dissociative recombination rates of the electrons in the argon plasma suggested the presence of molecular impurities, such as water vapor. Therefore, to better understand the recombination mechanisms in argon plasma with trace amounts (0.1% or less by volume) of water vapor under the experimental conditions, a 0-D kinetic model was developed and fit to the experimental data. The influence of trace amounts of water on the electron temperature and density decay was studied by solving electron energy and continuity equations. It was found that in pure argon, Ar^+ ions dominate while the electrons are very slow to

thermalize and recombine. Including trace amounts of water impurities drastically reduces the time for electrons to thermalize and increases their rate of recombination.

In addition to large quasi-steady electron number densities and low electron temperature in the plasma afterglow, plasmas sustained by nanosecond pulses use a lower power budget than those sustained by RF or DC supplies. The efficiency of the power budget can be characterized by measuring the ionization cost per electron, defined as the ratio of the energy deposited in a pulse to the total number of electrons created. This was experimentally determined in air and argon plasmas at 2-10 Torr sustained by 1-7 kV nanosecond pulses at repetition frequencies of 0.1-30 kHz. The number of electrons were determined from the measured electron density through microwave interferometry and assuming a plasma volume equivalent to the volume between electrodes. The energy deposited was calculated from voltage and current measurements using both a BCS as well as high frequency resistive voltage divider and fast current transformer (FCT). It was found that the ionization cost in all conditions was within a factor of three of Stoletov's point (the theoretical minimum ionization cost) and two orders of magnitude less than RF plasma.

Having shown that it is possible to generate high electron density, low electron temperature plasmas with nanosecond pulses, it was necessary to now create a plasma antenna prototype. Initially, commercial fluorescent light bulbs were used and ignited using surface wave excitation at various RF frequencies and powers. The S_{11} of the antenna response was measured by a VNA through a novel coupling circuit, while the deposited power was measured using a bi-directional coupler. Next, a custom plasma antenna was created in which the pressure and gas composition could be varied. In addition to the S_{11} and deposited power, the antenna gain, and the electron number density were also measured for a pure argon plasma antenna at pressures of 0.3-1 Torr. Varying the applied power shifts the antenna resonance frequency while increasing the excitation

frequency caused an increase in measured electron density for the same deposited power. Initial tests using direct electrode excitation of a twin-tube integrated compact fluorescent light bulb with nanosecond pulses have successfully been achieved. Future efforts include designing the proper circuitry to time-gate out the large pulse voltage to facilitate safe antenna measurements in the plasma afterglow.

1. INTRODUCTION

1.1 Background

It was first proposed to use plasmas as a conducting medium to replace metallic RF antennas in a patent for a plasma antenna filed by John Hettinger in 1919 [1]. From the 1960s to 1980s, research on different types of plasma antennas developed [2]–[5] with other applications of using plasmas to enhance metallic antennas also emerging [6]. In the 1990s, renewed interest in these devices developed after it was shown they have stealth applications resulting from their low radar cross section (RCS) [7].

A plasma antenna is possible only when a gas is ionized to a sufficiently high degree such that the resulting plasma conductivity, σ , would enable signals at frequencies, ω , that are below the plasma frequency, ω_p , to propagate in a fashion similar to how they would along a metal. Note that ω_p is proportional to the plasma electron number density, n_e , by

$$\omega_p = \sqrt{\frac{e^2 n_e}{\epsilon_0 m}} \quad (1.1)$$

where e is the electron charge, ϵ_0 the permittivity of free space, and m the electron mass. When the ionization source is removed, the electrons quickly recombine and the antenna is turned off. In this state, the antenna is now just a gas-filled dielectric tube, undetectable on radar, a feature impossible for their metallic counterparts to achieve. This result has spurred forth extensive experimental and theoretical investigations into plasma antennas over the last two decades.

Since the year 2000, experiments and simulations have shown that plasma antennas have the potential to operate as both receivers and transmitters over a wide frequency range, ~1 MHz -1 GHz [8]–[16]. These studies have investigated how their functionality and performance are affected by the gas type used, ionization mechanism, and dielectric tube

dimensions. Some of these studies have even shown the possibility of creating antennas using inexpensive, commercially available fluorescent lamps [10], [11], [16]–[19], examples of which are shown in figure 1.1. Others have developed their own custom configurations, as shown in figures 1.2 and 1.3 to allow for more parametric studies.

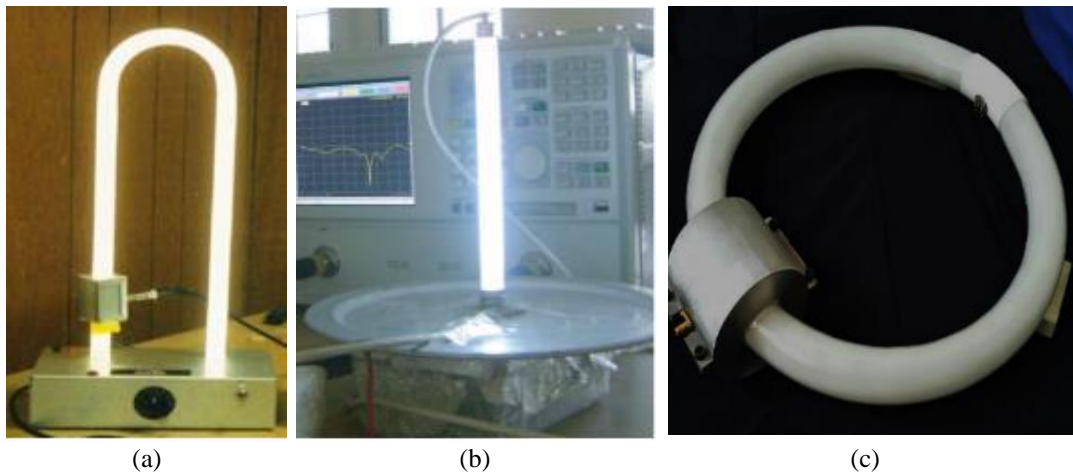


Figure 1.1. Examples of commercial fluorescent light bulbs that have been used as a dipole ((a) and (c)) and monopole (b) antenna. (a) Reprinted from [20] with the permission of AIP Publishing, (b) reproduced from [18] courtesy of The Electromagnetics Academy, and (c) reprinted from [17], © 2016 IEEE.

For a given set of parameters, one may manipulate antenna functionality by varying the plasma column length and dielectric properties by changing the gas pressure [8]–[10], [14], [21], [22], the input power [8], [9], [11], [14], [21], [23], and the excitation frequency [8], [9], [11], [24]. In such a manner, a plasma antenna can be rapidly reconfigured in shape, operating frequency, bandwidth, and directivity. Moreover, it can withstand much higher powers and have lower mutual coupling than metal antennas when used in multi-element arrays. These characteristics have been shown to exist in various custom antenna configurations such as monopole, dipole, loop, and arrayed plasma antennas.

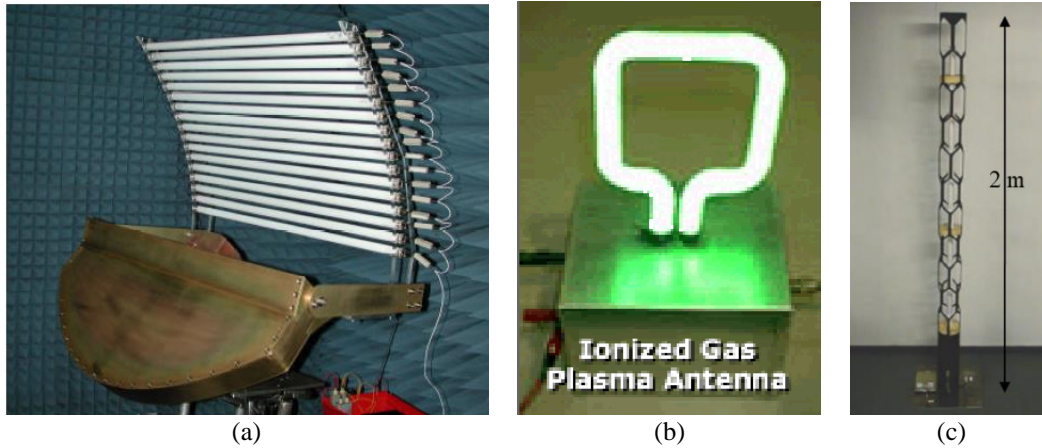


Figure 1.2. Samples of custom antenna structures fabricated for research purposes. (a) is a plasma reflector antenna and (b) a loop antenna while (c) is a monopole antenna developed by [12]. (a) reprinted from [25], © 2016 IEEE, (b) reprinted from [26], © 2007 IEEE, and (c) reprinted from [27].

As an example, consider figure 1.3 where just the effect of varying operating pressure on the plasma antenna can be observed. The authors of [21], [22] show that at pressures in the range of 0.023-0.23 Torr, the plasma is formed as a series of striations (figure 1.3a) with their size depending on the input RF power. Each one acts as an isotropic point source, collectively forming a phased array antenna. Then, as pressure is increased to above 0.4 Torr, the plasma appears uniform and the antenna radiation pattern differs from the case with striations, as seen in figure 1.3b. The radiation patterns suggest the antenna behaves more like a monopole as compared with the series of striations. Just changing the operating pressure can dramatically vary the antenna's radiation pattern and directivity.

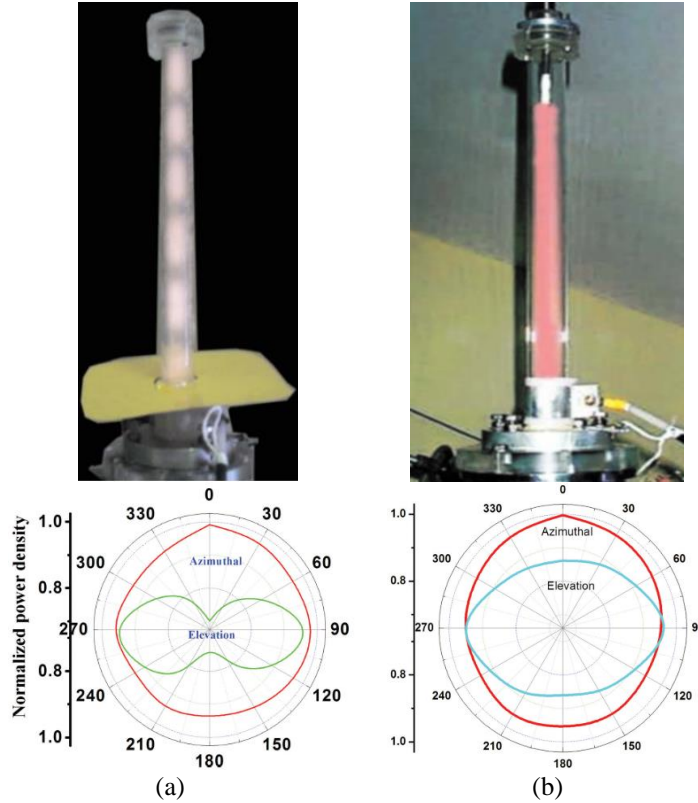


Figure 1.3. The effects of varying pressure on the plasma shape and corresponding antenna patterns: (a) ~ 0.023 - 0.23 Torr, (b) $> \sim 0.4$ Torr. All radiation patterns reprinted from [22], with the permission of AIP Publishing, while the antenna images are reprinted from [21], with the permission of AIP Publishing.

1.1.1 Plasma Antenna Sources

Plasma antennas can be sustained by DC [10], [12], [17], AC [12], [16], [18], [19], RF [8], [9], [11]–[14], [21]–[24], [28], and laser sources[29]. DC and AC power supplies directly applied to electrodes in contact with the gas are an easy means of ionization but have shown to yield noisy plasma antennas [12]. Laser sources can sustain plasmas that are more conductive but require bulkier, complex, energy intensive systems to operate. RF generators of various frequencies and powers < 100 W are also commonly used and generate more efficient plasma antennas. More rarely, surfaguides have also been used to generate plasmas[30]–[32]. These are devices in which a waveguide is used to launch a microwave into a tube inserted inside of it, thereby ionizing the

enclosed gas. RF signals can then be coupled to the plasma column serving as an antenna. An example of such a system is shown in figure 1.4.

Unlike other devices that perturb the plasma to sustain it, RF power supplies can generate a plasma directly through electrodes in contact with a gas or indirectly through a capacitively coupled sleeve surrounding the dielectric tube, as shown in figure 1.5. Coupling sleeves are preferred since the presence of electrodes and unshielded wiring adversely affect the radiation characteristics of the antenna. Moreover, by utilizing a sleeve, a single RF source can ionize the gas and transmit a signal at the same excitation frequency, in stark contrast to other excitation techniques. Of course, the technique of using two sleeves, one to sustain the plasma and another to couple the signal, is practiced as well. Plasmas generated through these capacitively coupled sleeves sustained by surface waves have been extensively researched and shown to produce radially uniform, stable plasmas [33].

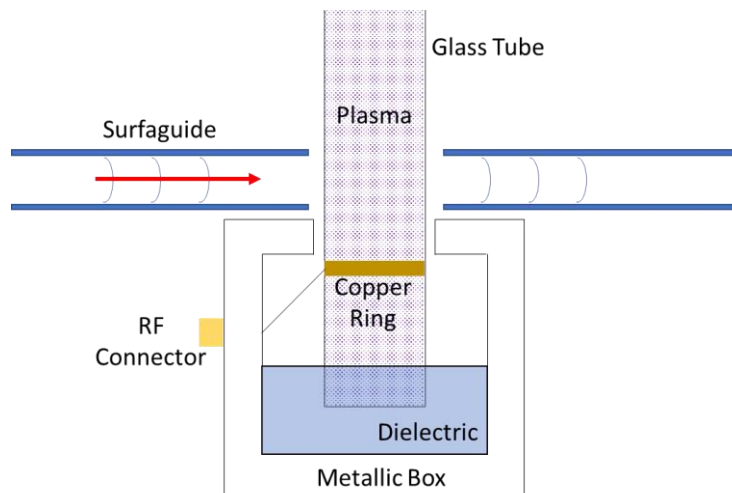


Figure 1.4. Example of the surfaguide plasma generation technique.

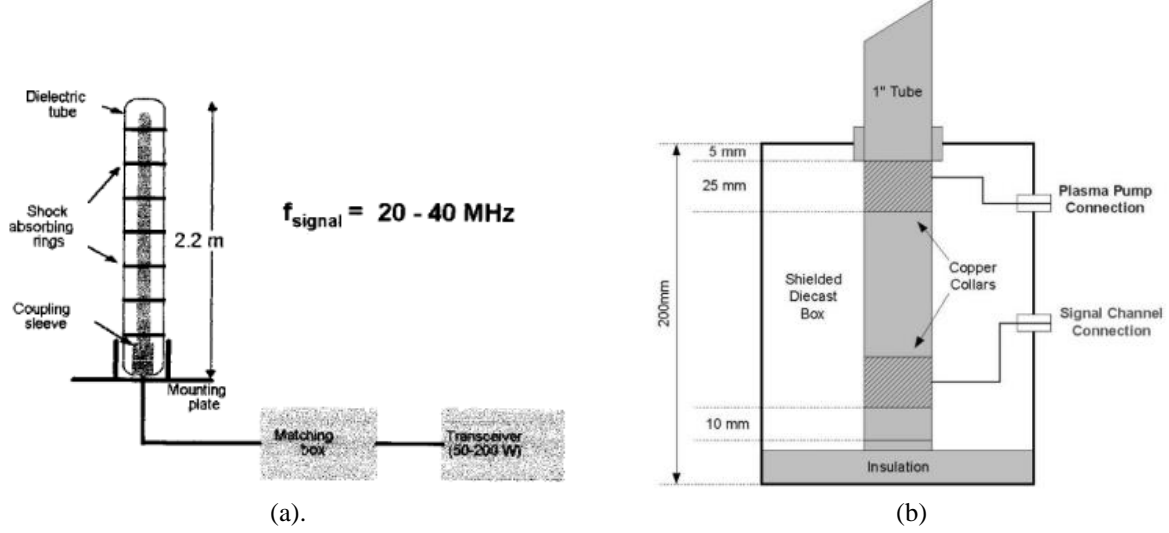


Figure 1.5. Plasma antenna configurations in which a single (a) and two (b) coupling sleeves are used. (a) Reprinted from [12], with the permission of AIP Publishing and (b) reprinted from [9], © 2004 IEEE.

1.1.2 Brief Overview of Surface Waves

Surface waves in plasma columns were first discovered by Trivelpiece and Gould in 1959 [34]. These waves have phase velocity, $V_{\phi} \leq c$, the speed of light in a vacuum, and travel along the interface between two dielectrics, each with different relative permittivity. An example of such a wave travelling along a plasma with permittivity ϵ_r and a dielectric (such as Pyrex) with permittivity ϵ_g is shown in figure 1.6. Here, ϵ_g is a fixed property while ϵ_r can vary since it depends on ω , ω_p , and ν_m by

$$\epsilon_r = 1 - \frac{\omega_p^2}{\omega^2 + \nu_m^2} \quad (1.2)$$

where ν_m is the electron-neutral collision frequency. Surface wave propagation is only possible when $\epsilon_r < 0$, $\epsilon_g > 0$ and $|\epsilon_r| > \epsilon_g$ [4], [35], [36] which is satisfied in a plasma surrounded by a dielectric if $\nu_m < \omega < \omega_p$.

If the wave is symmetric, as in a plasma bounded by a dielectric cylinder, only TM waves satisfy the appropriate boundary conditions for \vec{E} and \vec{B} field continuity, and the only non-zero

field components are E_r , E_z , B_ϕ [4], [35]. The wave field and wave vector of such a wave propagating in the z -direction are shown in figure 1.6.

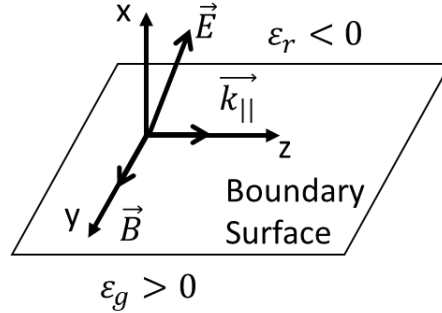


Figure 1.6. The \vec{B} and \vec{E} field for a TM surface wave propagating in the z -direction. $\vec{k}_{||}$ is the surface wave vector parallel to the direction of propagation.

These waves are evanescent, meaning the intensity of their \vec{E} and \vec{B} fields decay radially as [4]

$$E_o, B_o \propto \frac{1}{\sqrt{r}} \exp(-k_{\perp} * r) \quad (1.3)$$

where r is the transverse distance from a plasma column and k_{\perp} is the transverse wavenumber also referred to as the decay coefficient [4]

$$k_{\perp} = \left(\beta^2 - \epsilon_r \frac{\omega^2}{c^2} \right)^{1/2} \quad (1.4)$$

where β is the wavenumber of the surface wave propagating along the boundary between the two materials. In such conditions, the electric fields take the profiles presented in figure 1.7. The electric field is maximum at the dielectric interface and then decays on either side. Within the plasma column, the transverse component of the electric field, $|E_r|$, is much less than the axial component, $|E_z|$, everywhere except for near the dielectric where the two can be comparable. Outside the column, in air or vacuum, the opposite is true.

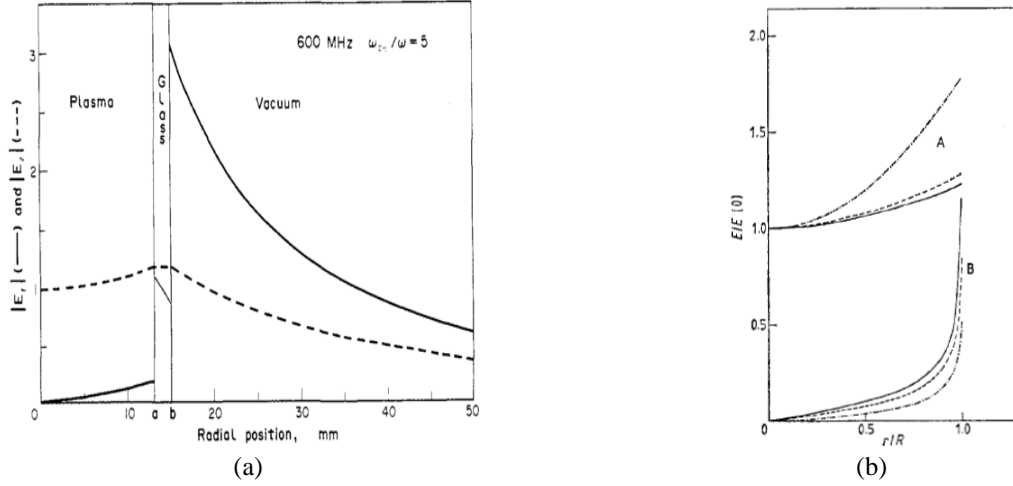


Figure 1.7. Electric field profiles in and out of the plasma column. (a) © IOP Publishing. Reproduced with permission. All rights reserved. It was reprinted from [4] where (---) corresponds to $|E_z|$ and (—) corresponds to $|E_r|$. The change in dominating electric field inside and outside the glass is apparent. (b) © IOP Publishing. Reproduced with permission. All rights reserved. The figure was reprinted from [36], where A corresponds to $|E_z|$ and B to $|E_r|$. This shows the rapid drop in $|E_r|$ away from the dielectric interface in the plasma column.

For surface waves to exist, ω and ω_p must satisfy certain limits that arise from the solution of the dispersion relations and are depicted in figure 1.8 [35], [37]. For a collisionless plasma column ($v_m^2 \ll \omega^2$) surrounded just by vacuum, $\omega/\omega_p \leq 1/\sqrt{2}$ while for a plasma column in a dielectric tube $\omega/\omega_p \leq 1/\sqrt{1 + \epsilon_g}$. As ω/ω_p approach these limits, $\beta \rightarrow \infty$ and the group velocity, V_g , approaches zero causing propagation to stop [4]. If these conditions are met, the minimum local electron density needed to facilitate surface wave propagation within a column is [33]

$$n_D = 1.2 \times 10^4 (1 + \epsilon_g) f^2 \text{ (cm}^{-3}\text{)}$$

where f is the surface wave frequency in MHz. Moreover, operation in the $m=0$ mode (azimuthally symmetric fields) requires satisfying $fR < 2$ GHz-cm where R is the radius of the dielectric tube [38].

As $\omega/\omega_p \rightarrow 0$, $\beta \rightarrow \beta_o$, the free space wavenumber. Under this limit, the plasma conducts the surface wave similar to a metal and most of the wave power flows outside of the dielectric [4]. In general, three modes can exist in a plasma antenna based on the value of this parameter: non-radiative, transitional, and linear [39]. As $\omega/\omega_p \rightarrow 1/\sqrt{2}$ or $1/\sqrt{1 + \epsilon_g}$, the antenna is in the

non-radiative mode. For $\omega/\omega_p \leq 0.1$ it is in the linear mode. In between it is in the transitional mode, where the radiation is very sensitive to wave parameters.

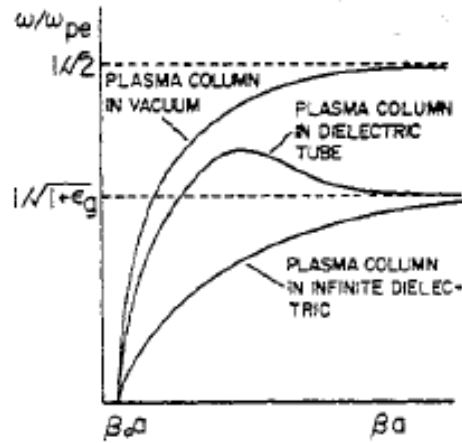


Figure 1.8. Limits of ω/ω_p in different conditions at which surface waves cease to propagate as a function of the wavenumber, β . Here, a is the radius of the dielectric tube and β_0 the free space wavenumber. The overshoot may sometimes occur due to radial inhomogeneity of n_e [4]. This figure was reprinted from [37]. © IOP Publishing. Reproduced with permission. All rights reserved.

These surface waves can operate in both a self-sustained mode, ionizing the gas as they propagate, and in a coupled mode where they propagate along an already existing plasma column. Therefore, surface wave plasmas can be driven from a single capacitive coupler with an RF source. Such an excitation technique does not require electrodes in contact with the gas, has been shown to be more efficient in producing plasma, does not produce many perturbations in the gas, and creates a more stable plasma compared to a DC column [12], [40]. When designing a surface-wave driven or capacitively coupled plasma antenna, it is important to ensure these conditions are satisfied for successful device operation.

1.2 Motivation

A couple of main hurdles have prevented the widespread adoption of plasma antennas. First, plasmas have conductivities 10^4 - 10^6 times smaller than in metals, resulting in an antenna gain that is at best 5-10 dB smaller [8], [11], [13], [14], [19], [29] and effective antenna efficiencies of 75%

at best [9], [21], [41], [42]. Second, plasma antennas have a larger Johnson-Nyquist thermal noise than their metallic counterparts because the temperatures of the charge carriers (electrons) are several eV larger than in metals. This makes them unattractive as receivers because larger thermal noise necessitates a stronger received signal for detection. These drawbacks may be mitigated by utilizing pulsed excitation techniques to sustain the plasma.

It has been claimed that a pulsed DC ionization mechanism reduced the noise of, increased the electron density in, and decreased the power consumed by a plasma antenna [13]. Furthermore, it has been shown that using pulsed RF signals, the noise of a plasma antenna receiver measured by a SINADDER was at most 4 dB higher than the typical noise power threshold of a receiver (-120 dBm) [12]. Such results are both beneficial to plasma antennas since this suggests improvement in conductivities and noise, important for reception.

The plasma conductivity, σ , is defined as [43]

$$\sigma = \epsilon_0 \nu_m \frac{\omega_p^2}{\omega^2 + \nu_m^2}. \quad (1.5)$$

Any increase in the electron density of the plasma antenna would directly increase σ because $\omega_p^2 \propto n_e$ (cf. equation (1.1)). The Johnson-Nyquist thermal noise power, P , per unit bandwidth, Δf , is given by [44]

$$\frac{P}{\Delta f} = \frac{4kT_e}{1 + \frac{\omega^2}{\nu_m^2}} \left(\frac{\text{W}}{\text{Hz}} \right) \quad (1.6)$$

where k is the Boltzmann constant and T_e is the electron temperature. In metals, $T_e = T = 300$ K (0.025 eV) and $\nu_m^2 \gg \omega^2$ while in a non-equilibrium plasma, $T_e = 1-5$ eV and ν_m depends on the gas and its pressure. As such, DC and RF plasmas inherently have a noise power that is several orders of magnitude larger than in metals. To ensure low noise in plasma antennas, it is necessary to

reduce the electron temperature and operate at a low pressure to minimize the collision frequency. However, this reduction must be traded off with the conductivity since it is also dependent on ν_m . Even if $\nu_m = \omega$, $P/\Delta f$ would still be half that of metals assuming $T_e \approx T$. By operating in a pulsed regime, large electron densities can be sustained, and, in the proper operating mode, the electron temperature can quickly approach room temperature in the plasma afterglow. Such conditions can be sustained using nanosecond pulses.

High-voltage (HV), repetitive, nanosecond pulses can efficiently create plasmas with sufficiently high electron densities while utilizing a low power budget [45]. During the short pulse, E/N , where E is the electric field and N the gas density, in such plasmas is very high (typically on the order of 1000 Td) [45], resulting in optimal conditions for ionization and generation of various excited species. Between the pulses, the plasma decays due to recombination, attachment, and diffusion; however, if the next ionizing pulse is applied before the plasma density decays by more than a factor of 2-3, a quasi-continuous plasma can be sustained [45]. Figure 1.9 shows an example of such a pulse train. The peak voltage, V_p , pulse width, P_w , and pulse repetition frequency, PRF, correspond to the maximum capabilities of our FID, FPG 10-1 MHN and FPG 1-3 MH2 pulse generators. Other pulse generators, such as the Eagle Harbor NSP with $V_p \leq 30$ kV and $P_w \leq 100$ ns are also available to use for experimentation.

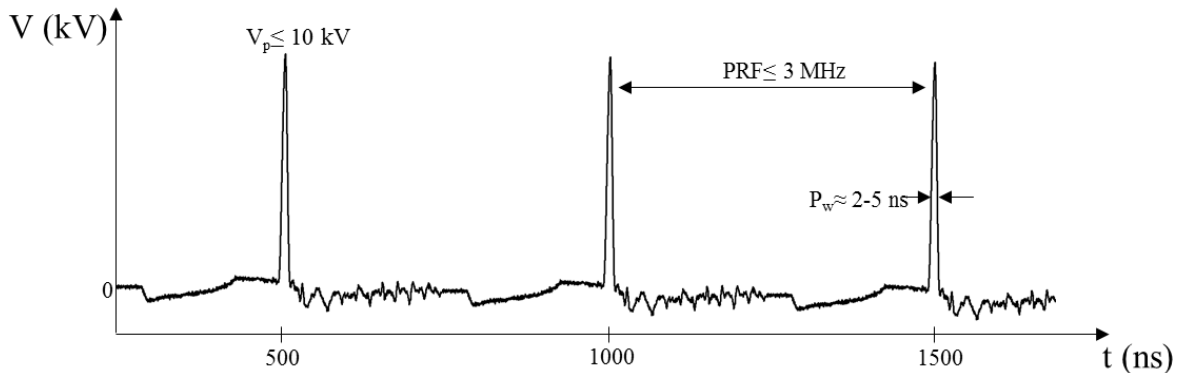


Figure 1.9. Example of a nanosecond pulse train. V_p , PRF, and P_w values indicated are particular to our FID pulsers.

The ability of nanosecond-pulsed plasmas to generate large quantities of excited species and to deliver significant amounts of energy in a short period of time has made them particularly attractive for plasma-assisted combustion and aerodynamic flow control applications [46]–[50]. However, in most cases related to those applications, the pulse repetition frequency is low enough to ensure an almost complete electron density decay between the pulses. If the PRF can be high enough to sustain quasi-continuous plasmas (cf. figure 1.10), then between pulses, the electron temperature could thermalize much faster than the electron density would decay. Thus, under appropriate operating conditions, a plasma with sufficiently high average electron number density ($\approx 10^{10}$ - 10^{13} cm⁻³) and with a low mean electron temperature can be used to create more conductive, low-noise plasma antennas.

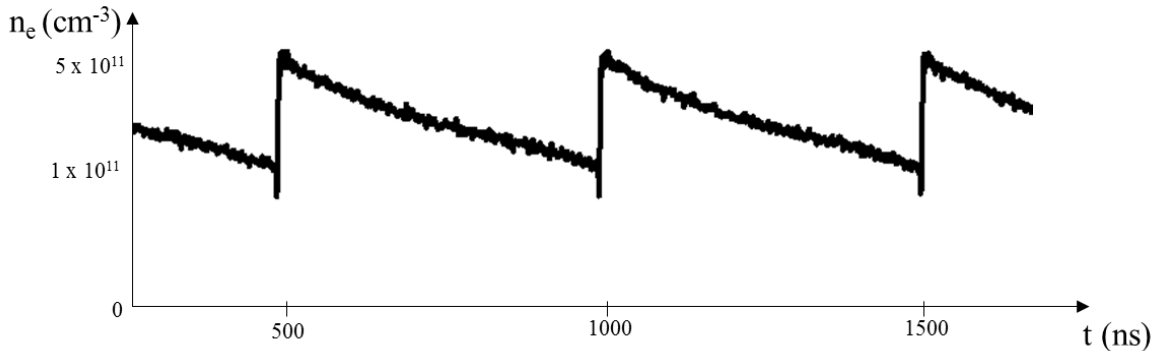


Figure 1.10. A representation of a quasi-steady electron number density possible at high enough PRF. Decay between pulses is such that n_e is always within the same order of magnitude.

Like nanosecond pulses, if an RF signal is “chopped” using an external triggering mechanism, it is believed that between pulses, the electron temperature would also decay quickly. If the quasi-steady electron number density is large enough, then such a scheme can also be used with plasma antennas. Such a technique may enable the antenna to serve as a transmitter of signals at the source excitation frequency and a receiver with low thermal noise in the afterglow, as

depicted in figure 1.11. This would be advantageous to using nanosecond pulses because a second signal generator would not be required to couple a signal to the plasma.

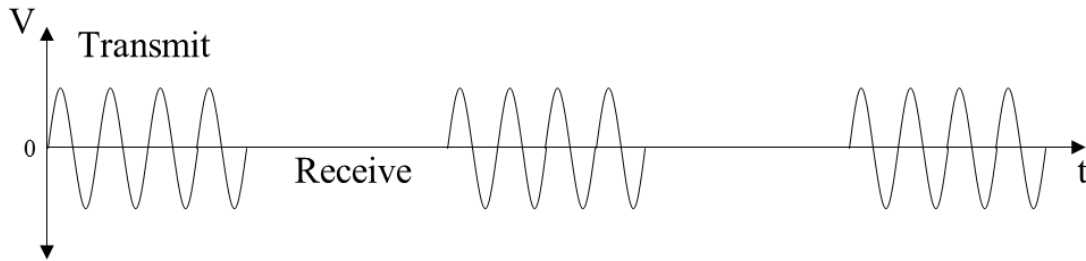


Figure 1.11. Chopped RF plasma antenna scheme.

Therefore, it is necessary to conduct experimental research to understand the levels of n_e achievable using such pulsed techniques at various gas types, pressures, and electrode spacings. It is also important to measure the electron temperature in the plasma afterglow. Kinetic modeling of the experiments performed is also necessary to understand the recombination processes. Once this is understood, these sources can be used to generate operational plasma antennas.

2. DIAGNOSTICS OF NANOSECOND PULSED PLASMA

Large portions of this chapter were reprinted from V. Podolsky, A. Khomenko, and S. Macheret, “Time-resolved measurements of electron number density in argon and nitrogen plasmas sustained by high-voltage, high repetition rate, nanosecond pulses,” *Plasma Sources Sci. Technol.*, vol. 27, no. 10, p. 10LT02, 2018. © IOP Publishing. Reproduced with permission. All rights reserved.

2.1 General Facility Development

To conduct experimental studies, the vacuum system shown in figure 2.1 was constructed. It consists of a Pyrex cylinder seated onto recessed face seals between two acrylic caps. This design was chosen to allow for visual clarity and easy, non-invasive plasma diagnostic techniques. In the chamber, two aluminum parallel-plate electrodes 10.16 cm in diameter were aligned and spaced 2 cm away from each other. The central wire of the coaxial cable was attached to the top electrode and the shield wire to the bottom. An Alcatel 2033A rotary vane vacuum pump was used to evacuate the chamber and the pressure was measured using a 10 Torr Baratron (MKS-626C). Before testing, the chamber was first evacuated to a base pressure of 10 mTorr and the desired test gas was introduced to purge the system. Afterwards, a throttle valve and a flow controller (Alicat MC-10SLPM) were used to attain the desired chamber pressure for a given mass flow rate.

To generate the plasma, the FID FPG 1-3MH2 pulser was used. It outputs a fixed 820 V, 3 ns FWHM pulse at pulse repetition frequencies (PRF) of up to 3 MHz. Tests with argon and nitrogen were performed at a pressure of 3 Torr with PRFs of 30-75 kHz. The voltage and current profiles were attained using a back current shunt (BCS) consisting of fifteen, 2.2 Ω carbon-film resistors soldered in parallel onto the shielding of a 30 m RG-217 coaxial cable. The voltage drop across the resistors was measured using a Lecroy 8254M oscilloscope. A detailed description of

the theory behind a BCS can be found in [51]. The BCS was calibrated by applying known currents and measuring the corresponding voltage drop across the shunt resistors.

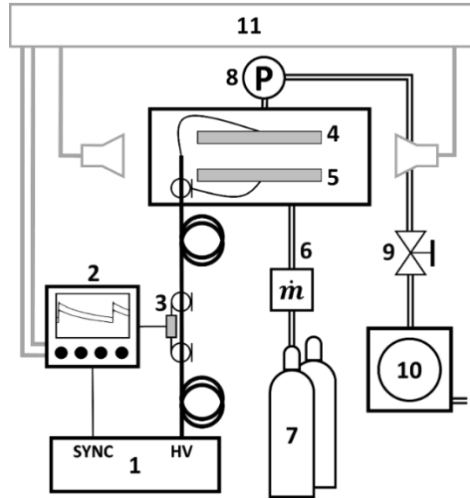


Figure 2.1. The complete experimental setup. The numbered components are as follows: 1) FID HV nanosecond pulser; 2) LeCroy 8254M oscilloscope; 3) Back current shunt; 4) Positive electrode; 5) Electrode connected to the shield; 6) Mass flow controller; 7) Gas supply; 8) 10 Torr Baratron; 9) Throttle valve; 10) Rotary vane pump; 11) Microwave interferometry system.

2.2 Voltage and Current Measurements

Other voltage and current measuring techniques were tested before the BCS was chosen. Due to the construction of the vacuum chamber used, it was impossible to test these devices on this system. Therefore, a plasma was created under the same pressure, electrode spacing, and gas type in another vacuum chamber with 5.08 cm diameter electrodes. The discrepancy in electrode diameter should have minimal, if any, effect on the overall pulse profile. On this chamber, in addition to the BCS, three different voltage probes (the Montena VDOT8G, the Lecroy PPE6KV and the HP HF 54006A 6 GHz Resistive Divider) and another current probe (Bergoz FCT-028-1.25-WB) were used to measure the pulse shape. The peaks of the profiles were aligned, and an average and standard deviation were calculated to show the discrepancy between devices, as shown in figure 2.2.

The measured voltage and current profiles each give a different measured peak amplitude and appear to indicate pulse broadening in devices other than the BCS. When the nanosecond pulse reaches the plasma, an impedance mismatch between the transmission line and load (the plasma) is present causing the pulse to be reflected. Other than the BCS, each of the probes is placed as close as possible to the electrodes to minimize the influence of the reflection, but some influence remains and appears in the form of pulse broadening. In particular, the PPE6KV has a bandwidth of only 400 MHz; it cannot capture the full correct profile shape of the 3-5 ns time scale. With the back current shunt, on the other hand, the forward and reflected pulse are separated, eliminating pulse broadening and allowing extraction of the correct magnitude of the proper transmitted pulse. These observations are supported by the matching of the voltage and current profiles of the high frequency devices when measured on the same matched load.

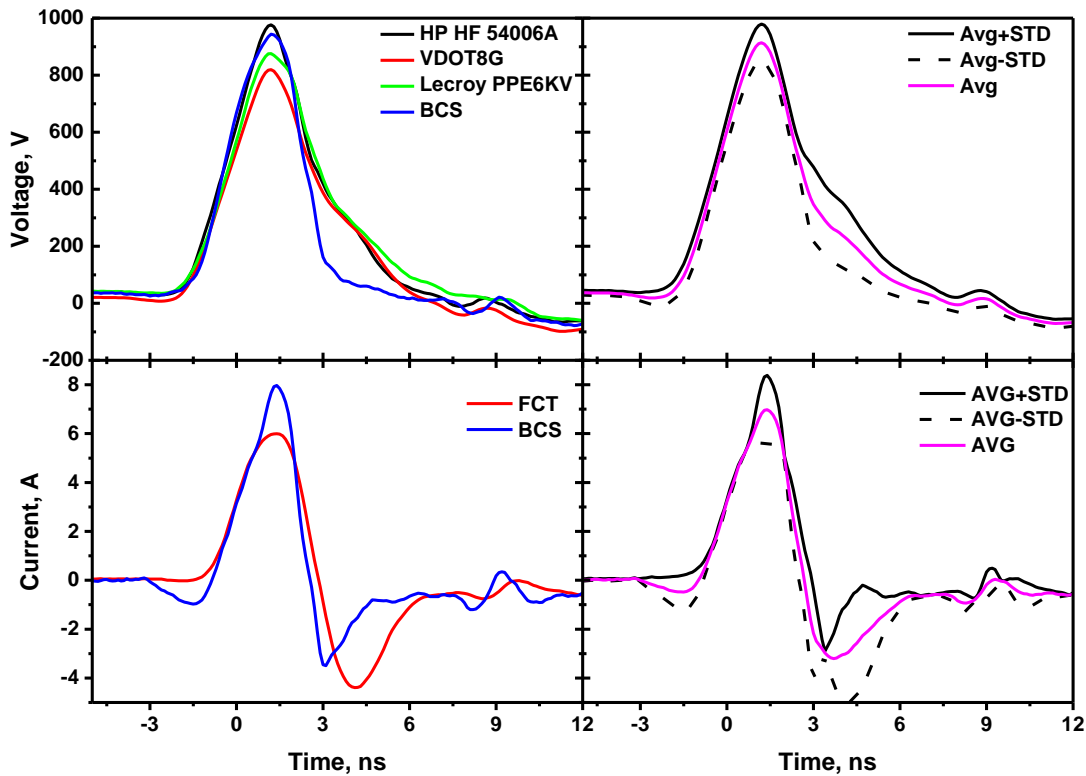


Figure 2.2. A comparison of the measured voltage and current profiles using various probing techniques.

2.3 Microwave Interferometry System

To characterize the electron number density in the afterglow of such a plasma, a microwave interferometry system was constructed to perform time-resolved measurements. Microwave interferometry is an attractive method to measure electron number density that can be performed in a wide range of experimental configurations and on various types of plasmas [52]. It has been utilized to make time-resolved measurements of Hall thruster plasma plumes [53], RF plasmas [54]–[56], laser induced plasmas [57], and pulsed plasmas [58]–[60]. It is nonintrusive, operable over a wide pressure range, and requires minimal assumptions to be made about the plasma [55]–[57], [61]. Other techniques, including Stark broadening and Thompson scattering, are only effective at very high electron number densities and require a much more complex experimental setup.

Measuring the phase shift of a microwave with angular frequency ω transmitted across a uniform plasma of known length, L , permits the determination of the line-of-sight average electron number density, n_e , along the probing path can be determined [52]. Under the conditions of this experiment, the high frequency limit of $\omega \gg \omega_p \gg \nu_m$ is valid, where ω_p is the plasma frequency and ν_m is the electron-molecule momentum transfer collision frequency. In this regime, the real part of the wavenumber, k , is $\frac{\omega}{c} \left(1 - \frac{\omega_p^2}{\omega^2}\right)^{\frac{1}{2}}$ where c is the speed of light.

By comparing the absolute change in k of a microwave traversing air to that across a plasma, the phase difference, $\Delta\Phi$, due to the presence of the plasma is given by [52]

$$\Delta\Phi = \frac{\omega}{c} \int \left[1 - \left(1 - \frac{\omega_p^2(x)}{\omega^2} \right)^{\frac{1}{2}} \right] dx. \quad (2.1)$$

Since ω_p is related to n_e , a Taylor series expansion of the expression for $\Delta\Phi$ in the high frequency gives an explicit relation for n_e [52] of

$$n_e = \frac{2\epsilon_0 mc \omega \Delta\Phi}{e^2 L} \quad (2.2)$$

where m is the electron mass, e is the electron charge, and ϵ_0 is the permittivity of free space.

To utilize this theory and determine the n_e of the bulk plasma, a homodyne microwave interferometry system (MIS) operating at a frequency of 58.1 GHz was constructed; at this frequency, the critical electron number density, n_c , is $4.17 \times 10^{13} \text{ cm}^{-3}$. Figure 2.3 shows a block diagram of this system. A local phase-locked oscillator (Herley PDRO-14744) produces a sinusoidal signal of 14.525 GHz that is quadrupled and amplified through an active multiplier (Millitech AMC-15-RFHB0). The resultant signal of 58.1 GHz with a power of up to 25 dBm is transmitted through an isolator before being divided through a directional coupler into the reference and plasma branches. The signal has a power of 5 dBm in the reference branch and 25 dBm in the plasma branch. As the signal propagates through the plasma branch, it is transmitted from a pyramidal horn antenna (Flann 25240-20) through the plasma via a beam focusing system before being received by another antenna and sent to the RF port of an I-Q mixer (Millitech MIQ-15-01900).

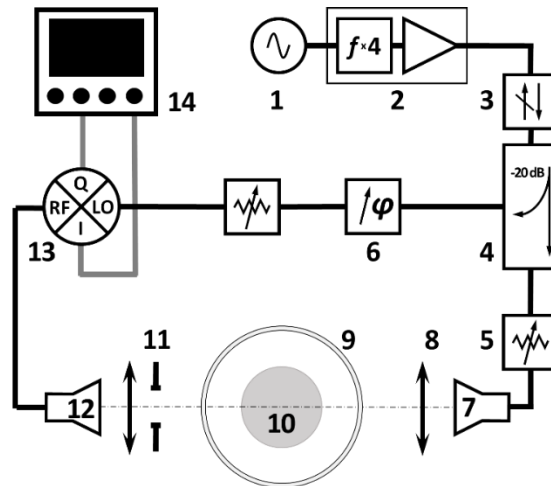


Figure 2.3. The microwave interferometry system used to measure n_e . The numbered components are as follows: 1) 14.525 GHz fixed oscillator; 2) 4x frequency multiplier/amplifier; 3) Isolator; 4) Directional coupler; 5) Variable attenuator; 6) Variable phase shifter; 7) Transmitting antenna; 8) Plano-convex Teflon lens; 9) Pyrex cylinder; 10) Measured plasma; 11) 2 cm aperture; 12) Receiving antenna; 13) I-Q mixer; 14) Oscilloscope. The lines represent the WR15 waveguides used to connect the components.

Meanwhile, the reference signal is transmitted to the LO port of the mixer. Because the frequencies entering the RF and LO part of the mixer are equal, the output signals from the I and Q ports are DC and proportional to the probing wave's phase shift. Consequently, $\Delta\Phi$ can be determined by comparing the measured I and Q signals with plasma to those without it. The attenuator (Millitech 45734H-1200) upstream of the LO port is used to ensure that the mixer does not saturate while the phase shifter (Hitachi M4610), as well as the other attenuator (Flann 25020), are used in calibrating the MIS.

The purpose of the focusing system is to improve the signal-to-noise ratio of the RF signal received by the I-Q mixer. A plano-convex Teflon lens (ThorLabs LAT075) on the transmitting side of the system focuses the signal before it is beamed into the plasma and then through a 2 cm aperture (ThorLabs ID36) downstream of the chamber. An aperture is used to ensure that only the portion of the probing beam traveling through the desired portion of the electrode gap is detected, minimizing the influence of any reflected or scattered signals. Finally, the probing beam is focused onto the receiving antenna horn by the second lens.

To account for measurement deviations arising from the losses inherent to the microwave system, an intrinsic DC offset of the system, and offsets created by the probing signal propagating through a Pyrex cylinder of a certain gas and pressure, the following calibration process was developed. It was inspired by a similar technique developed in [53]. Phase shifts induced by the Pyrex and the vacuum chamber environment were determined by transmitting the interferometer signal through the electrodes with no plasma present. The resulting I and Q signals were recorded and are indicated by I_{NP} and Q_{NP} in figure 2.4. The DC offset was accounted for by completely attenuating the signal emitted in the plasma branch (block 5 in figure 2.3) and measuring the resulting I and Q signals, I_C and Q_C .

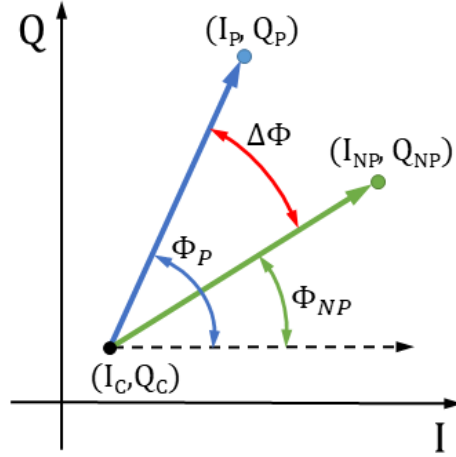


Figure 2.4. IQ plane showing how I and Q signals taken with plasma and without it, along with the center DC offset, are related to one another and can be used to determine the phase shift induced by the presence of a plasma.

As shown in figure 2.4, once a measurement through the plasma is acquired (I_P, Q_P) , it can be used with (I_{NP}, Q_{NP}) and (I_C, Q_C) to give a trigonometric relation for $\Delta\Phi$

$$\Delta\Phi = \tan^{-1}\left(\frac{Q_P - Q_C}{I_P - I_C}\right) - \tan^{-1}\left(\frac{Q_{NP} - Q_C}{I_{NP} - I_C}\right) \quad (2.3)$$

This $\Delta\Phi$ is then used in equation (2.2) to determine n_e . It should be noted that in these experiments, because the beam was aligned to propagate through the central region of the plasma, L was assumed to be equal to the diameter of the electrodes. Using this calibration technique yielded a resolution in the n_e measurements of 10^8 cm^{-3} and the overall uncertainty of around 25%. The uncertainty was estimated by comparing multiple measurements acquired under similar conditions.

2.4 Experiment Results and Discussion

Consider the voltage and current at the plasma electrodes during each pulse emitted from the high voltage pulser. In the raw BCS data presented in figure 2.5, it is clearly seen that the initial HV pulse occurs at 0 ns and the first reflection from the plasma electrode system occurs at about 300 ns. The reflection occurs because the impedance of the plasma electrode system is not equal to the 50Ω impedance of the cable. Also, the signal attenuates as it travels down the cable.

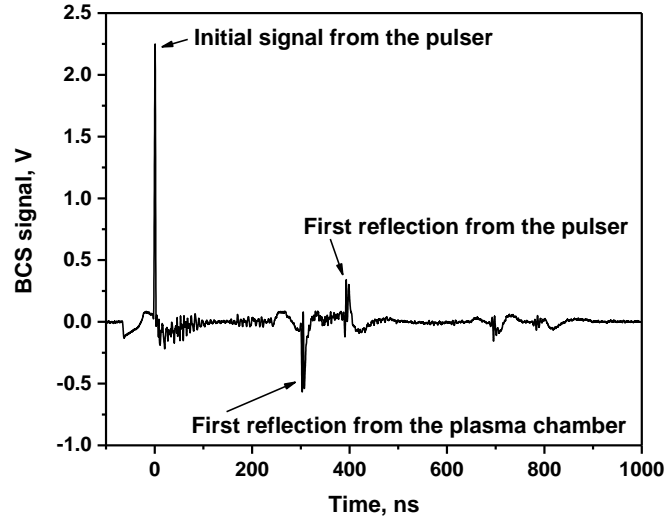


Figure 2.5. Raw BCS data indicating pulse reflections in the system.

By the procedure described in [51], the actual voltage and current at the plasma electrodes was reconstructed from the BCS data. More attention was paid to the first plasma pulse profile, as it contains more than 90% of the energy delivered to the plasma. The pulse's measured voltage and current profiles are shown in figure 2.6 from which it is evident that the applied peak voltage was 790 V and the peak current was 9.8 A.

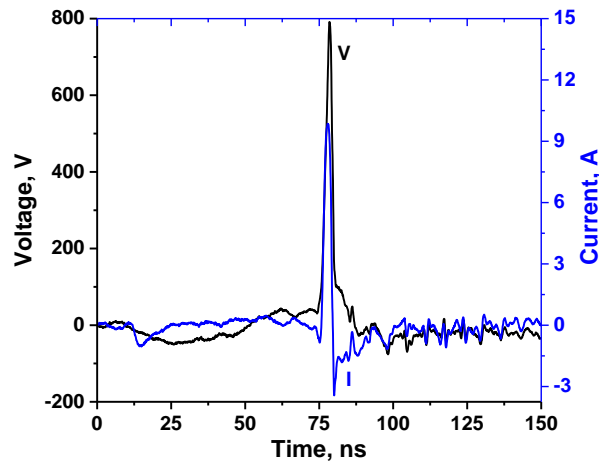


Figure 2.6. Voltage and current profiles of the first plasma pulse.

The measured time-resolved electron density in argon and nitrogen plasmas at various pulse repetition rates are shown in figures 2.7a and 2.7b, respectively. It is clear that n_e increases

with PRF for both gases. For argon, the quasi-steady average of the measured n_e changes from $1.8 \times 10^{10} \text{ cm}^{-3}$ at a PRF of 30 kHz to $2.0 \times 10^{10} \text{ cm}^{-3}$ at a PRF of 75 kHz, and for nitrogen, the quasi-steady average of the measured n_e changes from $6.7 \times 10^9 \text{ cm}^{-3}$ at a PRF of 30 kHz to $1.4 \times 10^{10} \text{ cm}^{-3}$ at a PRF of 75 kHz. The reason for this is simple: the total amount of power applied to the plasma increases with PRF which results in a larger ionization fraction and therefore a higher n_e for a given pressure.

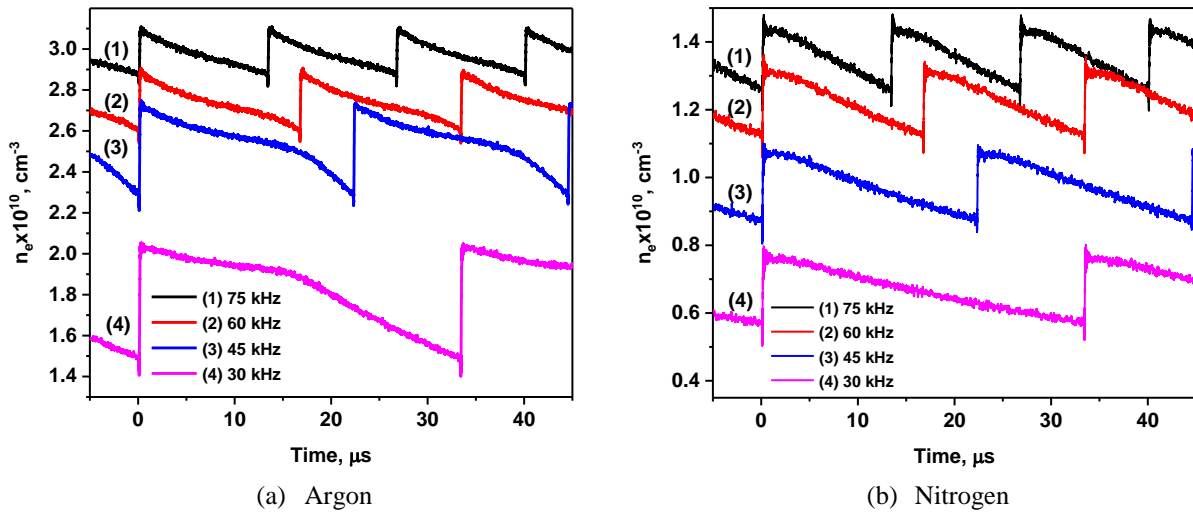


Figure 2.7. Electron number density vs time in (a) argon and (b) nitrogen plasma at different PRF for $p=3$ Torr, $m=1.45$ g/min.

Another way of looking into this is to note that operating at high PRF reduces the time for recombination processes to proceed between the pulses. Therefore, the relative change in n_e between consecutive pulses decreases when operating in the quasi-steady regime, (i.e. when the average n_e remains constant as pulses are applied). This phenomenon is more clearly observed by examining the measured inverse electron number densities for both plasmas presented in figure 2.8a and 2.8b.

Analysis of these measured profiles can provide insight into the dominant recombination mechanisms. Estimates show that in the conditions of the experiments the ambipolar diffusion is too slow to account for the observed decay of electron density. Then, for a quasi-neutral plasma,

the number density of ions, n_i , is approximately equal to that of the electrons, and in the absence of ionization between the pulses, the continuity equation considering only two-body recombination can be written as

$$\frac{dn_e}{dt} = -\beta n_e n_i = -\beta n_e^2 \quad (2.4)$$

where β is the two-body dissociative recombination rate coefficient. If $\beta = \text{const}$, then the solution shows a linear relation between the change in $1/n_e$ and t

$$\frac{1}{n_e(t)} = \frac{1}{n_{e,0}} + \beta t \quad (2.5)$$

where $n_{e,0}$ is the initial electron density at $t=0$, corresponding to the moment immediately after the pulse. Therefore, it is useful to analyze the reciprocal of electron number density.

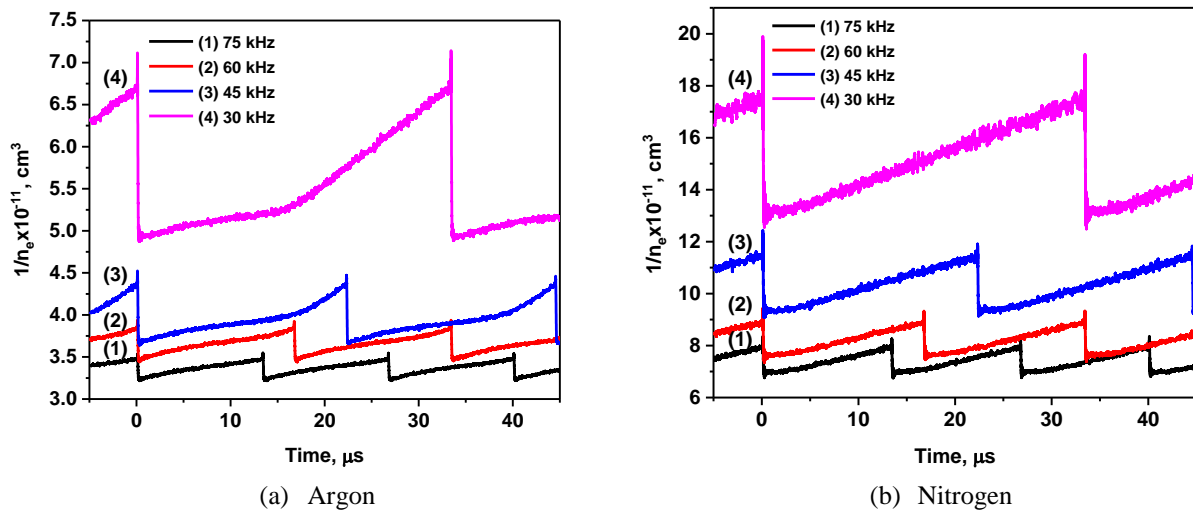


Figure 2.8. Inverse electron number density as a function of time in (a) argon and (b) nitrogen plasma at different PRF for $p=3$ Torr, $m=1.45$ g/min.

From figure 2.8a, it is evident that at pulse repetition frequencies of 30 and 45 kHz for argon, a distinct transition in recombination rate occurs at $16 \mu\text{s}$. Prior to this time, changes in $1/n_e$ are minimal while afterwards $1/n_e$ appears to linearly increase with time indicating a second-order decay of n_e . In nitrogen, such transition phenomenon is not as pronounced in figure

2.8b but a small constant region 1-3 μs after the pulse does exist. After this region, $1/n_e$ also clearly linearly increases. Accordingly, for both gases, the effective electron-ion recombination rate was extracted from the linear slope regions and suggests dissociative recombination as the process responsible for the observed electron decay. The inferred rate coefficients are presented in table 2.1 and compared with the values found in the literature.

As a first approximation, it can be assumed that the primary ions with which electrons recombine just after the HV pulse are dimer ions, Ar_2^+ , in argon and nitrogen ions, N_2^+ , in nitrogen, and that most of the recombination occurs when the electrons are thermalized, i.e. $T_e=300$ K. It is apparent that within the uncertainty of this experiment and of the ones to which β is compared, there is an overall agreement with the rates for argon dimer ions found in literature for $T_e=300$ K. However, the recombination rates in nitrogen are substantially higher than the known value $2 \times 10^{-7} \text{ cm}^3/\text{s}$ [43], indicating that cluster ions may be present.

Table 2.1. Measured dissociative recombination rates and their comparison to the literature data.

	PRF (kHz) for Measured and reference for Literature data	β ($\times 10^{-7} \text{ cm}^3/\text{s}$)	
		Argon	Nitrogen
Measured	30	8.7	13.9
	45	7.3	10.4
	60	-	8.4
	75	-	8.0
Literature data	[62]	7.7-9.3	-
	[63]	8.2-10.0	-
	[60], <3 Torr	-	2 (N_2^+)
	[60], >5 Torr	-	≈ 10 ($\text{N}_3^+, \text{N}_4^+$)
	[58], 3 Torr	-	10-20 (N_4^+)

This is supported by the fact that the recombination rates measured agree with those typical of cluster ions. Indeed, at 3 Torr, in the process $\text{N}_2^+ + \text{N}_2 + \text{N}_2 \rightarrow \text{N}_4^+ + \text{N}_2$, the time that it takes

the concentration of N_2^+ to be reduced by a factor of $e=2.72$ as it converts to N_4^+ , $\tau_{1/e}$, is $\sim 1\mu\text{s}$ as determined by the rate constant found in [58]. Consequently, in 2-3 μs , the concentration of N_2^+ drops by a factor of 10 at which time most of the ions are N_4^+ . The recombination rate of these cluster ions is known to be $2 \times 10^{-6} (300/T_e)^{0.5} \text{ cm}^3/\text{s}$ [58], [60]. At T_e of 600-1900 K, the predicted rate matches the experimental nitrogen recombination rates given in table 2.1. This suggests that the electrons cool to these temperatures in a few microseconds, which is consistent with the time dependent electron temperature decay modeled in [58] for nitrogen plasma at 3 Torr.

From table 2.1, it is also evident that as the PRF is increased, the measured recombination rate decreases. This implies that the time-averaged electron temperature should increase with PRF, as can be expected.

In argon, on the other hand, at electron temperatures of $\sim 3 \text{ eV}$ or lower, the electron energy relaxation is mostly due to elastic collisions with argon atoms. The characteristic time of electron thermalization in argon plasma (i.e. the time in which the difference between the electron and gas temperatures reduces by a factor of e) can be estimated as [43]

$$\tau_\varepsilon = \frac{1}{\nu_m \delta} \quad (2.6)$$

where ν_m is the electron-molecule momentum transfer frequency, and δ is the mean fraction of electron energy transferred to a molecule in one collision. For argon, $\delta = 2m/M = 2.74 \times 10^{-5}$ [43], where m and M are the masses of electron and atom, respectively. Therefore, in 6-8 μs the electron temperature should drop from $\sim 3\text{-}5 \text{ eV}$ or so in the pulse to a fraction of eV. However, subsequent electron temperature relaxation in argon should be very slow due to the Ramsauer-Townsend minimum in the electron transport cross section at electron energies on the order of 0.1 eV. Thus, the full thermalization of electrons in 16 μs implied by the experimental data in argon could mean that in the experiments some molecular impurity in argon was present, possibly

due to outgassing from the acrylic caps of the chamber. Moreover, the formation of Ar_2^+ through ion conversion $Ar^+ + Ar + Ar \rightarrow Ar_2^+ + Ar$ has a rate constant of 2.5×10^{-31} cm⁶/s [64]. At a pressure of 3 Torr, $\tau_{1/e}$ for Ar_2^+ formation is ≈ 400 μ s, much longer than the 16 μ s it takes to transition to a faster recombination rate in figure 2.8a. Therefore, additional recombination mechanisms, possibly involving molecular impurities, should be considered to better understand the observed transition in rates in the data. Detailed analysis of these possibilities, as well as detailed kinetic modeling of electron temperature relaxation and number density decay, has been performed.

3. KINETIC MODELING

Large portions of this chapter were reprinted from V. Podolsky and S. Macheret, “Plasmas sustained by repetitive nanosecond pulses: recombination mechanisms in Ar with trace amounts of H₂O,” *Plasma Sources Sci. Technol.*, vol. 28, no. 5, p. 055008, 2019. © IOP Publishing. Reproduced with permission. All rights reserved.

3.1 Kinetic Model Introduction

High-voltage (HV), repetitive, nanosecond pulses can efficiently generate plasmas with high electron number densities, n_e , and large quantities of excited species [45]. By utilizing high pulse repetition frequencies (PRF), the decay of charged species between the pulses can be minimized, thereby producing a periodic quasi-continuous plasma [45]. One emerging application of such plasmas is to plasma antennas. Conventional DC and RF plasmas have electron temperatures, T_e , on the order of 1-5 eV, resulting in high levels of Johnson-Nyquist thermal noise proportional to the charge carrier temperature (i.e. T_e) [65]. Plasmas sustained by high PRF could remedy this problem, for, in between the pulses, the electron temperature can thermalize more rapidly than the decay of electron density. Therefore, a quasi-continuous plasma with sufficiently high electron number densities and low mean electron temperature can potentially be utilized to produce a low-noise plasma antenna.

To investigate the decay of such a plasma, microwave interferometry experiments on argon and nitrogen plasmas sustained by 800 V, 3 ns FWHM pulses at PRF = 30 -75 kHz at a gas pressure of 3 Torr were performed in [66]. An initial analysis of the nitrogen plasma showed that the quick thermalization and subsequent decay could solely be explained by the dissociative recombination of N_4^+ . However, a similar analysis of the argon plasma results suggested that the rapid thermalization and the decay of electron density could only be explained by the presence of molecular impurities. It is believed that these impurities were introduced via outgassing and

permeation through the acrylic walls of the vacuum chamber. Acrylic is known to be a readily hygroscopic material, and therefore it is believed that trace amounts of H₂O were likely present.

We have also explored the possibility of nitrogen and oxygen as molecular impurities but determined that they could not explain the measured decay rates. The dissociative recombination rate of N₂⁺ and O₂⁺ are too slow compared to the measured experimental rates in argon plasma. Cluster ions of these species have the appropriate recombination rates but since only trace amounts of these impurities (<0.1%) could have been present, the formation of these cluster ions was unlikely. Dissociative attachment and three-body attachment to oxygen and water was considered, but these processes were also found insignificant at a pressure of 3 Torr.

Therefore, we have developed a kinetic model to understand the experimental results in argon and the effect of water vapor as a molecular impurity in the afterglow of a pulse. In the subsequent section, we first describe the key assumptions and list the relevant ion conversion and electron-ion recombination processes. We then describe the electron energy equation with processes involving both Ar and H₂O. Then we explore which argon-electron recombination mechanisms would be possible on the time scale between the ionizing pulses and formulate the rate equations for the argon and water ions. The final rate equation of electron recombination is then derived incorporating the dominant processes involving argon species and the added influence of water species. Finally, the kinetic model incorporating the energy and rate equations is compared with the experimental data.

3.2 Model Description

In creating the model, the following assumptions were made. A 0-D approximation was used since, under the experimental conditions, it can be shown that the fast electron heat conduction equilibrates the electron temperature throughout the centimeter-scale plasma in approximately 100

ns or so after the culmination of a pulse. The electron-ion densities can also be assumed quasi-uniform within the quasi-neutral plasma, and the effect of ambipolar diffusion can be incorporated via an effective loss rate (see Section 3.4 and [43]). A Maxwellian electron energy distribution function (EEDF) was used when computing electron-molecule collision frequencies. Such an EEDF is appropriate, for after a pulse, the electrons would have sufficiently low energy and the influence of the high-energy tail of the EEDF should be insignificant. In solving the electron energy equation, it was assumed that the gas temperature, T , remains constant at 300 K, consistent with low average energy input in [66]. The reactions considered to explain the observed rate of electron recombination between pulses are given in table 3.1

Table 3.1. Reactions considered in this model. The reactions marked in bold font were shown to be negligible for electron recombination at the experimental conditions [66].

Reaction	Process	Rate Coefficient (cm ³ /s), # (cm ⁶ /s)	Ref
<i>Ar Reactions</i>			
(R1) Stepwise Ionization	$e + \text{Ar}^* \rightarrow \text{Ar}^+ + 2e$	$k_1 = 1 \times 10^{-10} T_e^3 \exp(-4.16/T_e)$	[67]
(R2) Ar_2^+ Dissociative Recombination	$e + \text{Ar}_2^+ \rightarrow \text{Ar}^* + \text{Ar}$	$k_2 = 9.8 \times 10^{-8} (T_e)^{-0.61}$	[63]
(R3) Recombination	$e + \text{Ar}^+ \rightarrow \text{Ar}^*$	$k_3 = 4.0 \times 10^{-13} (T_e)^{-0.5}$	[67]
(R4) Ar* De-excitation	$e + \text{Ar}^* \rightarrow e + \text{Ar} + \Delta\varepsilon$	$k_4 = 1 \times 10^{-11} (T_e)^{-0.75}$	[67]
(R5) Three Body Recombination	$e + e + \text{Ar}^+ \rightarrow \text{Ar}^* + e$	$k_5^\# = 5.0 \times 10^{-27} (T_e)^{-4.5}$	[67]
(R6) Ar_2^+ Formation	$\text{Ar}^+ + \text{Ar} + \text{Ar} \rightarrow \text{Ar}_2^+ + \text{Ar}$	$k_6^\# = 2.5 \times 10^{-31}$	[67]
(R7) Metastable Associative Ionization	$\text{Ar}^* + \text{Ar}^* \rightarrow \text{Ar}^+ + \text{Ar} + e$	$k_7 = 5.0 \times 10^{-10}$	[67]
(R7a) Ar* Quenching by H₂O	$\text{Ar}^* + \text{H}_2\text{O} \rightarrow \text{Ar} + \text{H}_2\text{O}$	$k_{7a} = 4.8 \times 10^{-10}$	[68]
<i>H₂O Reactions</i>			
(R8) $\text{Ar}^+, \text{H}_2\text{O}$ Charge Exchange	$\text{Ar}^+ + \text{H}_2\text{O} \rightarrow \text{H}_2\text{O}^+ + \text{Ar}$	$k_{8a} = 7 \times 10^{-10}$ $k_{8b} = 1.5 \times 10^{-10}$	[69] [70]
(R9) H_2O^+ Ion Conversion	$\text{H}_2\text{O}^+ + \text{H}_2\text{O} \rightarrow \text{H}_3\text{O}^+ + \text{OH}$	$k_{9a} = 1.85 \times 10^{-9}$ $k_{9b} = 1.30 \times 10^{-9}$	[69] [70]
(R10) H_2O^+ Dissociative Recombination	$\text{H}_2\text{O}^+ + e \rightarrow \text{products}$	$k_{10} = 6.9 \times 10^{-8} (T_e)^{-0.5}$	[69]
(R11) H_3O^+ Dissociative Recombination	$\text{H}_3\text{O}^+ + e \rightarrow \text{products}$	$k_{11} = 9.9 \times 10^{-8} (T_e)^{-0.7}$	[69]
(R12) ArH^+ Formation	$\text{Ar}^+ + \text{H}_2\text{O} \rightarrow \text{ArH}^+ + \text{OH(X)}$	$k_{12} = 1.31 \times 10^{-9}$	[70]
(R13) ArH^+ Ion Conversion	$\text{ArH}^+ + \text{H}_2\text{O} \rightarrow \text{Ar} + \text{H}_3\text{O}^+$	$k_{13} = 4.9 \times 10^{-9}$	[70]
(R14) H^+ Formation	$\text{Ar}^+ + \text{H}_2\text{O} \rightarrow \text{H}^+ + \text{OH} + \text{Ar}$	$k_{14} = 3.1 \times 10^{-10}$	[69]
(R15) $\text{H}^+, \text{H}_2\text{O}$ Charge Exchange	$\text{H}^+ + \text{H}_2\text{O} \rightarrow \text{H}_2\text{O}^+ + \text{H}$	$k_{15} = 6.9 \times 10^{-9}$	[69]
(R16) OH^+ Formation	$\text{Ar}^+ + \text{H}_2\text{O} \rightarrow \text{H} + \text{OH}^+ + \text{Ar}$	$k_{16} = 4.2 \times 10^{-10}$	[69]
(R17) $\text{OH}^+, \text{H}_2\text{O}$ Charge Exchange	$\text{OH}^+ + \text{H}_2\text{O} \rightarrow \text{H}_2\text{O}^+ + \text{OH}$	$k_{17} = 1.5 \times 10^{-9}$	[69]
(R18) OH^+ Ion Conversion	$\text{OH}^+ + \text{H}_2\text{O} \rightarrow \text{H}_3\text{O}^+ + \text{O}$	$k_{18} = 1.3 \times 10^{-9}$	[69]

In modelling the interaction of argon ions with the water vapor impurities present, we considered two sets of reactions and corresponding rates— one set from [69] and the other from [70]. It was found that utilizing each set independently yielded good fits to our experimental data at similar concentrations of H₂O. Therefore, unless otherwise noted, we focus our discussion on the reactions and rates presented in [69]. Note that the H₂O⁺ and H₃O⁺ dissociative recombination rates (k_{10} and k_{11}) were taken only from [69] as the rates for these processes provided in [70] are not given as function of electron temperature.

The processes of electron attachment can be neglected in the conditions of experiments [66]. Indeed, dissociative attachment processes $e + \text{H}_2\text{O} \rightarrow \text{OH} + \text{H}^-$, $e + \text{H}_2\text{O} \rightarrow \text{H}_2 + \text{O}^-$, and $e + \text{H}_2\text{O} \rightarrow \text{OH}^- + \text{H}$ (reactions R83, R84, and R85, respectively, in [69]) have high energy thresholds of 6.1-7.6 eV (R83 and R84 of [69]) and a low pre-exponential factor (R85 of [69]). Since the electron temperature is low during most of the time between the pulses, this leads, in combination with the low concentration of H₂O, to electron losses in attachment being significantly lower than those due to recombination with H₃O⁺ (cf. figure 3.7).

3.3 Electron Energy Equation

In the afterglow of a pulse, because reaction rate coefficients depend on T_e , it is necessary to model the behavior of the electron temperature. The time dependent decay of T_e can be obtained by solving the average electron energy equation: we have included elastic collisions of electrons with neutral argon atoms, the excitation of argon to an excited electronic state, and the excitation of the rotational as well as vibrational modes of water molecules. This equation can be written as

$$\frac{dT_e}{dt} = -(T_e - T) \delta v_m - \frac{2}{3} v_{el} \Delta \varepsilon_{el} \left[1 - \exp \left(-\Delta \varepsilon_{el} \left(\frac{1}{T} - \frac{1}{T_e} \right) \right) \right] \quad (3.1)$$

$$\begin{aligned}
& -\frac{2}{3} \nu_{rot} \Delta \varepsilon_{rot} \left[1 - \exp \left(-\varepsilon_{rot} \left(\frac{1}{T} - \frac{1}{T_e} \right) \right) \right] \\
& -\frac{2}{3} \nu_{vib,s} \Delta \varepsilon_{vib,s} \left[1 - \exp \left(-\Delta \varepsilon_{vib,s} \left(\frac{1}{T} - \frac{1}{T_e} \right) \right) \right] \\
& -\frac{2}{3} \nu_{vib,b} \Delta \varepsilon_{vib,b} \left[1 - \exp \left(-\Delta \varepsilon_{vib,b} \left(\frac{1}{T} - \frac{1}{T_e} \right) \right) \right]
\end{aligned}$$

where δ is the mean fraction of electron energy lost per elastic momentum-transfer collision, ν_m is the electron-atom momentum transfer collision frequency, ν_{el} is the frequency of electronic excitation of argon atoms, and $\Delta \varepsilon_{el}$ is the energy of the argon electronic state. We only consider transitions to and from the first argon excited state, $\Delta \varepsilon_{el} = 11.55$ eV [71]. For the electron energy lost in elastic collisions, $\delta = \frac{2m}{M}$ where m and M are the electron and atom mass, respectively, so that $\delta = 2.74 \times 10^{-5}$ for argon [43].

The collision frequencies of electrons with water molecules that cause excitation of H₂O rotational, vibrational stretching and vibrational bending modes are ν_{rot} , $\nu_{vib,s}$, $\nu_{vib,b}$, respectively. The corresponding threshold transition energies from the ground to the first rotational ($J = 0 \rightarrow 1$) and vibrational level ($\nu = 0 \rightarrow 1$) are $\Delta \varepsilon_{rot}$, $\Delta \varepsilon_{vib,s}$, $\Delta \varepsilon_{vib,b}$, the values for which are $\Delta \varepsilon_{rot} = 0.0046$ eV, $\Delta \varepsilon_{vib,s} = 0.4595$ eV, and $\Delta \varepsilon_{vib,b} = 0.1977$ eV [72]. The value used for $\Delta \varepsilon_{vib,s}$ is an average of the symmetric and asymmetric mode quanta. To obtain the forms of the electronic, rotational and vibrational terms in the energy equation (3.1), we used the detailed balance principle so that when $T_e = T$, the system is at equilibrium and no energy exchange occurs.

In equation (3.1), it was assumed that not only the rotational, but also vibrational temperatures of H₂O are equal to T because (a) the vibrational relaxation of H₂O in collisions with Ar is very fast, with the room-temperature rate coefficient of about 3×10^{-13} cm³/s [73], (b) due to the low electron temperature during most of the time between the pulses (see the results below),

the time-averaged rate coefficient for electron-impact vibrational excitation does not exceed $\sim 10^{-9}$ cm³/s, and (c) the ionization fraction is low, on the order of 10^{-7} . Simple calculations show that for the conditions of the experiments [66], the vibrational temperature of the bending mode of H₂O is very close to the room temperature, while the temperature of the stretch modes is about 600-700 K. Since the characteristic temperature of the stretch modes is about 5300 K, the population of vibrationally-excited states in the stretch modes is negligible as if it would have been had the vibrational temperature been fully equilibrated with the gas temperature. This justifies the assumption of full vibrational equilibration of water molecules in the conditions considered in [66] and in this work.

For argon, electron-ion collisions should not play a significant role as an electron energy loss mechanism since the ionization fraction in the experiments [3] is on the order of 10^{-7} for $n_e \approx 10^{10}$ cm⁻³ at 3 Torr.

Evaporative cooling of electrons as a mechanism of thermalization was also considered. In equation (6) of [74], the authors derived an expression for the characteristic time, τ_e , of this process, defined as $\tau_e = \left(\frac{1}{T_e} \frac{dT_e}{dt} \right)^{-1}$. In [74], the 3D geometry was that of a cube with the side length $L=50$ cm. In contrast, in our experiments [66] the geometry was that of two parallel discs, the spacing ($L=2$ cm) between which was much smaller than the disc diameter making the diffusion processes essentially one-dimensional. Therefore, for our conditions, the characteristic time, τ_e , computed with equation (6) of [74] should be multiplied by a factor of 3. We thus estimated this characteristic time for our experimental conditions [66] at 3 Torr (a factor of 400 higher than that considered in [74]), and for $T_e=3$ eV, 1 eV, 0.5 eV, and 0.2 eV, we obtained $\tau_e=40$ μ s, 120 μ s, 234 μ s, and 567 μ s, respectively. Since τ_e indicates the time in which the temperature will drop by only a factor of $e=2.718$, evaporative electron cooling at these temperatures cannot explain the complete

thermalization of electrons to room temperature within the $\sim 16 \mu\text{s}$ observed in our experiments [66] (see also figures 3.3, 3.4, and 3.5 and the discussion in section 3.5.2 below) and is substantially longer than the period between two pulses ($33.3 \mu\text{s}$) [66]. Moreover, as shown in [75], the model developed in [74] overpredicts the rate of evaporative cooling of electrons, and thus the actual characteristic time τ_e is even longer than estimated, indicating that evaporative cooling of electrons does not play a role under our experimental conditions.

Superelastic collisions of electrons with metastable argon atoms (R4), Ar^* , were also considered since energy that can heat the electrons is released as the metastable atoms return to the ground state. To understand if such heating of electrons is significant, consider a comparison between this process and the rate of electron temperature decay through elastic collisions with argon at $T_e = 1 \text{ eV}$. Assuming $T_e \gg T$, and approximating $\nu_m \approx 1.59 \times 10^{10} \text{ s}^{-1}$ at $p = 3 \text{ Torr}$ [43], the rate of T_e decay for elastic collisions can be estimated to be $4.36 \times 10^5 \text{ eV/s}$. The rate of electron heating can be estimated by $\frac{2}{3}k_4 n_{\text{Ar}^*} \Delta\varepsilon^*$ where $\Delta\varepsilon^* = 11.55 \text{ eV}$ is the energy released per superelastic collision and n_{Ar^*} is the number density of argon metastable atoms. At the same T_e , even assuming $n_{\text{Ar}^*} \approx 10^{11} \text{ cm}^{-3}$ (the highest conceivable value, estimated for pure Ar plasma), this heating rate is only $\approx 8 \text{ eV/s}$. Comparing these two estimations, it is clear that electron thermalization even in elastic collisions dominates any superelastic heating by five orders of magnitude. Therefore, even if the electron temperature and n_{Ar^*} are each an order of magnitude higher, decay through elastic collisions would still dominate. As such, superelastic collisions are insignificant.

To solve the energy equation, it was necessary to incorporate the concentration of H_2O within the collision frequency terms:

$$v_{m,el} = (1 - \chi)N\langle\sigma_{m,el}v_e\rangle \quad (3.2a)$$

$$v_{rot,vib} = n_{H_2O}\langle\sigma_{rot,vib}v_e\rangle = \chi N\langle\sigma_{rot,vib}v_e\rangle \quad (3.2b)$$

where v_e is the velocity of electrons, n_{H_2O} is the number density of water, χ is the mole fraction of H_2O , and $\sigma_{m,el,rot,vib}$ is the cross section for collisions of electrons with argon and water for the relevant process indicated in the subscript. In equations (3.2a) and (3.2b), $N = n_{Ar} + n_{H_2O}$ and is the total number density of particles at the experimental pressure and temperature.

When computing the collision frequencies as functions of T_e , the fit of the momentum transfer cross section was taken from [76], the electronic excitation cross section for argon was obtained by fitting data from [71], while the rotational and vibrational cross sections of water were obtained by fitting the data presented in [77].

3.4 Continuity Equation

The recombination of electrons and ions in the afterglow between the pulses is governed by the continuity equation

$$\frac{\partial n}{\partial t} + \nabla \cdot \Gamma = q \quad (3.3)$$

where n is the electron and ion number density, q is the source term which includes all of the processes responsible for electron and ion production and decay, and Γ is the diffusion flux term given by $\Gamma = -D_a \nabla n$ where D_a is the ambipolar diffusion coefficient. As recommended in [43], the continuity equation can be reduced to zero-dimensional one by using the approximation $D_a \nabla n = -\frac{D_a}{\Lambda_D^2} n$, which is used in our model. The inverse square of characteristic diffusion length, $1/\Lambda_D^2$, was estimated as described in [43]. For an electrode spacing of 2 cm and side lengths of

10.16 cm (the geometry of the experiment [66]) $1/\Lambda_D^2$ was found to be 2.66 cm^{-2} . Note that the drift term was not included in equation (3.3) as there is no electric field in the plasma afterglow.

The ambipolar diffusion coefficient is determined as [43]

$$D_a = \frac{D_e \mu_i + D_i \mu_e}{\mu_e + \mu_i} \quad (3.4)$$

where D_e and D_i are the electron and ion diffusion coefficients, while μ_e and μ_i are the electron and ion mobilities, respectively. D_e and D_i are given by the Einstein relations. μ_e is related to v_m by [43]

$$\mu_e = \frac{q}{m_e v_m} \quad (3.5)$$

where q is the electron charge. The ion mobility μ_i was calculated [78] as the weighted average of the mobilities of all ions present in significant concentrations. The reduced mobilities of the key ions are: $\mu_{O,Ar^+} = 1.52 \frac{\text{cm}^2}{\text{Vs}}$ [68], $\mu_{O,Ar_2^+} = 1.83 \frac{\text{cm}^2}{\text{Vs}}$ [68], $\mu_{O,H_3O^+} = 2.92 \frac{\text{cm}^2}{\text{Vs}}$ [79], $\mu_{O,H_2O^+} = 2.71 \frac{\text{cm}^2}{\text{Vs}}$ [79]. These values were taken from the indicated references for an electric field of 0 V/cm and used with experimental pressure and gas temperature to determine the corresponding mobilities.

3.4.1 Rate Equations

The full continuity equation characterizing the decay of n_{Ar^+} is

$$\begin{aligned} \frac{dn_{Ar^+}}{dt} = & k_1 n_e n_{Ar^*} - k_3 n_e n_{Ar^+} - k_6 n_{Ar}^2 n_{Ar^+} - k_5 n_e^2 n_{Ar^+} - (k_8 + k_{14} + k_{16}) n_{H_2O} n_{Ar^+} \\ & - \frac{D_a}{\Lambda_D^2} n_{Ar^+} \end{aligned} \quad (3.6)$$

It is possible to simplify this expression by comparing the characteristic time, τ , of each process at high and low T_e . The characteristic time τ is the amount of time it takes the density of a species to

fall by a factor of e . Numerical estimates indicate that the characteristic times for R1, R3, and R4 are much longer than that of R5. Comparing ambipolar diffusion to Ar^+ ion conversion indicates that at $T_e < 2$ eV, ion conversion dominates. Due to the presence of electron energy loss through electronic excitation of argon at high T_e , the electron temperature is expected to drop to $T_e < 2$ eV within 1-2 microseconds after the pulse. Therefore, ambipolar diffusion can be neglected. Applying these simplifications to equation (3.5) gives

$$\frac{dn_{\text{Ar}^+}}{dt} = -k_6 n_{\text{Ar}}^2 n_{\text{Ar}^+} - (k_8 + k_{14} + k_{16}) n_{\text{H}_2\text{O}} n_{\text{Ar}^+} \quad (3.7)$$

Regarding argon dimer ions, under the conditions of the experiment [66], the production of Ar_2^+ is due to the Ar^+ ion conversion (R6). Ambipolar diffusion is negligible since it is comparable to Ar_2^+ dissociative recombination (R2) only at $T_e > 1$ eV, i.e. only within ~ 1 μs after the pulse. Combining these mechanisms gives a simple rate equation describing the decay of argon dimer ions

$$\frac{dn_{\text{Ar}_2^+}}{dt} = k_6 n_{\text{Ar}}^2 n_{\text{Ar}^+} - k_2 n_e n_{\text{Ar}_2^+} \quad (3.8)$$

It is also important to consider the role of metastable ions in the afterglow. The characteristic time of stepwise ionization (R1) as a loss mechanism for Ar^* is comparable to or less than the characteristic time of metastable associative ionization (R7) only at electron temperatures of at least 5 eV for the electron number density measured in this experiment. Such high T_e are expected to be present only during the pulse. Similarly, Ar^* de-excitation (R4) only plays a role for metastable destruction at unrealistically high T_e . Therefore, R7 and R7a dictate the decay of Ar^* by

$$\frac{dn_{\text{Ar}^*}}{dt} = -k_7 n_{\text{Ar}^*}^2 - k_{7a} n_{\text{Ar}^*} n_{\text{H}_2\text{O}} \quad (3.9)$$

The rate equations involving water related species are given in equations (3.10)-(3.13). In general, the presence of H₂O in the argon plasma causes the formation of H₂O⁺ as well as the direct and indirect formation of H₃O⁺, both of which can in turn recombine with electrons. We will show that under the conditions of the experiment [66], dissociative recombination with H₃O⁺ will serve as the main loss mechanism of electrons.

$$\frac{dn_{H_2O^+}}{dt} = k_8 n_{Ar^+} n_{H_2O} + k_{15} n_{H^+} n_{H_2O} + k_{17} n_{OH^+} n_{H_2O} - k_{10} n_e n_{H_2O^+} - k_9 n_{H_2O^+} n_{H_2O} - \frac{D_a}{\Lambda_D^2} n_{H_2O^+} \quad (3.10)$$

$$\frac{dn_{H_3O^+}}{dt} = k_9 n_{H_2O^+} n_{H_2O} + k_{18} n_{H_2O} n_{OH^+} - k_{11} n_e n_{H_3O^+} - \frac{D_a}{\Lambda_D^2} n_{H_3O^+} \quad (3.11)$$

$$\frac{dn_{OH^+}}{dt} = k_{16} n_{H_2O} n_{Ar^+} - (k_{17} - k_{18}) n_{H_2O} n_{OH^+} - \frac{D_a}{\Lambda_D^2} n_{OH^+} \quad (3.12)$$

$$\frac{dn_{H^+}}{dt} = k_{14} n_{H_2O} n_{Ar^+} - k_{15} n_{H_2O} n_{H^+} - \frac{D_a}{\Lambda_D^2} n_{H^+} \quad (3.13)$$

Lastly, we derive the rate equation governing electron recombination between pulses. The main electron loss processes were found to be dissociative recombination with Ar₂⁺, H₂O⁺, and H₃O⁺, with ambipolar diffusion playing a role in < 1 μs just after the pulse. Since the ion conversion Ar⁺ → H₂O⁺ → H₃O⁺ occurs rapidly, and H₃O⁺ will be the dominant ion in the afterglow under the experimental conditions [66], the ambipolar diffusion coefficient can be determined using the mobility of H₃O⁺. (Additionally, there is little difference in the mobility of H₃O⁺ and the other ions present). Electron production through metastables is also incorporated by

$$\frac{dn_e}{dt} = k_7 n_{Ar^*} n_{Ar^*} - k_2 n_e n_{Ar_2^+} - k_{10} n_e n_{H_2O^+} - k_{11} n_e n_{H_3O^+} - \frac{D_a}{\Lambda_D^2} n_e \quad (3.14)$$

Calculations with the highest conceivable density of metastables (expected in pure Ar) $n_{Ar^*} = 1 \times 10^{11} \text{ cm}^{-3}$, showed that even at this high metastable density the reaction (R7) does not play any significant part in the electron balance in the afterglow. Since the density of metastables is likely to be much lower due to the fast quenching by H₂O in (R7a), the processes involving Ar^{*}

can be disregarded for the purposes of this work. The simplified electron density decay equation can then be written as

$$\frac{dn_e}{dt} = -k_2 n_e n_{Ar_2^+} - k_{10} n_e n_{H_2O^+} - k_{11} n_e n_{H_3O^+} - \frac{D_a}{\Lambda_D^2} n_e \quad (3.14.1)$$

3.4.2 Solving the Balance Equations

To solve the continuity equations, it is necessary to know the initial number densities of the electrons and ions at the start of the afterglow. The initial electron number density in the afterglow, $n_{e,o}$, is obtained from experimental measurements [66]. The ion initial densities were determined in an iterative manner where the initial ion number density of the $(i+1)^{th}$ iteration, $n_{i,o_{i+1}}$, was determined by

$$n_{i,o_{i+1}} = \frac{n_{i,o_i} + n_{i,f_i}}{2} \quad (3.15)$$

where n_{i,o_i} and n_{i,f_i} is the initial and final ion concentration, respectively, of a given ion in the afterglow of the i^{th} iteration.

While applying this iterative process, we assume that only Ar^+ is produced during the pulse since only a trace amount of H_2O exists in the gas when a pulse is applied; therefore, a slightly different approach in the iterative technique for Ar^+ is utilized:

$$n_{Ar_o^+_{i+1}} = \frac{(n_{Ar_o^+_{i+1}} - \Delta n_e) + n_{Ar_f^+_{i+1}}}{2} + \Delta n_e \quad (3.16)$$

where Δn_e is the measured change in electron density between the start and end of a pulse. Under this assumption, the number densities of the other ions at the end of the afterglow are equal to their densities at the start of the afterglow. Therefore the iterations are continued until $n_{i,o_i} = n_{i,f_i}$ and $n_{Ar_o^+_{i+1}} - \Delta n_e = n_{Ar_f^+_{i+1}}$ while enforcing quasi-neutrality within the afterglow.

A good set of starting values for this iterative process can be obtained by approximating the quasi-steady concentrations of the ions. To do so, the rate equations (3.7), (3.8), and (3.10)- (3.13) are each first set to zero and a ratio of number densities is found. For example, consider equation (3.8). Equating it to zero, the ratio of Ar_2^+ to Ar^+ is

$$\frac{n_{\text{Ar}_2^+}}{n_{\text{Ar}^+}} = \frac{k_6 n_{\text{Ar}}^2}{k_2 \bar{n}_e} \quad (3.17)$$

where \bar{n}_e is the experimental quasi-steady mean electron number density averaged over the duration of a pulse. Repeating this process for the rate equations of the other ions gives their quasi-steady ratios. These ratios were solved simultaneously while enforcing quasi-neutrality to give an initial guess of their starting point concentrations. Note that it is still necessary to add Δn_e to the initial concentration of Ar^+ determined in this manner. In solving the system of algebraic equations for the initial-guess ion concentrations, it was assumed that $T_e = T$ in order to compute the rate constants. Indeed, in the following section we will show that in the presence of small amounts of water, the electrons thermalize completely by the end of the afterglow, validating this assumption.

3.5 Results and Discussion

The electron energy equation was solved using MATLAB's ode15s stiff integrator while the system of continuity equations was solved numerically using Euler's method with a time step of 2.5 ns. The time interval starts at the end of the current pulse and ends at the beginning of the subsequent pulse. The initial electron temperature, $T_{e,o}$, was chosen to be 5 eV, but additional calculations showed no difference in the results as the initial electron temperature was varied from 1 eV to 10 eV.

3.5.1 Electron Temperature Decay

First, consider the solution to equation (3.1) in pure Ar, without any water impurities. Figure 3.1 compares the energy transfer through only elastic collisions of electrons with argon atoms to that of including Ar electronic excitation by electron impact. Clearly the inclusion of electronic excitation causes the characteristic decay time (the time in which the electron temperature drops by a factor of e) to be reduced to 50 ns compared to 3.9 μ s for only elastic collisions. Consequently, even if the initial electron temperature is in the range of 10 – 20 eV just after the pulse, it would quickly relax to 1-2 eV in a fraction of a microsecond.

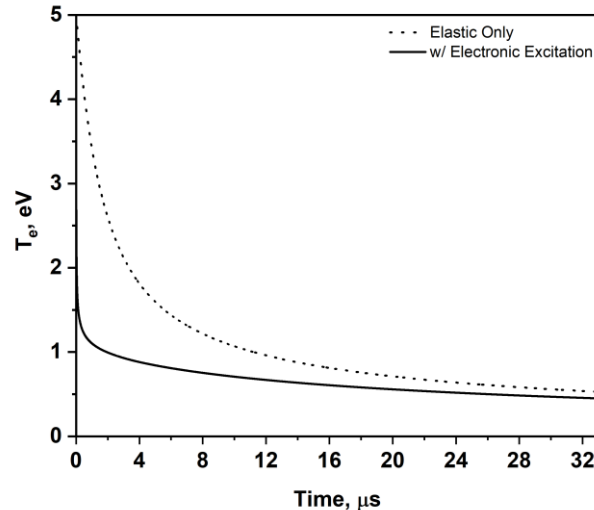


Figure 3.1. Effect of Ar electronic excitation on the relaxation rate of electron temperature.

Once T_e drops to such levels, their cooling begins to level off. Because the mass fraction δ in equation (3.1) is 2.74×10^{-5} , the electrons lose a very small amount of energy in elastic collisions with argon. This is only exacerbated by reduction in the collision frequency ν_m since the electron mean thermal velocity decreases with T_e . A further reduction in ν_m is caused by the Ramsauer-Townsend effect that results in low momentum transfer collisional cross sections at low electron temperatures. The rate constant of electron-argon momentum transfer collisions is shown in figure 3.2. As T_e drops from 5 eV to 0.1 eV, the rate constant decreases by almost two orders of

magnitude. Therefore, it is impossible to achieve complete electron thermalization in pure argon at 3 Torr within 33.3 μs , the longest time between pulses in the experiment [66].

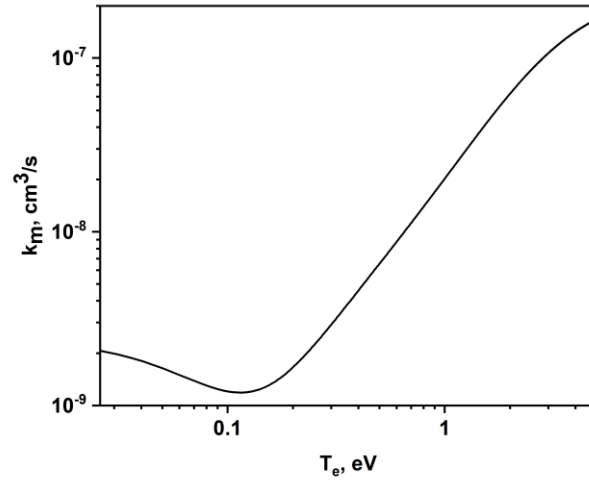


Figure 3.2. Rate constant of electron-argon momentum transfer collisions.

The presence of water vapor enables significant reduction of this long thermalization time. Figure 3.3 shows the solution to equation (3.1) at different water concentrations. As the percentage of H_2O is increased, there is a dramatic decrease in the time it takes the electrons to thermalize: just 0.1% H_2O is enough to drop the thermalization time to 10 μs . Such a phenomenon is due to the electron impact excitation of the rotational and vibrational modes of H_2O . For electron energies between 0.1 and 1 eV, when argon's momentum transfer cross section approaches its minimum, water vapor's ($J = 0 \rightarrow 1$) rotational excitation cross section [77] is four orders of magnitude larger (while its $\nu = 0 \rightarrow 1$ vibrational excitation cross sections [77] are an order of magnitude larger) than the momentum transfer cross sections in argon. These large cross sections, coupled with the much larger energy transferred per collision, are enough to dramatically accelerate the relaxation of electron temperature compared to the case of pure argon plasma.

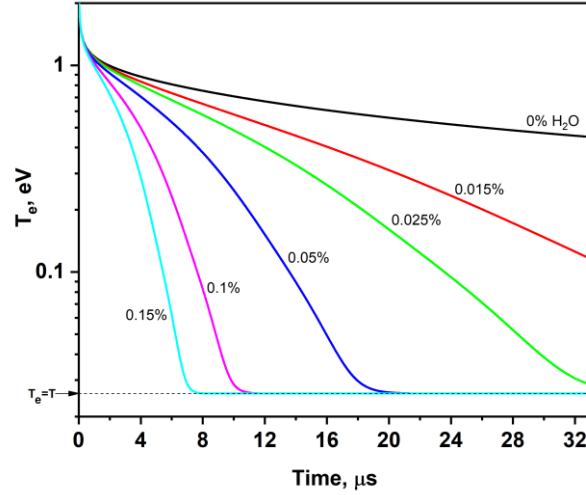


Figure 3.3. Computed electron temperature decay with differing concentrations of H₂O.

Having considered the effect of water impurities on the electron temperature, we can investigate how the effect of small concentrations of H₂O in the kinetic model affect the fit to experimental data. The comparison here is with experimental data [66] taken with PRF= 30 kHz, as faster pulse repetition rates show similar effects. Since the dominant electron loss process is two-body dissociative recombination, i.e. a second-order process, it should, at a constant T_e , be described by a linear dependence of $1/n_e$ vs time t . Therefore, the model is compared with the experimental data plotted in these coordinates.

3.5.2 Comparison to Experimental Data

The comparison with the experimental data assuming pure argon plasma is shown in figure 3.4. The fit is poor because, as previously explained, the electrons will not thermalize between pulses for pure argon on the timescale of this experiment. Nonetheless, even if the electrons were to reach room temperature, they would not experience dissociative recombination with Ar₂⁺ as we previously postulated [66]. Using equation (3.17), we can determine if there would be more Ar⁺ or Ar₂⁺ ions. At 3 Torr, $\bar{n}_e = 1.83 \times 10^{10} \text{ cm}^{-3}$, $n_{Ar} = 9.65 \times 10^{16} \text{ cm}^{-3}$, and $T_e = 300 \text{ K}$, which gives

$k_2 = 9.11 \times 10^{-7} \text{ cm}^3/\text{s}$. Under these conditions, the characteristic time for Ar^+ ions to convert into Ar_2^+ (R6) is $\tau_6 \approx 400 \text{ } \mu\text{s}$, much longer than the time between pulses; therefore, there are ≈ 6 times more Ar^+ than Ar_2^+ under quasi-steady state conditions. This indicates that the electron recombination in the afterglow of pure argon plasma is a very slow process taking place on timescales much longer than the time between the pulses [66].

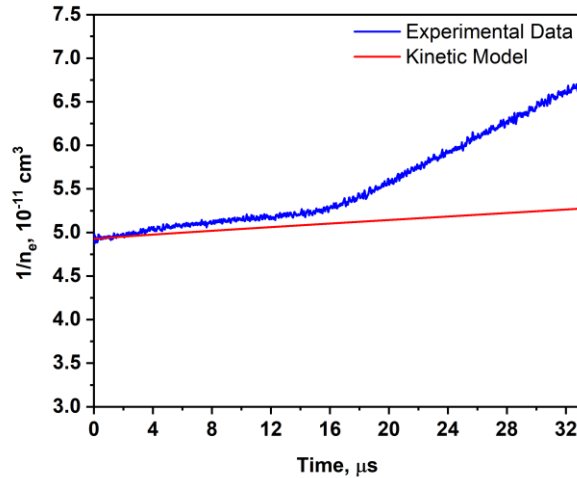


Figure 3.4. Comparison of kinetic model to the experimental data taken at 3 Torr, $\dot{m}=1.45 \text{ g/min}$ without considering H_2O impurities.

In the presence of just trace amounts of H_2O , the electron recombination changes dramatically. Since the exact amount of water vapor in the experiments [66] is unknown and could only be estimated not to exceed 0.1%, the water vapor concentration was varied, and it was found that an excellent agreement with the experimental data is obtained with only $(0.0415 \pm 0.001)\%$ (i.e. 415 ppm) H_2O in our model, as shown in figure 3.5. The modeled electron and ion densities are presented in figure 3.6. The concentration of H_3O^+ steadily and slowly rises until $\approx 16 \text{ } \mu\text{s}$ at which time the electrons have sufficiently thermalized (cf. figure 3.3) allowing the dissociative recombination with H_3O^+ (R11) to dominate all other processes. From figure 3.6, it is also clear that the total concentration of water ions (mainly H_3O^+ and H_2O^+) dominates the concentration of argon ions (Ar^+ and Ar_2^+). Consequently, electrons are more frequently lost through recombination

with H_3O^+ than any other process, as seen in figure 3.7. Such phenomena can be explained as follows.

First, consider the set of ion formation and conversion reactions in table 3.1 taken from [69]. At 3 Torr, even with only 0.02% of H_2O present, the characteristic time for Ar^+ to be converted to H_2O^+ through charge exchange (R8) is $\approx 7.1 \times 10^{-5}$ s (for k_{8a}). This is an order of magnitude faster than Ar_2^+ formation (R6). H_2O^+ would then either decay through dissociative recombination (R10) or form H_3O^+ through ion conversion (R9). Even for thermalized electrons, $T_e = T$, the maximum rate coefficient for (R10) is $k_{10} = 4.29 \times 10^{-7} \text{ cm}^3/\text{s}$ and $\tau_{10} \approx 1 \times 10^{-4}$ s. This is an order of magnitude slower than the $\tau_{9a} \approx 2.7 \times 10^{-5}$ s associated with (R9) indicating that H_2O^+ is mostly converted to H_3O^+ , and dissociative recombination (R11) with the latter is the dominant process by which electrons decay. This is still the case considering the reactions that indirectly form H_2O^+ and H_3O^+ (R14-R18).

The same analysis can be repeated using the set of reactions from [70]. Utilizing k_{8b} instead of k_{8a} , H_2O^+ is formed in $\tau_{8b} \approx 3.3 \times 10^{-4}$ s which is comparable to τ_6 . However, now Ar^+ would also form ArH^+ (R12) with $\tau_{12} \approx 3.82 \times 10^{-5}$ s, about 10 times more quickly than τ_6 . H_2O^+ then converts into H_3O^+ in $\tau_{9b} \approx 3.9 \times 10^{-5}$ s which is still an order of magnitude shorter than its characteristic time to experience dissociative recombination, τ_{10} . The presence of ArH^+ provides an additional channel for H_3O^+ creation through ion conversion (R13) and has $\tau_{13} \approx 1 \times 10^{-5}$ s, which is also ten times shorter than τ_{10} . Thus, H_3O^+ would still be the dominant ion with which electrons recombine.

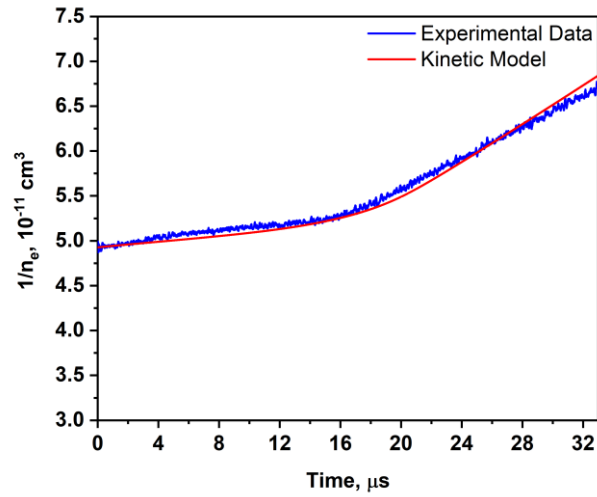


Figure 3.5. Comparison of kinetic model with the experimental argon data taken at 3 Torr, $\dot{m}=1.45$ g/min at 0.0415% H_2O .

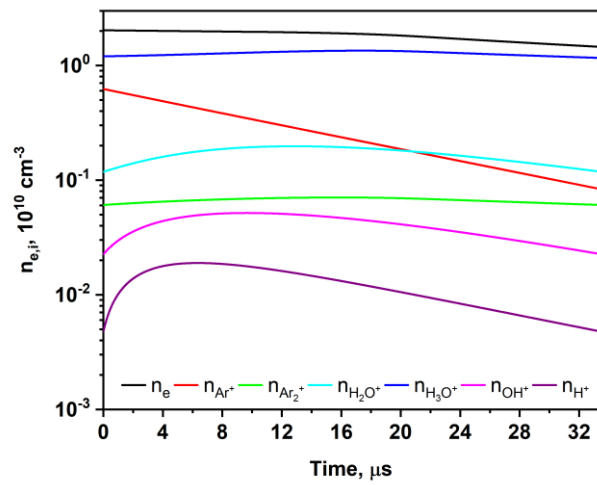


Figure 3.6. Modeled electron and ion densities for argon/water mixture at 3 Torr, $\dot{m}=1.45$ g/min with 0.0415% H_2O .

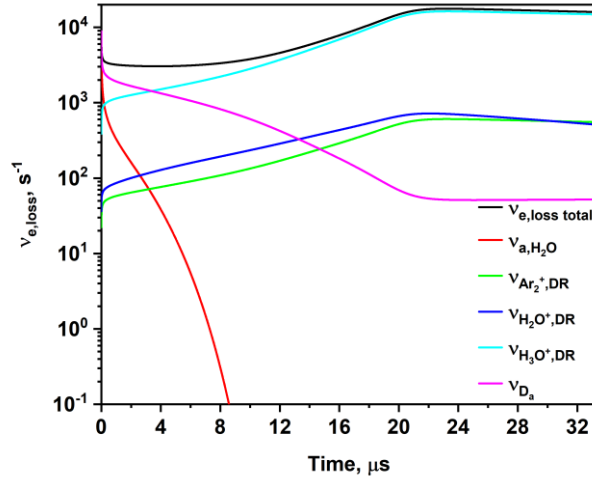


Figure 3.7. Frequency of electron losses at 3 Torr, $\dot{m}=1.45$ g/min with 0.0415% H_2O . Initial losses are due to ambipolar diffusion for the first ~ 4 μs and subsequently due to dissociative recombination (DR) with H_3O^+ . Losses due to attachment ($v_{a,\text{H}_2\text{O}}$) are insignificant.

To further test the theory that trace amounts of water vapor were responsible for the measured electron density decay profiles, the experiment described in [66] was repeated at a flow rate of 2.90 g/min, twice that of the original at the same pressure of 3 Torr. Figure 3.8 shows the experimental data and corresponding calculations under these conditions. Only $(0.024 \pm 0.001)\%$ of H_2O is needed to achieve a good fit of the data which is consistent with the anticipation that the increased flow rate should reduce the residence time of impurities outgassing from the acrylic, thereby decreasing the concentration of the impurity. A comparison of figure 3.5 to figure 3.8 reveals that the minimum value of $1/n_e$ is lower at the faster flow rate meaning that a larger peak n_e is achieved. Indeed, with less water vapor, the rate of electron recombination is slower resulting in larger electron densities to be sustained in the quasi-continuous regime.

In order to further check the model, time-resolved electron density measurements similar to those in [3] were repeated in argon at an increased pressure of 5 Torr but at the same PRF of 30 kHz with flow rates of 1.45 g/min and 2.90 g/min. A good agreement of the model with experimental data is clearly observed in figures 9a and 9b (both within $\pm 0.001\%$). Again, at a

faster flow rate, a smaller concentration of H₂O is needed to achieve a good fit, and the peak density of electrons is higher, consistent with expectations. The peak electron density is lower than that observed at 3 Torr regardless of flow rate (compare figure 9a to figure 5 and figure 9b to figure 8). This can be explained by the fact that the nanosecond pulser peak output voltage is fixed at 800 V, so at higher pressures the effective E/N is lower than it is at lower pressures.

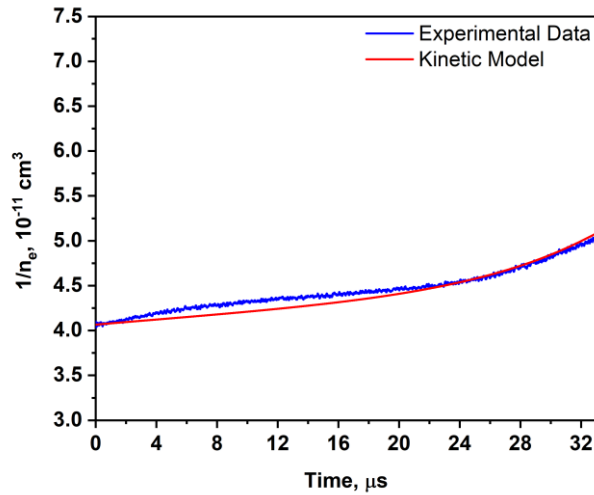


Figure 3.8. Comparison of kinetic model with experimental data taken at 3 Torr, 0.024% H₂O, \dot{m} =2.90 g/min.

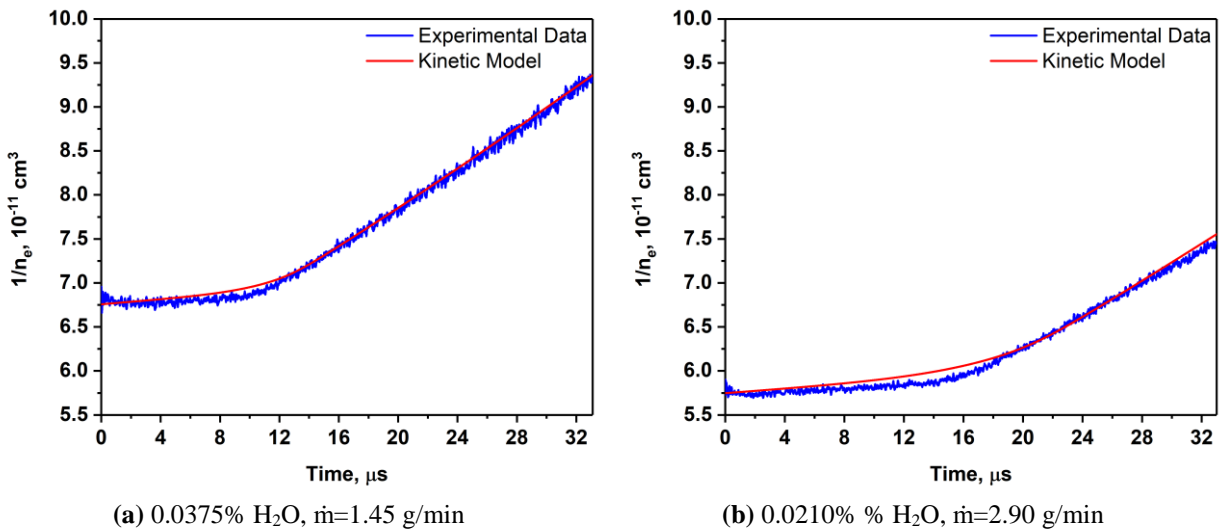


Figure 3.9. Comparison of kinetic model with experimental data taken at 5 Torr.

3.6 Conclusion

A kinetic model was developed to understand the dominant electron recombination mechanisms in the afterglow of a plasma sustained by repetitive nanosecond pulses in argon with small amounts of water impurities.

In pure Ar at $p=3$ Torr, formation of dimer ions takes about $400 \mu\text{s}$, more than an order of magnitude longer than the interval between the ionizing pulses, and thus most of the ions are Ar^+ . Moreover, following the pulse, after an initial rapid drop in electron temperature to 1-2 eV due to excitation of Ar metastables, the subsequent electron temperature relaxation is due to elastic collisions only and is therefore extremely slow (on the order of seconds).

Our model and its comparison with the experimental data demonstrate that even trace amounts (less than 0.1% by volume) of water vapor in Ar dramatically change the mechanism as well as the rates of electron thermalization and recombination. Ar^+ ions are rapidly converted to H_3O^+ (with H_2O^+ as an intermediate species in the process), and the dissociative recombination with H_3O^+ becomes the dominant electron loss mechanism. Electron-impact excitation of rotational and vibrational levels of water molecules accelerates the electron thermalization by orders of magnitude, with full thermalization to room temperature taking only $10 \mu\text{s}$ at $p=3$ Torr and 0.1% of H_2O .

These findings underscore the need for precise control of gas purity in future experiments similar to [66]. On the other hand, the findings show that controlled addition of water vapor (and perhaps other species) to noble gases such as argon can be used, together with the repetitive-pulse ionization technique, to create plasmas with reasonably high electron density and low time-averaged electron temperature.

4. CONDUCTIVITY AND PERMITTIVITY IN THE PLASMA AFTERGLOW

Recall that the conductivity of a plasma is defined as

$$\sigma = \varepsilon_0 \nu_m \frac{\omega_p^2}{\omega^2 + \nu_m^2} \quad (4.1)$$

and the permittivity as

$$\varepsilon_r = 1 - \frac{\omega_p^2}{\omega^2 + \nu_m^2} \quad (4.2)$$

For these plasma properties, there exists a dependency on ω_p , ν_m , and ω . In the afterglow of a plasma, n_e and T_e decay causing a reduction in ω_p and ν_m . The decay of these parameters occurs at different rates. Consider the case of a quasi-steady plasma sustained by ns pulses where, between pulses, it is possible for T_e to fall more rapidly than n_e . Under these conditions, ν_m drops at a rate much faster than the electrons recombine, and, so long as $\omega < \nu_m$, at the completion of a pulse, σ would increase as ν_m approaches ω in the afterglow while ε_r would decrease. Using the experimentally measured n_e decay in argon plasma presented in chapter 2.4 and the corresponding decay of T_e determined from the kinetic model presented in chapter 3, it is possible to derive the conductivity and permittivity in the afterglow of the experimental conditions. The theoretical behavior of σ and ε_r in the afterglow of pure argon was also explored in Appendix A.

4.1 Model Description

In determining $\sigma(T_e)$ and $\varepsilon_r(T_e)$, it is necessary to know $\nu_m(T_e)$. For a mixture of species i , $\nu_m(\varepsilon)$ is defined as

$$\nu_m(\varepsilon) = \nu(\varepsilon) \sum_i N_i \sigma_i(\varepsilon) \quad (4.3)$$

where N is the number of gas molecules, σ_m is the electron-molecule momentum collision cross section, and $v = \sqrt{\frac{2\varepsilon}{m}}$ is the electron speed with mass m . Accounting for the presence of both water and argon present in the experiment, equation (4.3) gives

$$v_m(\varepsilon) = v(\varepsilon) \left[N_{Ar} \sigma_{m,Ar}(\varepsilon) + N_{H_2O} \left(\sigma_{m,H_2O}(\varepsilon) + \sigma_{inelastic,H_2O}(\varepsilon) \right) \right] \quad (4.4)$$

Typically, to find $v_m(T_e)$ equation (4.4) is averaged over the Maxwellian EEDF. However, since 4.1 and 4.2 are nonlinear functions of v_m , substituting $v_m(T_e)$ determined in such a manner directly into those equations would not correctly give $\sigma(T_e)$ and $\varepsilon_r(T_e)$. Instead, equation (4.4) must be inserted into equations (4.1) and (4.2) to give $\sigma(\varepsilon)$ and $\varepsilon_r(\varepsilon)$ which can then be averaged over the Maxwellian EEDF, $f(\varepsilon)$, to obtain $\sigma(T_e)$ and $\varepsilon_r(T_e)$:

$$\sigma(T_e) = \int_0^\infty \varepsilon_o v_m(\varepsilon) \left(\frac{\omega_p^2}{\omega^2 + v_m^2(\varepsilon)} \right) f(\varepsilon) d\varepsilon \quad (4.5)$$

$$\varepsilon_r(T_e) = \int_0^\infty \left(1 - \frac{\omega_p^2}{\omega^2 + v_m^2(\varepsilon)} \right) f(\varepsilon) d\varepsilon \quad (4.6)$$

where

$$f(\varepsilon) = \frac{2}{\sqrt{\pi}} \left(\frac{\varepsilon}{(kT_e)^3} \right)^{\frac{1}{2}} \exp\left(-\frac{\varepsilon}{kT_e}\right) \quad (4.7)$$

4.2 Results and Discussion

Equations (4.5) and (4.6) were solved numerically in MATLAB based on experimentally measured n_e and corresponding modeled T_e for data obtained at 3 Torr at PRF=30 and 75 kHz in argon plasma with 450 ppm of water impurities. The resulting $\sigma(t)$ and $\varepsilon_r(t)$ (since $T_e(t)$) in the plasma afterglow are presented in figures 4.1 and 4.2, respectively, at three different radio frequencies of 30, 100, and 300 MHz. Each of these two figures also shows the corresponding decay of n_e and T_e . From figure 4.1, it is apparent that in the afterglow for both PRFs=30 kHz and 75 kHz, at all frequencies there is an initial rapid increase in conductivity after the pulse. At the pulse ends, the

rapid decrease in electron temperature due to the excitation of argon metastables causes a significant reduction of the electron-momentum collision frequency. Such a process occurs almost instantaneously ($<1 \mu\text{s}$) compared to the onset of electron recombination causing this apparent immediate increase in conductivity.

After this initial rise, further thermalization ultimately causes an order of magnitude increase in conductivity at $f=30 \text{ MHz}$ for both PRFs. At $f=100 \text{ MHz}$, σ initially increases and then remains relatively constant for the duration of the afterglow. However, at $f=300 \text{ MHz}$, after the conductivity experiences a small initial rise, it experiences a slow decay since now $\nu < \omega$ in the afterglow. The conductivities at PRF=75 kHz are higher than those at PRF=30 kHz due to the larger electron densities achieved. Moreover, the conductivity leveling off for all frequencies as seen at PRF=30 kHz occurs due to the electrons having completely thermalized (see the T_e plot) meaning the collision frequency ceases to change.

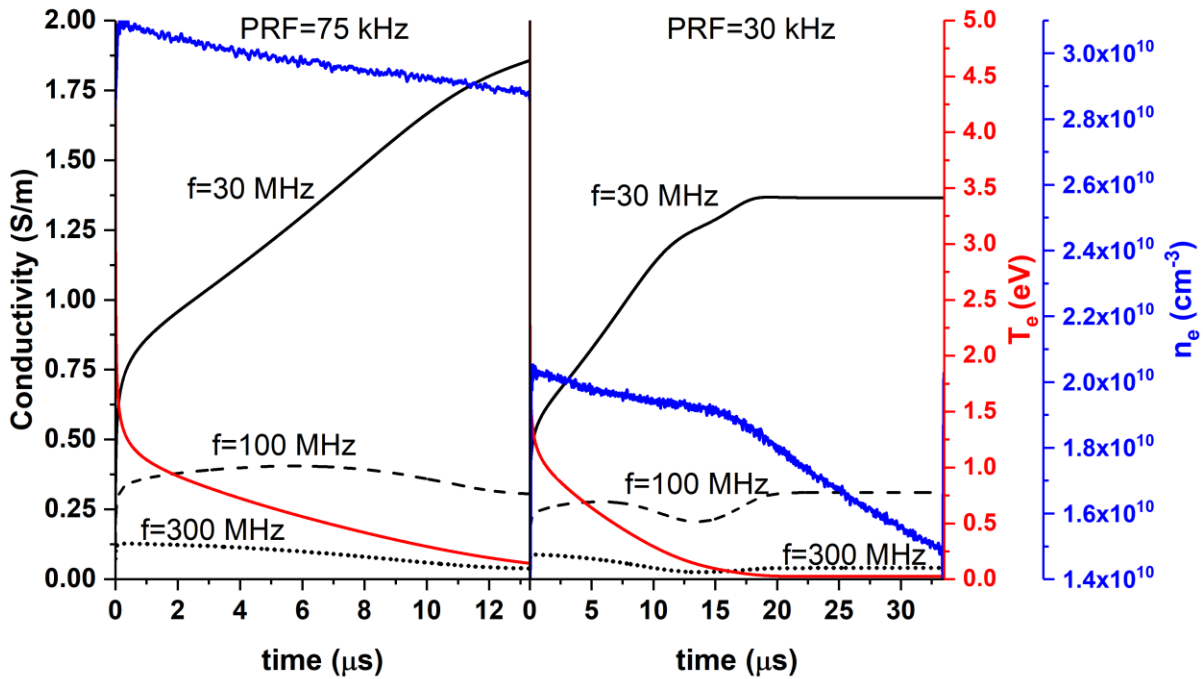


Figure 4.1. Conductivity for RF=30 MHz, 100 MHz, and 300 MHz in the afterglow of argon plasma. The experimentally measured n_e and corresponding modeled T_e correspond to plasma at 3 Torr argon with 450 ppm of H_2O .

From figure 4.2, it is apparent that in the afterglow for both PRFs=30 kHz and 75 kHz, at all frequencies there is also an initial rapid decrease in permittivity after the pulse for the same reason there was an increase in conductivity as previously explained. However, the initial fall in ϵ_r after the pulse is by two orders of magnitude, much more pronounced than in conductivity.

After this drop, further thermalization ultimately causes approximately another order of magnitude decrease in conductivity at $f=30$ MHz for both PRFs. Interestingly, for PRF=30 kHz, a minimum occurs at $\approx 13 \mu\text{s}$. This is due to the electron temperature being low enough that the Ramsauer-Townsend effect in argon is overcome and the collision frequency begins to increase again. At $f=100$ MHz and $f=300$ MHz, permittivity continues to decrease before remaining constant for the duration of the afterglow after thermalization occurs. The permittivities at PRF=75 kHz are lower than those at PRF=30 kHz due to the larger electron densities achieved.

Such results show that interesting operation regimes for plasma electronics may exist in the afterglow of a pulsed plasma, particularly at frequencies up to a couple hundred MHz for conductivity and perhaps up to a few GHz for permittivity. In the case of conductivity, such results may allow plasma electronics to be sustained with smaller power supplies without sacrificing performance. In the case of permittivity, a plasma device (such as an electrically short plasma antenna) may be better electrically matched by controlling at what time in the plasma afterglow and in what frequency range it operates.

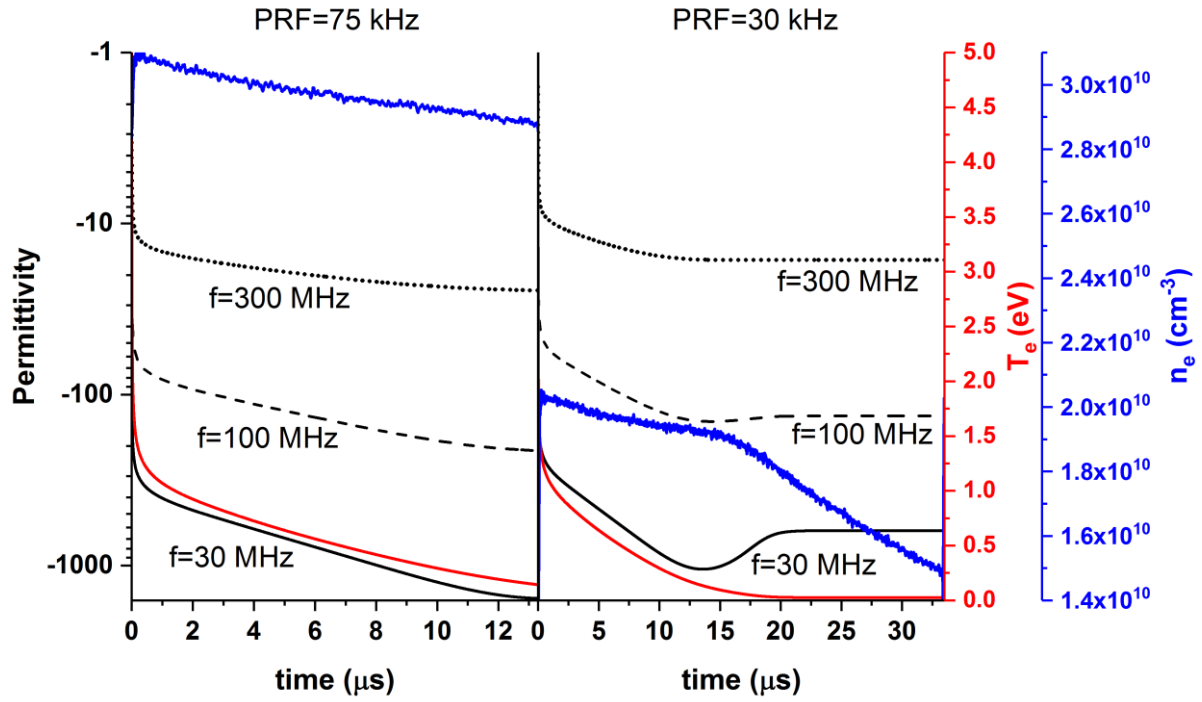


Figure 4.2. Permittivity for RF=30 MHz, 100 MHz, and 300 MHz in the afterglow of argon plasma. The experimentally measured n_e and corresponding modeled T_e correspond to plasma at 3 Torr argon with 450 ppm of H_2O .

5. COST OF IONIZATION

5.1 Introduction

In recent years, extensive research was performed on plasmas generated by high-voltage, nanosecond-duration, repetitive pulses for applications such as plasma-assisted combustion, aerodynamic flow control, and plasma electronics [50], [66], [80]–[82]. By varying the pulse parameters of the applied peak voltage and pulse repetition frequency, it is possible to manipulate the chemical species, excited states, and electron density in the plasma. A key benefit of utilizing these pulses for plasma generation is their low power budget, with the ionization cost per electron approaching the theoretical Stoletov's minimum [45], [83], [84].

The power budget per unit volume, P_B , of sustaining a discharge driven by high voltage, repetitive pulses is given by

$$P_B = Y_i \cdot \Delta n_e \cdot PRF \quad (5.1)$$

where Y_i is the ionization energy cost per electron, Δn_e is the number density of electrons created per pulse, and PRF is the pulse repetition frequency. Since the number density of electrons the discharge needs to sustain depends on the application, the PRF and ionization cost are the two parameters that can be experimentally controlled to reduce the power budget. All other parameters held constant, it is important to operate at a PRF that matches the overall loss rate of electrons (due to recombination, attachment, diffusion, etc.) in the pulse afterglow [45], [83], [84]. Doing so enables a regime in which a quasi-steady plasma is created as depicted in figure 5.1 and investigated in [66]. Since electron recombination, attachment, and diffusion rates are functions of gas pressure, the optimum PRF varies directly with pressure [83].

Even if the PRF is ideally chosen, the power budget can still vary by orders of magnitude depending on the energy cost of ionization, i.e. the mean energy required to produce a new electron

in the discharge. A theoretical analysis of ionization cost as it relates to the Townsend ionization and secondary emission coefficients as well as both the voltage drop across the cathode sheath and bulk plasma is presented in [45]. Using the Townsend ionization coefficients, it is easy to generate a curve of Y_i as a function of E/N [45], where E is the electric field strength and N is the number density of the gas. This relation is shown in figure 5.2 for both argon and air along with the corresponding theoretically minimum ionization cost at the Stoletov's point (41 eV for argon and 66 eV for air). For each gas, there is a well-defined E/N that corresponds to this minimum. If E/N deviates from this minimum by a factor of 10, the ionization cost increases by 2-3 orders of magnitude. Therefore, it is imperative to understand and operate in the proper ionization regime to minimize the ionization cost and the overall power budget.

Investigating the mechanisms which yield the lowest ionization costs is difficult due to the complex dynamics and kinetics of such plasma. Macheret et. al. modeled conditions at 10 Torr and compared them to experimental results in air [45]. They found that since most of the applied peak voltage falls across the cathode sheath, the E/N in this region is extremely high, much greater than that in the Stoletov's point, and the corresponding ionization cost is very large. In contrast, in the bulk plasma the electric field is much closer to Stoletov's point resulting in much more efficient ionization [45]. Such results are supported by the experimentally measured values of ionization costs of 55-150 eV at pressures of 1, 5, and 10 Torr. However, the experimental results produced were only for an applied peak voltage of 7 kV at a repetition rate of 100 kHz.

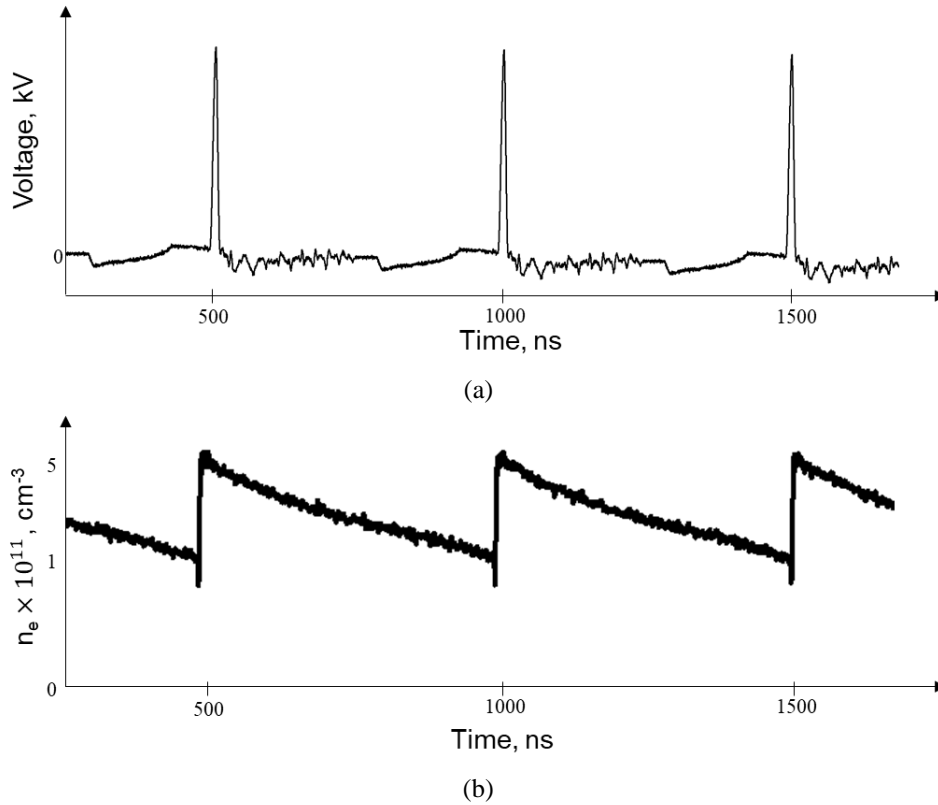


Figure 5.1. (a) Example of a high voltage, nanosecond pulse train applied at high PRF and (b) an illustration of the quasi-steady electron number density that it can sustain. n_e decay between the pulses is relatively small, less than by an order of magnitude.

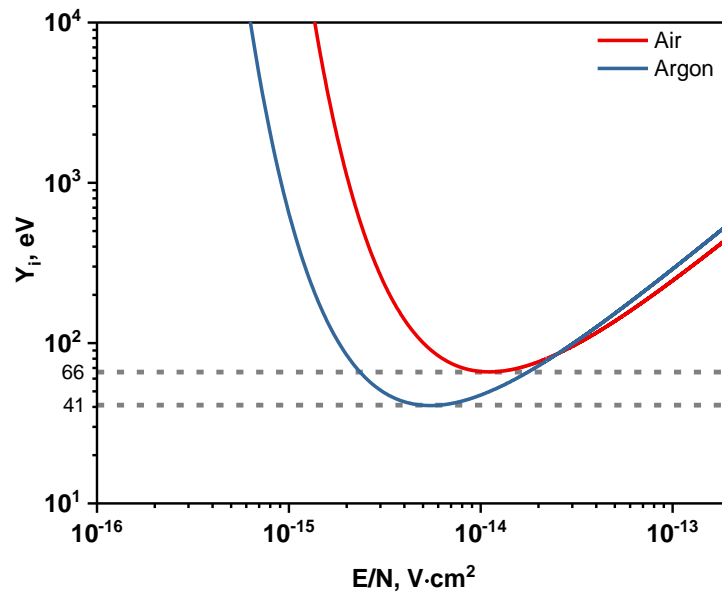


Figure 5.2. Theoretical cost of ionization, in eV per newly produced electron, for both argon and air as a function of applied E/N . The dashed line indicates each gas's Stoletov's point and corresponding cost.

The present experimental work expands on these previous results and aims to produce a more comprehensive dataset to serve as a baseline for future comparison with kinetic modeling. Our experiments were performed in argon and air at pressures of 2, 3, 5, and 10 Torr with applied voltages of 1.5 to 7 kV pulsed at repetition frequencies of 0.1, 3, 10, 20 and 30 kHz were used.

5.2 Experimental setup

Experiments were performed in the configuration shown in figure 5.3a. Plasma was sustained between two, parallel-plate, aluminum electrodes each having a diameter of 5 cm and each flush mounted into an acrylic plate. Three ceramic spacers were inserted into counter-bored holes on the acrylic to align the electrodes and set the spacing between them to 2 cm. The acrylic plates are clamped using all-thread through the spacers fastened with nuts on each end. The top acrylic plate also serves as the cap of the vacuum chamber: it has a groove into which a face seal fits allowing the assembly to rest on top of, and seal against, a Pyrex cylinder. The bottom of the Pyrex cylinder rests on another face seal.

An Edwards E2M-1 rotary vane vacuum pump was used to evacuate the chamber and an Alicat MC-200 was used to set the chamber pressure which was measured using an MKS Type 626C Baratron. In the argon experiments, an MKS e-Microvision PVD Residual Gas Analyzer (RGA) was used to monitor the chamber gas species since the chamber's face seals allows for impurities to enter. The RGA system was able to sample the gas composition at such pressures through a VAT-21124 dosing valve connected to a 36 in., KF16 flex hose attached to the chamber.

To generate the plasma, the central wire of the coaxial cable is directly connected to the top electrode and the shield wire to the bottom via the all-thread. It is used to transmit nanosecond pulses to ionize the gas and sustain the plasma inside. The FID, FPG 10-100MC2-10 nanosecond pulser can output positive pulses of up to 5 kV at pulse repetition frequencies of up to 100 kHz. In

this experiment, the commanded voltages were varied from 1.5 to 5 kV and used PRF of 0.1, 3, 10, 20 and 30 kHz. Due to load mismatch, the measured applied voltage could reach in excess of 7 kV. Because this configuration tended to create coronas around the electrodes, special care was taken to operate in the proper voltage and PRF regimes for a given gas and pressure in order to avoid creating them.

The 58.1 GHz (0.52 cm wavelength) microwave interferometer developed and described in [66] was used to measure the electron number density of the bulk plasma. A LeCroy 8254 M oscilloscope was used to acquire the interferometer signals. A difference here from [66] is that the antenna horns were placed touching the Pyrex cylinder without any lenses or apertures. This was done to achieve a much higher signal-to-noise ratio, which was important at larger applied voltages. A higher ratio reduces the measured phase error that otherwise occurs when stronger plasma occludes the microwave signal and causes it to approach the system zero-point. Because the antenna horns used have a narrow beamwidth over the length of the electrodes and an aperture size less than the gap spacing, any reflections from the electrodes themselves should be minimized. Using the electron number density produced per pulse, n_e , and assuming plasma volume equivalent to the 40.5 cm³ volume of the space between the electrodes, it is possible to determine $N_{j,e}$, the total number of electrons produced during the application of the j^{th} pulse. This methodology requires the assumption that the electron number density is uniform.

The amount of energy deposited was made utilizing two different techniques: 1) a back current shunt (BCS) and 2) a combination of a resistive divider, high voltage (HV) probe (4.7 k Ω , MS 260 Caddock resistor and a 50 Ω cable) and a fast current transformer (FCT) (Bergoz FCT-028-1.25-WB). This configuration is depicted in figure 5.3b. A LeCroy 8254 M and 735 ZI oscilloscope were used to acquire the BCS and probe signals, respectively. With the BCS, the

incoming and reflected pulses are easily distinguished and used to determine the voltage and current deposited into the plasma in a manner described in [51]. Since the voltage divider and fast current transformer are placed 3 cm from the load, reflections should have a minimal effect on their measured values by the HV and FCT probes. From the voltage and current, the energy deposited into the plasma could then be calculated.

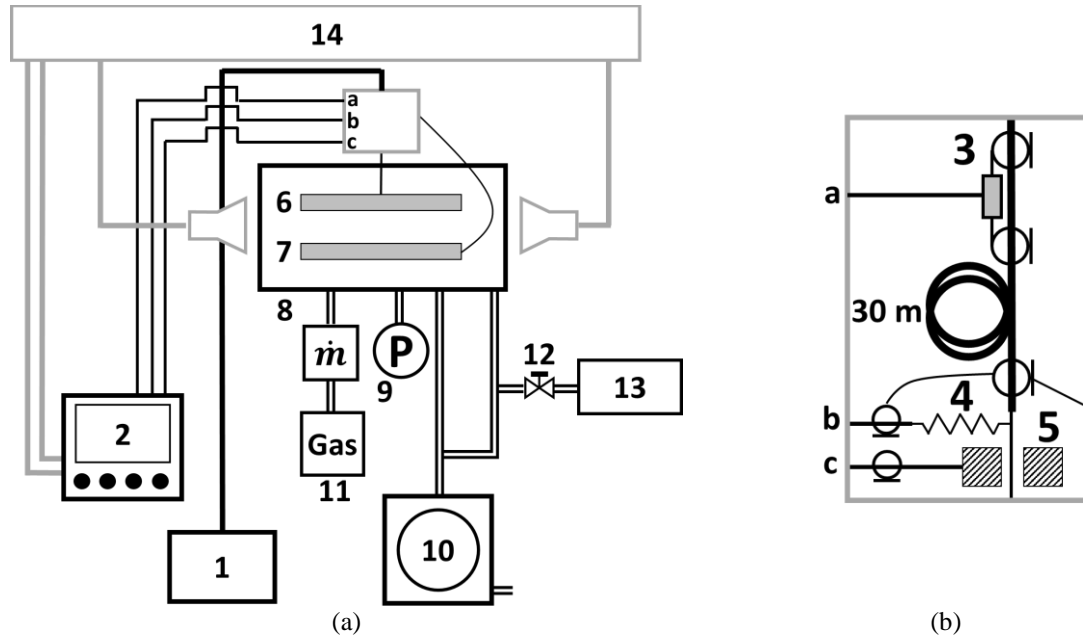


Figure 5.3. The experimental setup is in 3a while the voltage and current schematic is shown in 3b. The numbered components are as follows: (1) FID HV nanosecond pulser; (2) LeCroy 8254 M and 735 ZI oscilloscopes; (3) back current shunt; (4) resistive divider HV probe; (5) Bergoz FCT; (6) positive electrode; (7) electrode connected to shield; (8) mass flow controller; (9) 10 Torr Baratron; (10) rotary vane pump; (11) gas supply; (12) dosing valve; (13) RGA system; (14) microwave interferometry system.

To determine the energy deposited using the BCS, consider figure 5.4. Here, an incident pulse is first generated with energy ϵ_{1IN} and transmitted to the load, the electrodes with any discharge between them. Because the load is not matched to the transmission line, a portion of this incident energy is reflected, ϵ_{1B} , and transmitted back towards the pulser instead of being absorbed by the plasma. The design of this pulse generator is such that it cannot absorb the entirety of the reflected pulse: another reflection of energy occurs at the pulser, ϵ_{2IN} , and travels toward the

discharge cell. Again, whatever energy is not absorbed is reflected, ϵ_{2B} , and this process continues until the pulse energy decays towards 0 J.

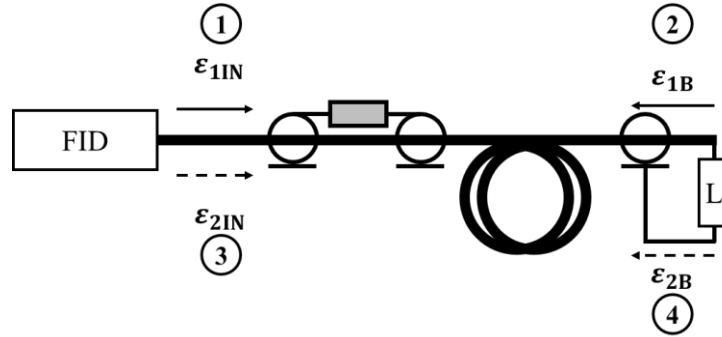


Figure 5.4. Energy and direction of pulse propagation.

Each time the wave passes the BCS, it can be measured and produces the raw signal as shown in figure 5.5. Through calibration of the raw signal to a known current source and known cable impedance (50Ω), the raw measurements can be converted into the actual voltage and current profiles:

$$I_{BCS} = \frac{BCS_{raw}}{0.146} \quad (5.2)$$

$$V_{BCS} = I_{BCS} \times 50\Omega \quad (5.3)$$

The cumulative energy, ϵ , can then be determined by equation (5.4) and is depicted in figure 5.6.

$$\epsilon = \int I \cdot V dt \quad (5.4)$$

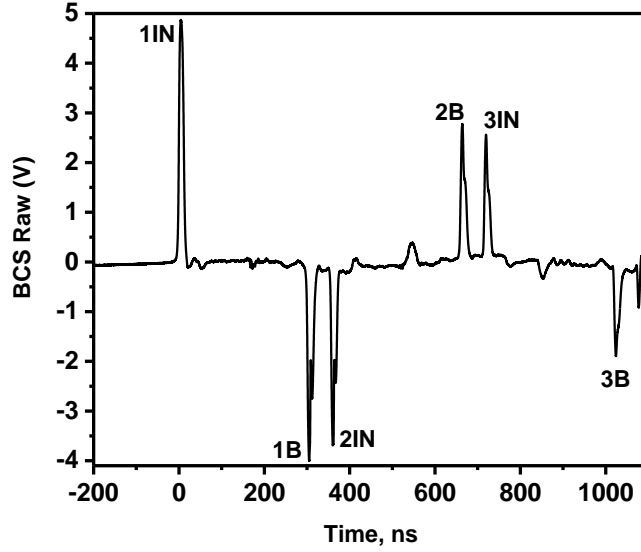


Figure 5.5. Raw BCS signal profile. Each peak labeled with IN refers to the incident pulse onto the discharge and with B refers to the reflected pulse from the discharge.

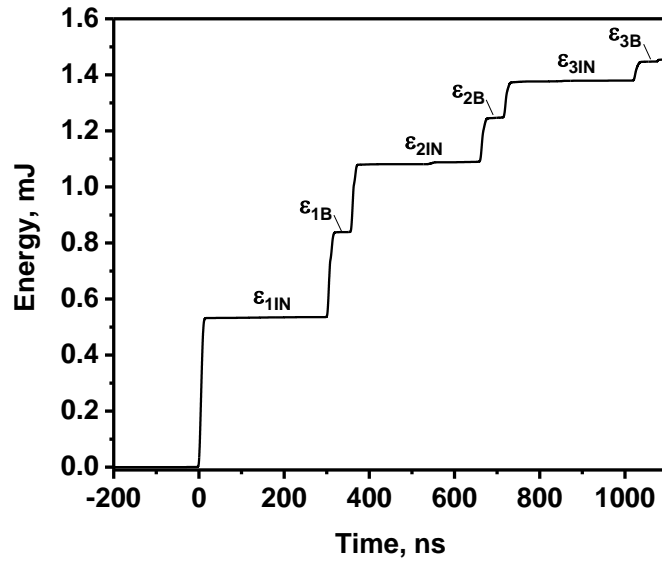


Figure 5.6. Cumulative energy extracted by the BCS technique.

Since equation (5.4) gives a cumulative energy, it is necessary to determine the total forward and reflected energies. The total forward energy of pulse j , $\epsilon_{j,F}$, can be determined by

$$\epsilon_{j,F} = (\epsilon_{j,IN} - \epsilon_{j-1,B})\alpha^2 \quad (5.5)$$

and the total reflected energy, $\epsilon_{j,R}$, by

$$\varepsilon_{j,R} = \frac{(\varepsilon_{j,B} - \varepsilon_{j,IN})}{\alpha^2} \quad (5.6)$$

where $\varepsilon_{j,IN}$ is the incident energy of the pulse traveling from the pulser, $\varepsilon_{j-1,B}$ is the reflected energy of the previous pulse from the discharge cell, $\varepsilon_{j,B}$ is the reflected energy of the current pulse from the discharge cell, and α is the one-way attenuation of the transmission line. α is determined by comparing the magnitudes of the incident and reflected pulses onto the discharge cell with no plasma present (i.e. an open load). For these experiments, it was determined to be 0.926. Once $\varepsilon_{i,F}$ and $\varepsilon_{i,R}$ are calculated, the energy deposited, $\varepsilon_{j,dep}$, can be determined

$$\varepsilon_{j,dep} = \varepsilon_{j,F} - \varepsilon_{j,R} \quad (5.7)$$

In our analysis of ionization cost, we focus on the energy deposited by the first two pulses ($j=1$ and $j=2$) as that comprises more than 95% of the total energy absorbed.

A similar procedure is done with the voltage and current probes to determine the energy absorbed. In this case, time-resolved voltages and currents are each directly measured by the HV resistive divider and FCT, respectively. Since these probes are close to the plasma cell, it is assumed that any reflections or signal attenuation is negligible, and that the measured signals are the deposited voltage and currents. Therefore, equation (5.4) can be used to determine the cumulative energy and then equation (5.5) can be used to find the deposited energies per each pulse since no reflections need to be accounted for like in the case of the BCS.

Having experimentally measured the deposited energy with two different techniques, the mean value, $\overline{\varepsilon_{j,dep}}$, was used with the measured $N_{j,e}$ to calculate the ionization cost per applied pulse

$$Y_{i,j} = \frac{\overline{\varepsilon_{j,dep}}}{N_{j,e}} \quad (5.8)$$

It is then also possible to determine the total cost of ionization for all pulses considered using the total energy deposited and total number of electrons created:

$$Y_{i,tot} = \frac{\sum \overline{\varepsilon_{j,dep}}}{\sum N_{j,e}} = \frac{\overline{\varepsilon_{tot}}}{N_{e,tot}} \quad (5.9)$$

5.2.1 Determining Uncertainty

The standard deviation of the deposited energy measured using these two techniques gives the uncertainty in energy deposited per pulse, $\delta\varepsilon_{j,dep}$. The uncertainty in the electrons produced per pulse, $\delta N_{j,e}$, was found to be within 20%. The uncertainty in ionization cost per pulse, $\delta Y_{i,j}$, was found through error propagation

$$\delta Y_{i,j} = Y_{i,j} \sqrt{\left(\frac{\delta \overline{\varepsilon_{j,dep}}}{\overline{\varepsilon_{j,dep}}}\right)^2 + \left(\frac{\delta N_{j,e}}{N_{j,e}}\right)^2} \quad (5.10)$$

The uncertainty of the mean total deposited energy, $\delta \overline{\varepsilon_{tot}}$, and of the total number of electrons produced, $\delta N_{e,tot}$, can be found, respectively, through error propagation of their uncertainties per pulse

$$\delta \overline{\varepsilon_{tot}} = \sqrt{\sum \delta \overline{\varepsilon_{j,dep}}^2} \quad (5.11)$$

$$\delta N_{e,tot} = \sqrt{\sum \delta N_{j,e}^2} \quad (5.12)$$

Finally, the uncertainty of the total cost of ionization, $\delta Y_{i,tot}$, is found through error propagation using the values given by equations (5.11) and (5.12).

$$\delta Y_{i,tot} = Y_{i,tot} \sqrt{\left(\frac{\delta \overline{\varepsilon_{tot}}}{\overline{\varepsilon_{tot}}}\right)^2 + \left(\frac{\delta N_{e,tot}}{N_{e,tot}}\right)^2} \quad (5.13)$$

5.3 Results and Discussion

5.3.1 RGA Analysis

The measured concentration of species present during experiments in argon are shown in figure 5.7. As expected, the purity of the argon gas in the chamber improves with increasing working pressure. In our previous work, we demonstrated that recombination processes in the afterglow of an argon plasma are significantly affected in the presence of impurities [85]. The narrative is different during the actual creation of a plasma by the nanosecond pulse. It was assumed that the scarce presence of N_2 , O_2 , and H_2O means that mostly Ar will be ionized. Therefore, it is sufficient to assume Stoletov's point should still correspond to that of argon rather than some gas mixture.

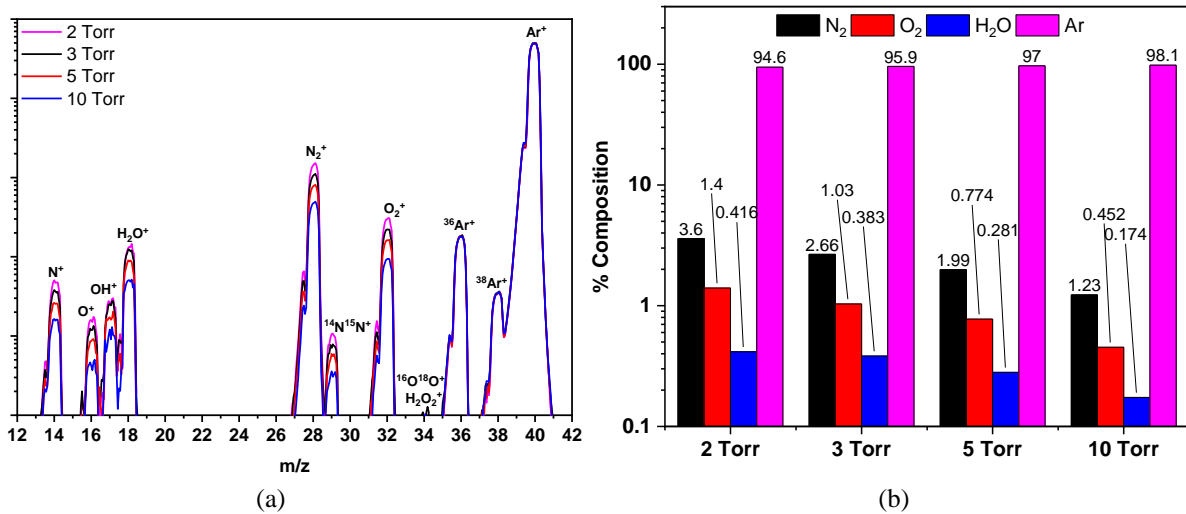


Figure 5.7. (a) The specific species detected by the RGA at pressures of 2, 3, 5, and 10 Torr. (b) the percent composition of the most dominant gases found during experiments in argon at the pressure tested.

5.3.2 Voltage and Current Measurements

An example of the incident and reflected waves used to reconstruct the BCS measured applied voltage and current profile of the first pulse is shown in figure 5.8 to describe the effects of pressure and repetition frequency on pulse shape. It is evident that as the wave travels from the pulser toward the plasma (1IN in figure 5.4), the peak voltage generated by the pulser is within 2-5%

regardless of the plasma conditions. However, as this wave gets reflected and travels from the plasma (1B in figure 5.5), this is no longer the case. The reflected pulse shape becomes distorted and appears to widen with decreasing pressure as seen in figure 5.8a. Such an effect is more noticeable when PRF is increased. Indeed, in figure 5.8b, the magnitude of 1B drops to $\sim 1/4$ its peak value as pulse repetition frequency is increased. This suggests that most of the energy is delivered to the load and that the plasma's impedance becomes better matched with increasing repetition frequency. Evidence of this behavior is further emphasized in figure 5.9 by noting that the peak voltage of the applied pulse approaches to within 10% of the 2.5 kV commanded on the pulser as *PRF* is increased while the same effect is not as pronounced with pressure variation.

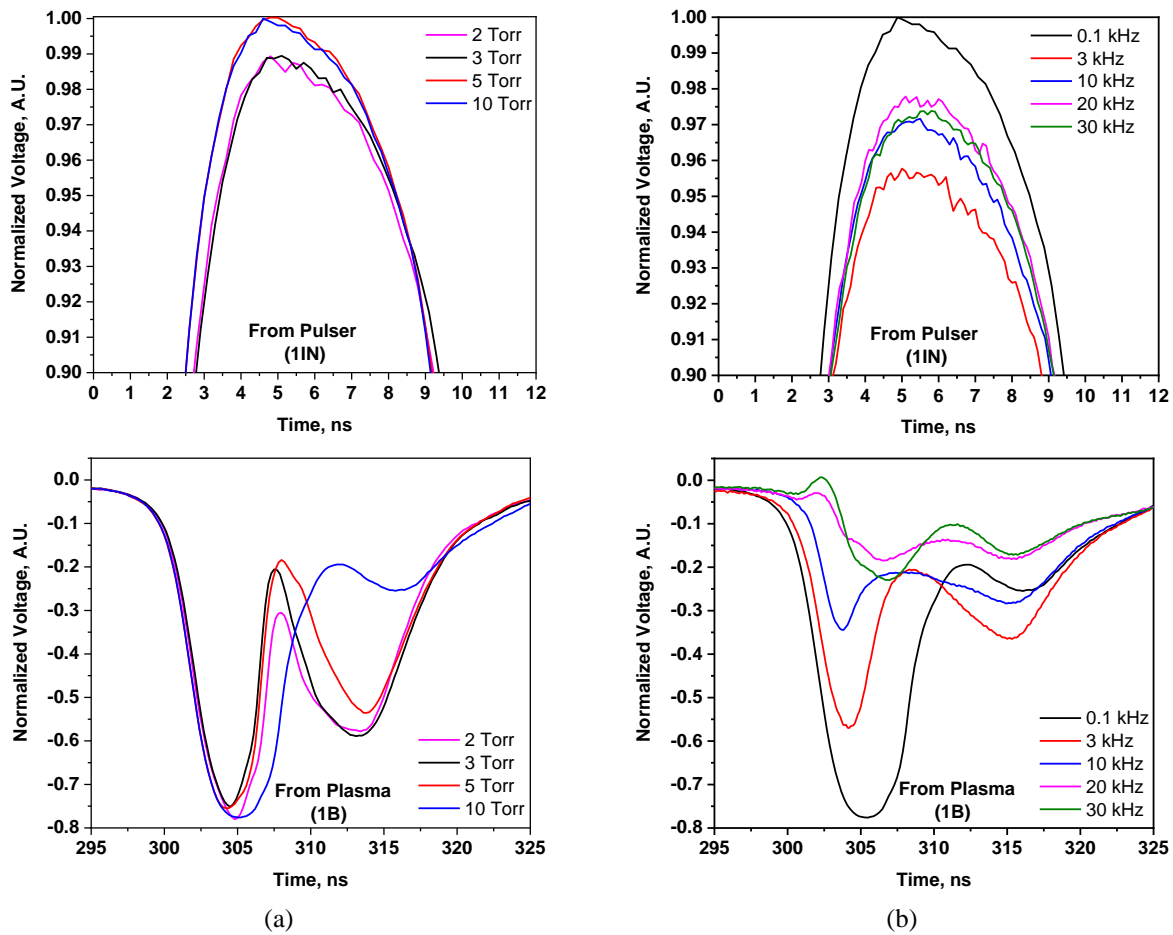


Figure 5.8. BCS measurement of pulse traveling to and from the plasma for a commanded voltage of 2.5 kV. The profiles have been normalized by the peak measured voltage. (a) Argon, 0.1 kHz, pressure varied (b) Argon, 10 Torr, *PRF* varied.

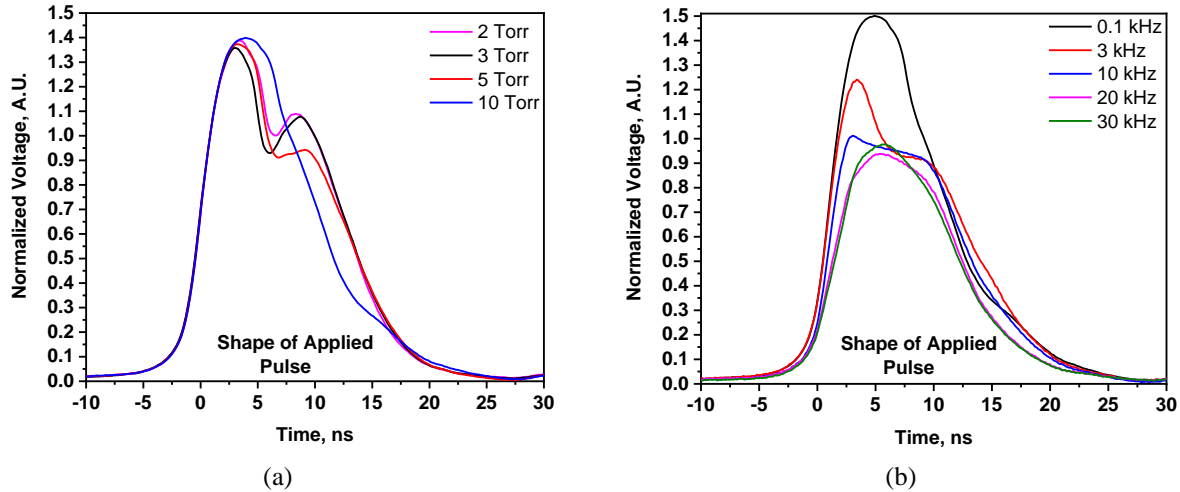


Figure 5.9. Pulse voltage profiles applied to the plasma, reconstructed from the BCS measurements of figure 8. The profiles have been normalized by the commanded voltage of 2.5 kV. (a) Argon, 0.1 kHz, pressure varied (b) Argon, 10 Torr, *PRF* varied.

The reconstructed applied voltage and current profiles used to sustain an air plasma at varying pressures with repetition frequency of 0.1 kHz are shown in figure 5.10. The trends described for this figure are also observed in argon (Appendix B). As the commanded voltage is increased, noticeable changes in the pulse shapes are observed. When 2.0 kV is commanded, it is clear from figure 5.10a that the measured voltage profile at 5 and 10 Torr appears Gaussian in shape while a kink is present at 2 and 3 Torr at $t=7$ ns. The almost symmetric current profile at 10 Torr indicates that it is mainly the displacement current measured under this condition which suggests the load is a predominantly capacitive, open circuit with no plasma. Indeed, no plasma was measured by the microwave interferometer when 2.0 kV is applied to 10 Torr.

When the commanded voltage is increased to 2.5 kV (figure 5.10b) the magnitude of applied voltage and current is increased. The current profile at 10 Torr starts to increase at $t=6$ ns while the voltage profile begins to narrow. Figures 5.10c-5.10f show that as the commanded voltage is increased, this behavior continues with a reduction in voltage after the first peak becoming more pronounced. Increasing voltage causes more electrons and an overall stronger

plasma to be generated. More electrons cause a decrease in plasma resistance which allows for more conductive current to flow as seen by the increasing secondary peak relative to the first in the current profiles taken at 10 Torr. Such an effect is also observed at the other pressures to a less pronounced effect. In the voltage profiles, the decrease in magnitude after the initial peak corresponds to the maximum secondary peak in current indicating that plasma breakdown occurs at this moment. The time of breakdown shifts from $t = \sim 7$ ns to $t = \sim 4$ ns with increasing applied voltage as a stronger electric field is produced sooner enabling the breakdown to proceed faster.

A representative sample comparing the applied voltage and current profiles of the first and second pulse (due to reflection from the pulse generator) is shown in figure 5.11. For all pressures tested, the polarity of the second pulse's voltage profile is opposite to that of the first due to how this FID pulser's circuitry absorbs and reflects the pulse coming back from the load. At 2, 3 and 5 Torr, the shape of the second pulse's current profile is more sinusoidal than that of the first pulse. Unlike when the first pulse is applied to the electrodes, there exists a plasma when the second pulse arrives; therefore, the load (plasma) impedance now has both resistive and reactive parts and perhaps behaves as an RLC circuit. Moreover, while still high, the magnitude of the applied voltage and current of the second pulse is less than that of the first pulse. This suggests that the amount of energy deposited by the second pulse would be less than the first but still high enough to produce electrons within 1-2 orders of magnitude of what is generated by the first pulse.

An analysis of figures 5.10 and 5.11 shows that the resistive and strong reactive components of the plasma sustained in this parallel-plate configuration both vary in time. This makes it difficult to determine the plasma impedance by simply using Ohm's law with the acquired voltage and current profiles. Instead, the experimental results should be coupled with simulations to estimate the plasma impedance.

Figures 5.9-5.11 demonstrates the difficulty of fixing the voltage applied to a plasma while varying pressure and pulse repetition frequency. Therefore, it is convenient to consider the dependence of plasma parameters as a function of the ratio between peak voltage of the first pulse and pressure, V_{peak}/P , rather than only V_{peak} . Note that the V_{peak} values presented in subsequent sections is an average of the maximum voltage measured by the BCS and HV probe since the same profile shape is captured but with differing magnitudes.

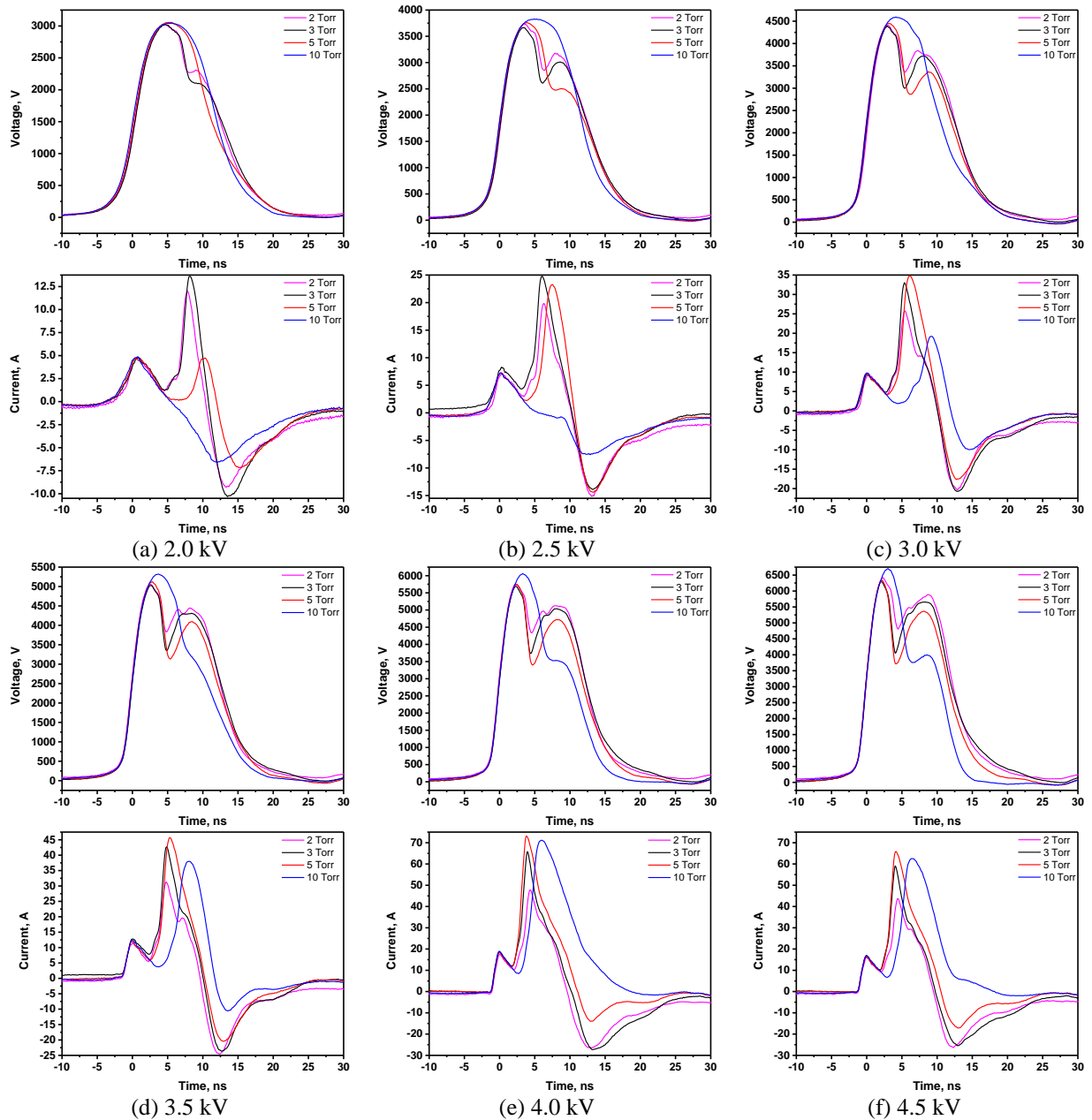


Figure 5.10. BCS Reconstructed applied voltage and current profiles for indicated commanded voltage pulsed at a repetition frequency of 0.1 kHz onto air plasma at the indicated pressures.

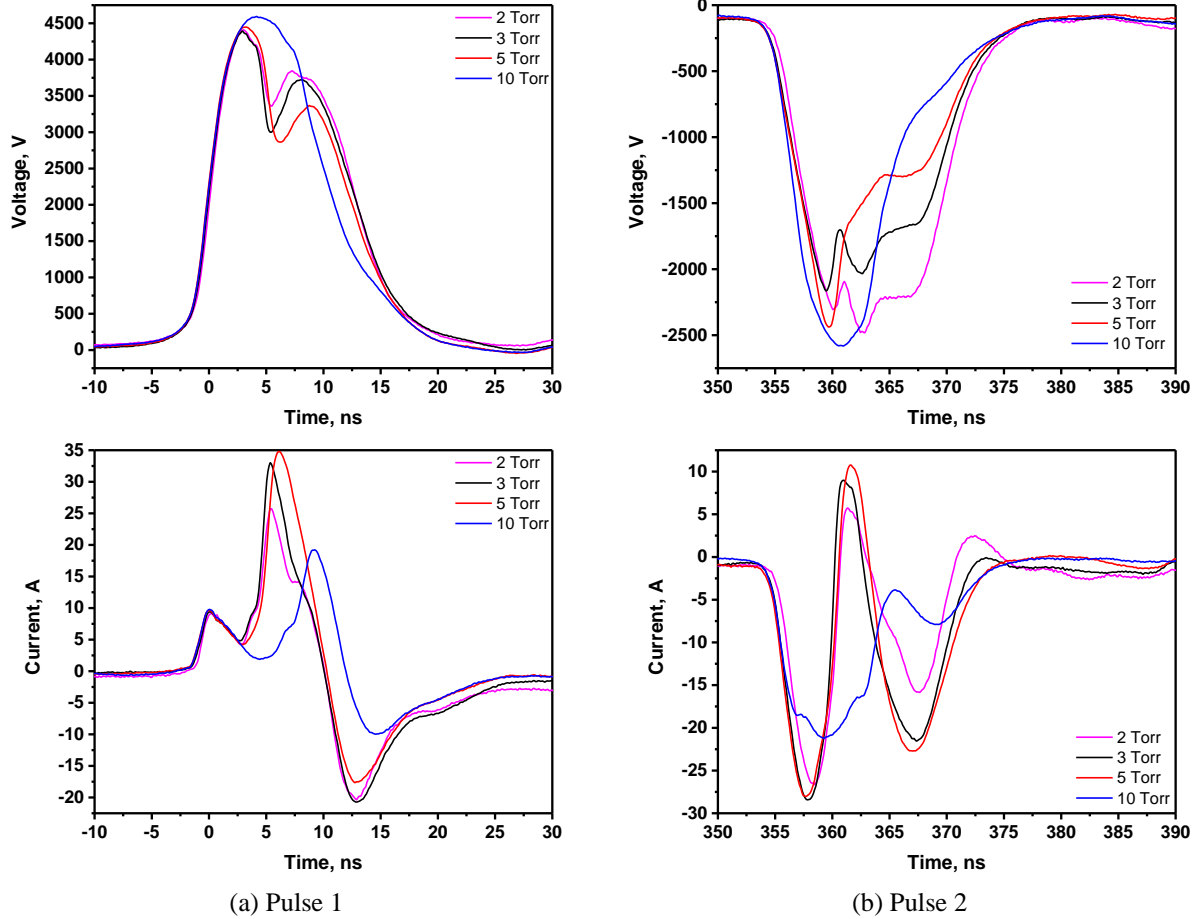


Figure 5.11. BCS reconstructed applied voltage and current profiles of the (a) 1st and (b) 2nd pulse for a commanded voltage of 3 kV at a repetition frequency of 0.1 kHz onto air plasma at the indicated pressures.

5.3.3 Energy Deposited and Measured Change in Electron Density

The average energy deposited into air and argon plasma by the first and second pulses are shown in figures 5.12 and 5.13, respectively. At constant V_{peak}/P , the energy deposited per pulse increases with pressure. For both gases at constant pressures, the deposited energy for each pulse increases with voltage, with the first pulse applying more energy than the second. The exception is at 0.1 and 3 kHz pulse repetition frequency. In air at 2 Torr and PRF of 0.1 kHz (figure 5.12a) the energy deposited by the first and second pulse is almost identical regardless of voltage. In air at 5 and 10 Torr (figure 5.12a-5.12b) and argon at 10 Torr (figure 5.13a-5.13b), this same behavior is observed, particularly at the lower end of applied voltages. This behavior can occur if the afterglow of the

plasma generated by the first pulse creates the conditions to provide a better impedance match. As the second pulse arrives, less energy is reflected compared to when the first pulse arrives at the load.

It is observed that the difference between the energy deposited by the first and second pulse for a given V_{peak}/P increases with pulse repetition frequency in both gases. At higher repetition frequencies, the electrons have less time to recombine; therefore, the overall quasi-steady electron number density is higher for higher repetition frequencies. This means that it is easier for the first pulse to transfer more of its energy to the plasma and generate a more conductive medium. Thus, when the second pulse arrives in the afterglow of the plasma created by the first, the plasma impedance could be similar to what it was at lower repetition frequencies and a similar amount of energy is transferred. In this manner, the energy deposited by the first pulse increases while the energy deposited by the second pulse is relatively constant causing the difference in energy deposited to increase.

The total energy deposited is shown in figure 5.14 for both argon and air. It is clear that the total energy deposited increases with pressure and voltage. At 0.1 kHz, the amount of energy deposited is similar for both gases at all pressures, while at 3, 10, and 20 kHz, more energy is deposited into argon than into air. In both gases, as pressure is increased, the slope of the total applied energy also increases with little dependence on PRF.

The Δn_e generated in air and argon plasma by the first and second pulses are shown in figures 5.15 and 5.16, respectively, while the total Δn_e is displayed in figure 5.17. Comparing figures 5.12 and 5.13 to figures 5.15 and 5.16, and figure 5.14 to figure 5.17, the electron number density exhibits the same trends observed in the energy deposited figures. This is to be expected since the number of electrons produced are coupled to the magnitude of energy supplied to the

electrodes. From figure 5.17, it is evident that in both air and argon plasmas that $10^{11} - 7 \times 10^{12} \text{ cm}^{-3}$ electrons are created under the conditions tested.

Figure 5.18 shows the total change in electron number densities at constant pressures in air (figure 5.18a-5.18c) and argon (figure 5.18d-5.18e) plasmas while varying the pulse repetition frequency. At 5 and 10 Torr, the total electron density increases with repetition frequency; however, the difference between Δn_e at 10, 20, and 30 kHz is not significant. Beyond a certain repetition frequency, the quasi-steady electron density ceases to change significantly due to a shorter time to decay between pulses. Therefore, beyond this limit, increasing *PRF* will not drastically change the number of electrons produced by each pulse. Since electron recombination rates in the plasma afterglow tend to increase with pressure, so should this limit. This may explain why a lack of variation is observed at 3 Torr in figure 5.18a and 5.18d.

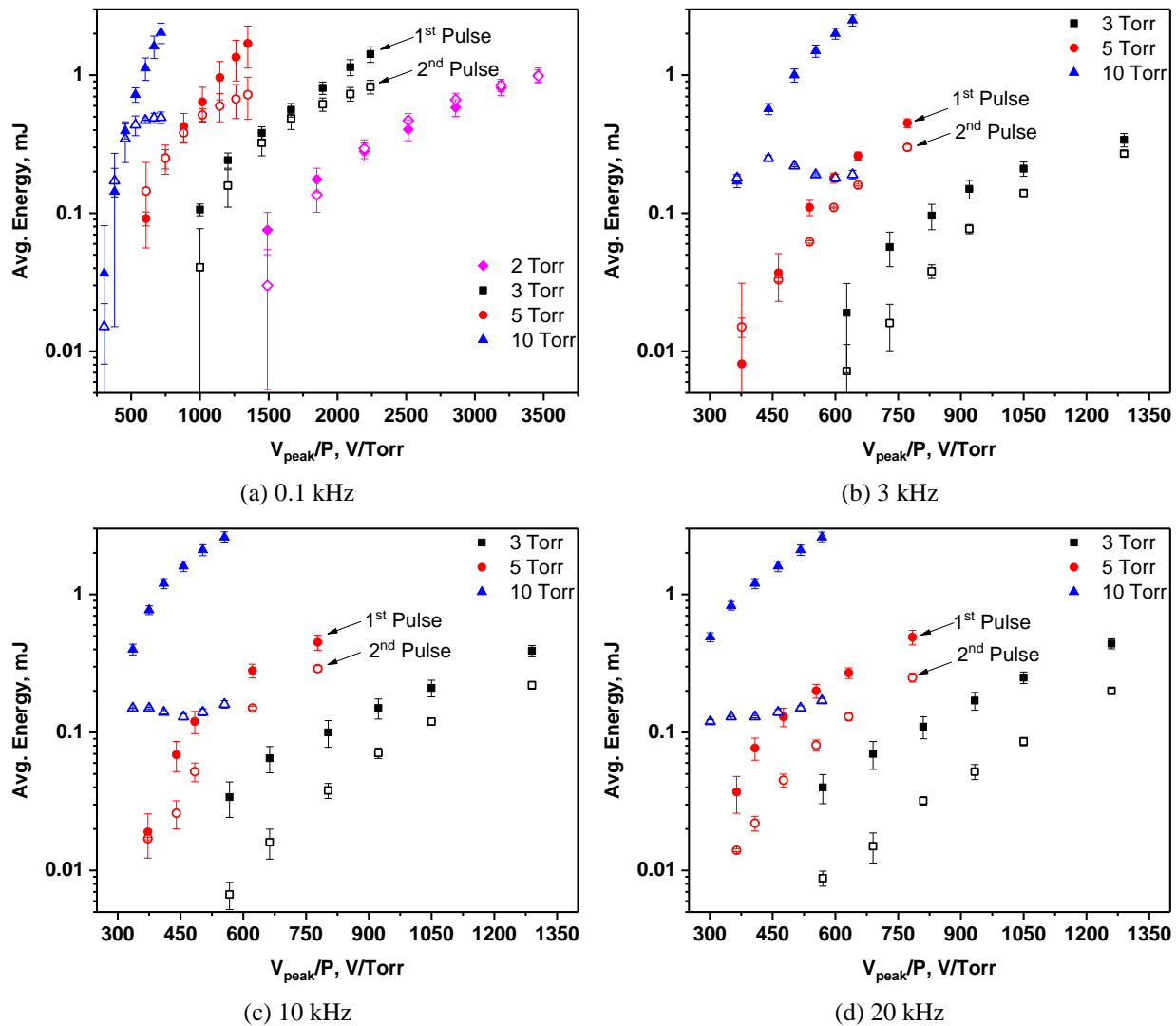


Figure 5.12. Energy deposited by the first and second pulse into air plasma at pressures of 2, 3, 5 and 10 Torr and repetition frequencies of 0.1, 3, 10, and 20 kHz. Data could only be acquired at 2 Torr at PRF=0.1 kHz without a corona forming.

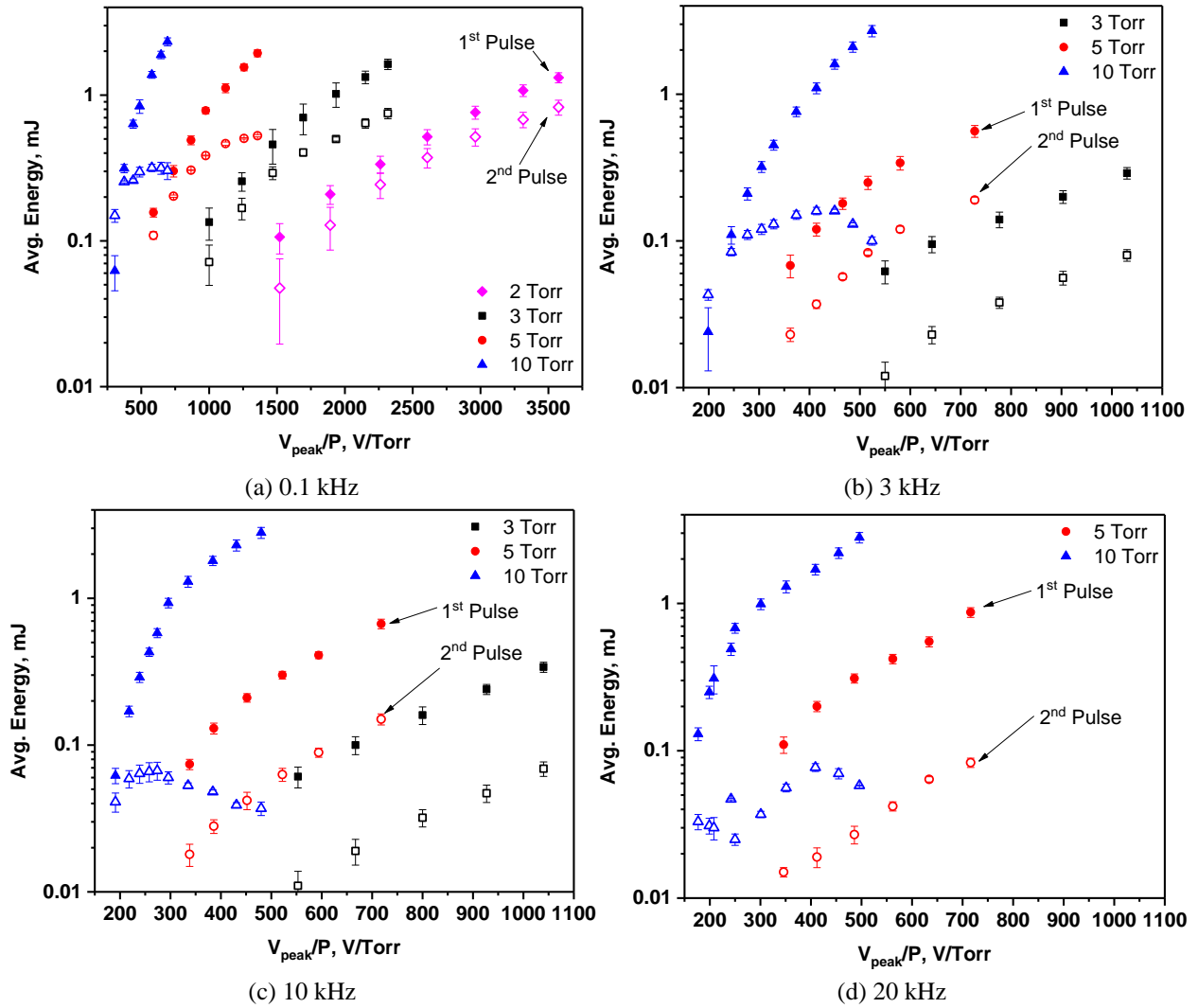


Figure 5.13. Energy deposited by the first and second pulse into argon plasma at pressures of 2, 3, 5 and 10 Torr and repetition frequencies of 0.1, 3, 10, and 20 kHz. Data could only be acquired at 2 Torr at PRF=0.1 kHz without a corona forming. Data was not collected at 3 Torr in figure 5.13d for the same reason.

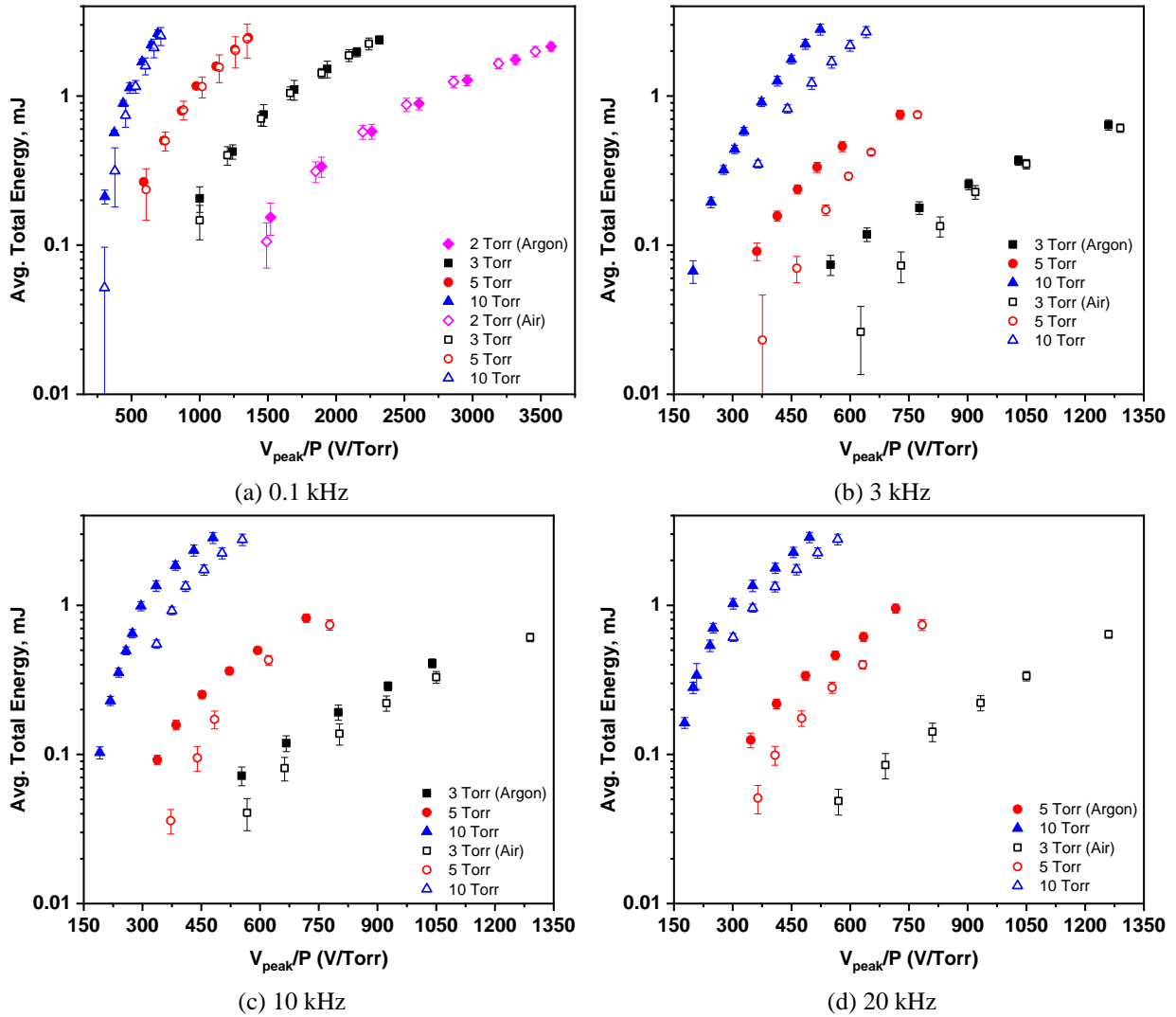


Figure 5.14. Total energy deposited onto argon and air plasma at the indicated conditions. Data could only be acquired at 2 Torr at PRF=0.1 kHz without a corona forming. Data was not collected at 3 Torr in figure 5.14d for the same reason.

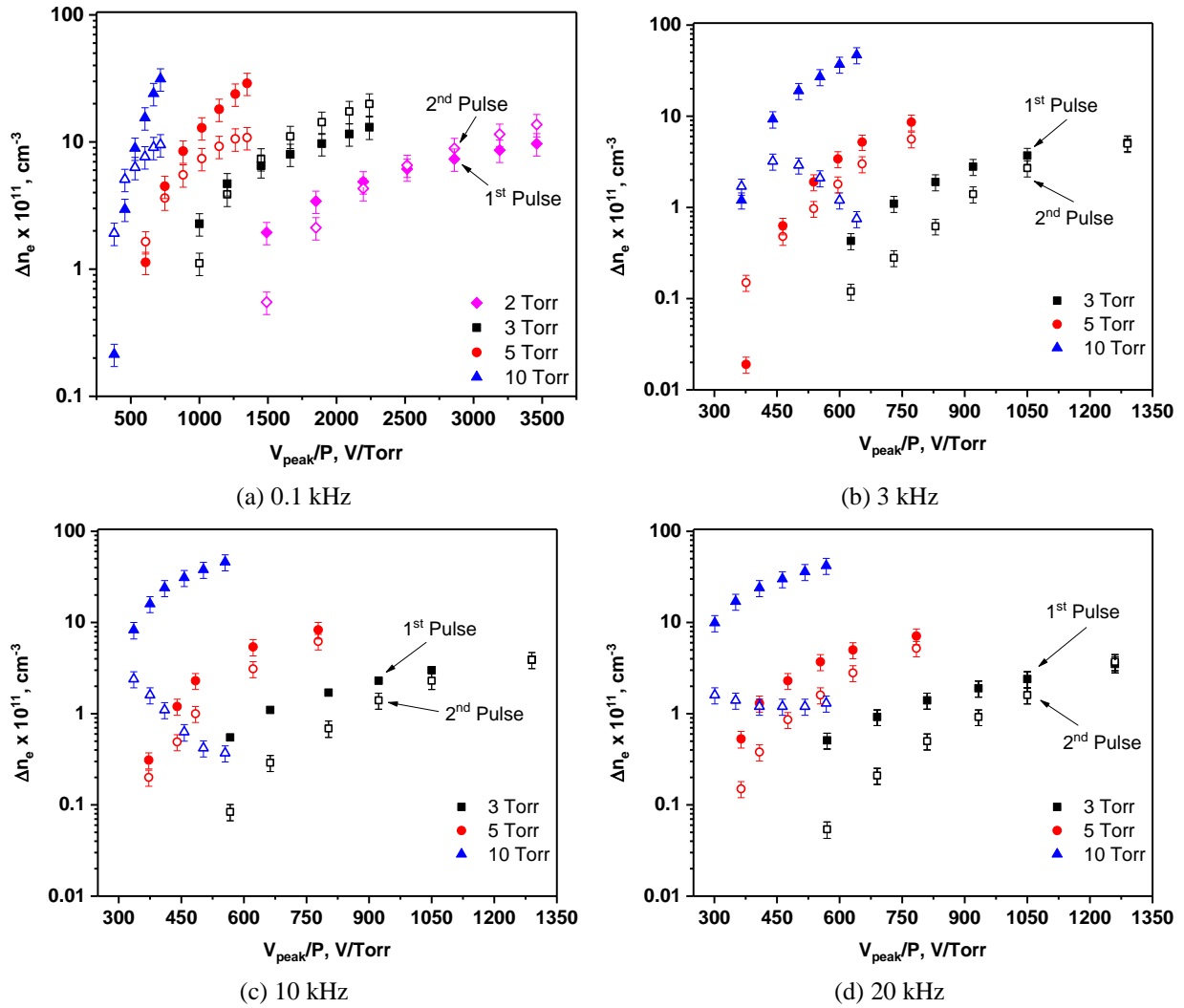


Figure 5.15. Measured change in electron density by each applied pulse at indicated repetition frequencies and pressures in air plasma.

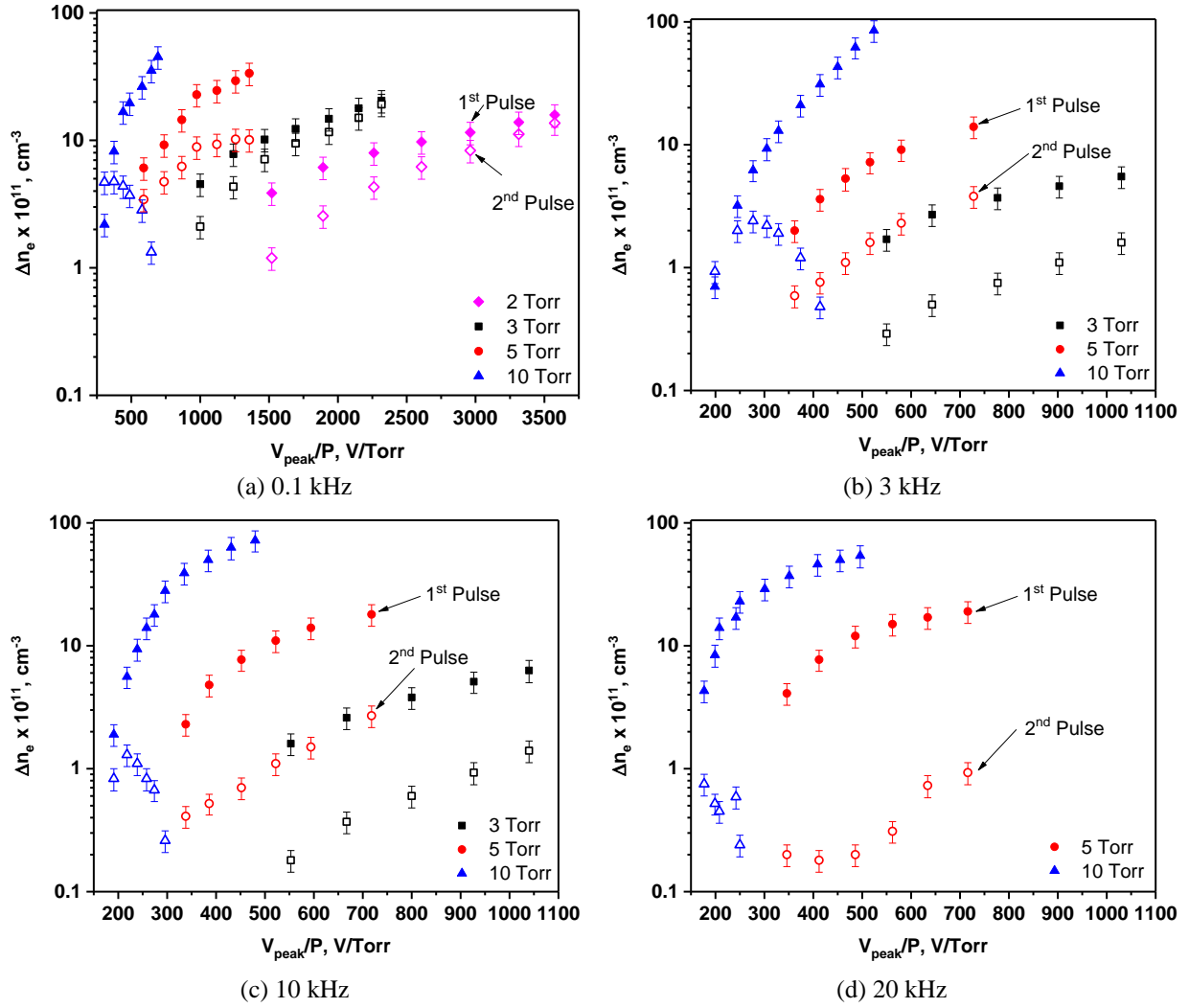


Figure 5.16. Measured change in electron density by each applied pulse at indicated repetition frequencies and pressures in argon plasma.

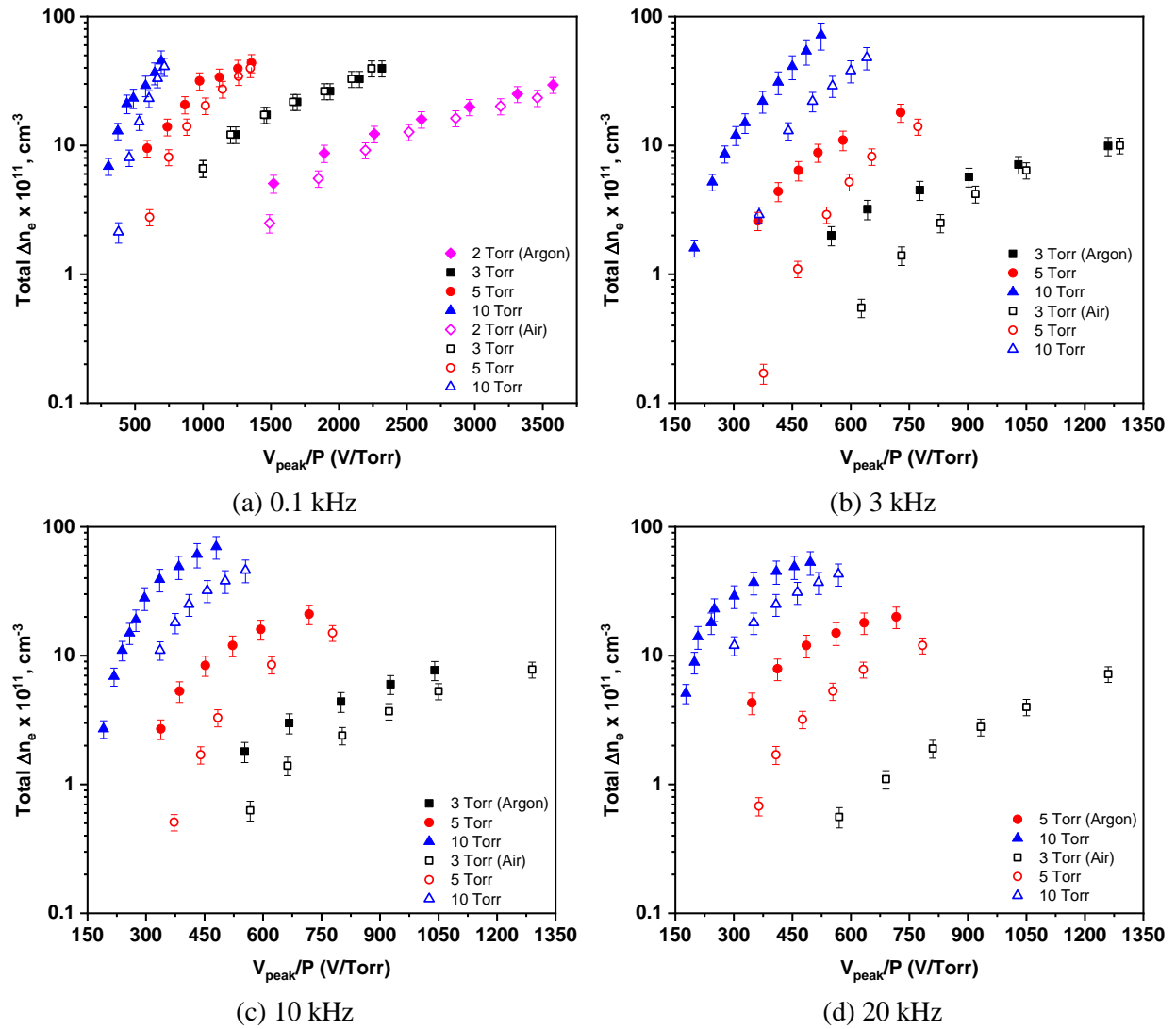


Figure 5.17. Total electron number density produced by each pulse at indicated pressures and repetition frequencies for argon and air plasmas.

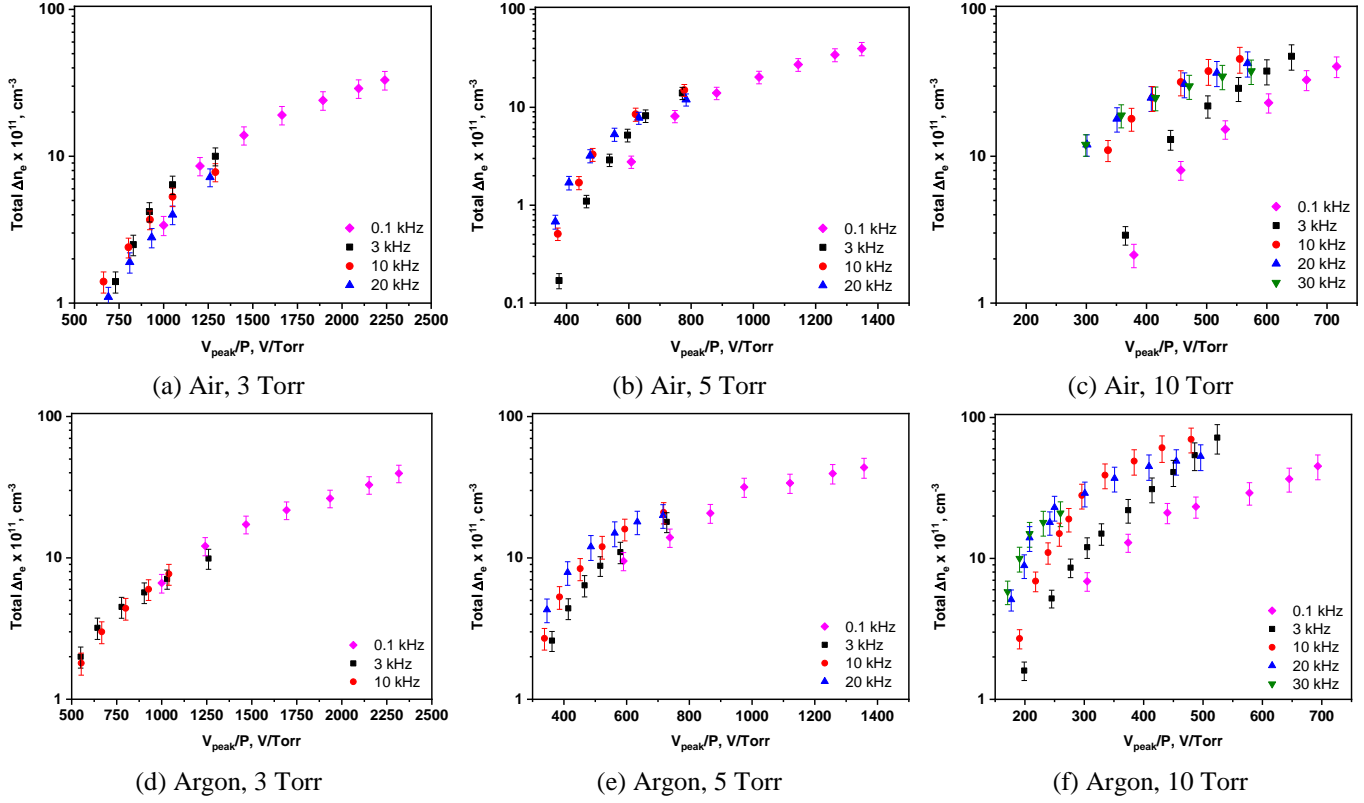
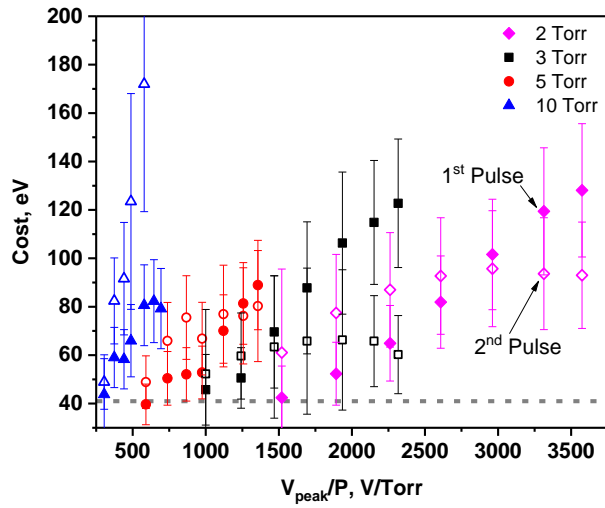


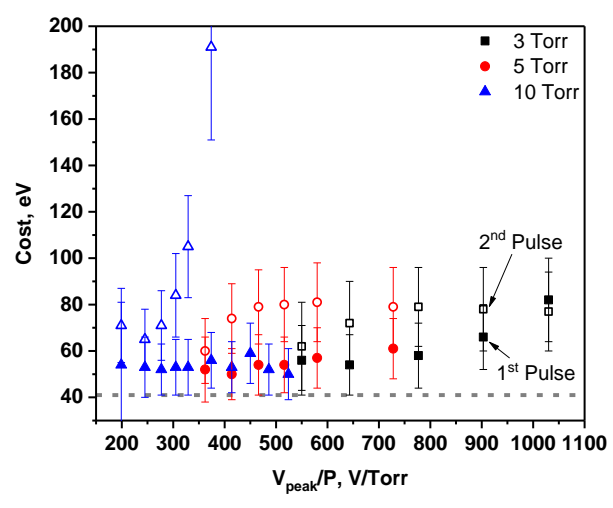
Figure 5.18. Effect of varying pulse repetition frequency at constant pressure in air and argon plasma on electron number density.

5.3.4 Cost of Ionization

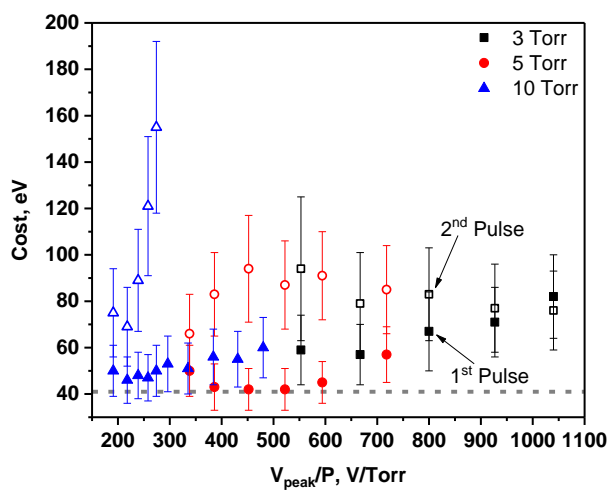
The calculated ionization cost of electrons created by the first and second pulse in argon and air plasma is shown in figures 5.19 and 5.20, respectively. In argon, the cost of ionization by the second pulse is higher than that of the first at most of the voltages and pressures considered for each *PRF* tested. However, due to the small fraction of energy deposited and electrons produced, the total calculated cost is generally closer to the cost of ionization by the first pulse. In air, the total cost of ionization is more influenced by the second pulse at higher voltages at all *PRF* and pressures tested, as seen in figure 5.21. This effect is more pronounced at 3 Torr at all *PRF* and 2 Torr at 0.1 kHz (figure 5.21a). At 10 Torr with *PRF* = 0.1 and 3 kHz (figure 5.21a and 5.21b), total cost tends to be closer to the second pulse at lower voltages.



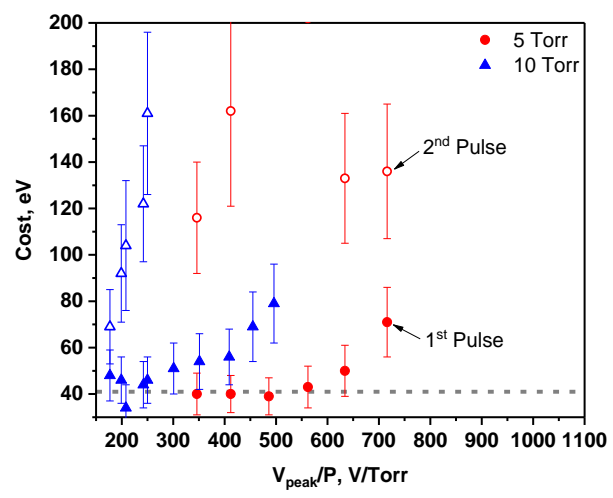
(a) Argon, 0.1 kHz



(b) Argon, 3 kHz



(c) Argon, 10 kHz



(d) Argon, 20 kHz

Figure 5.19. Cost of ionization for the first and second applied pulse in argon plasma. The dashed line is the cost associated with Stoletov's point.

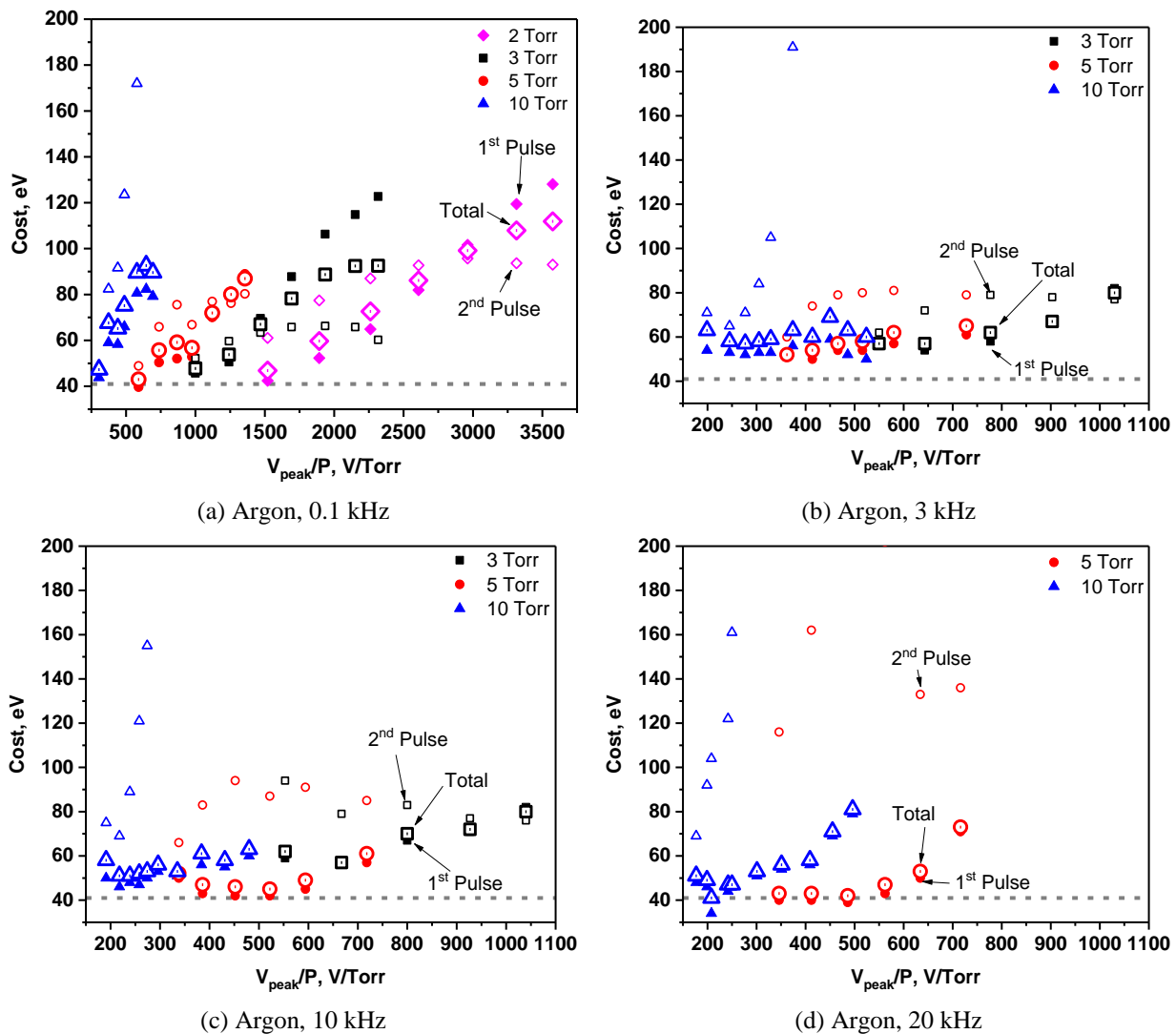
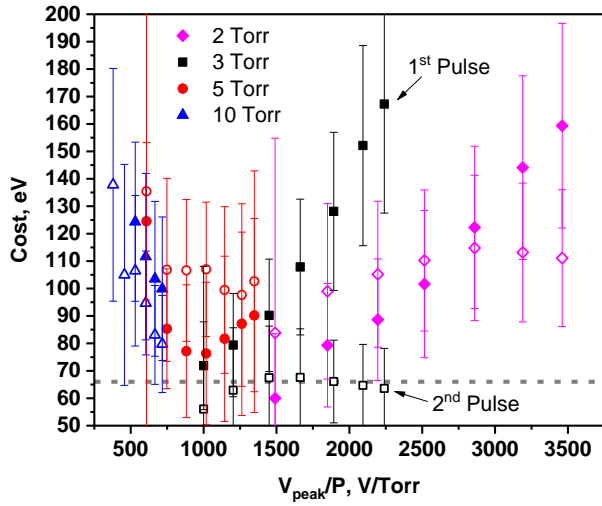
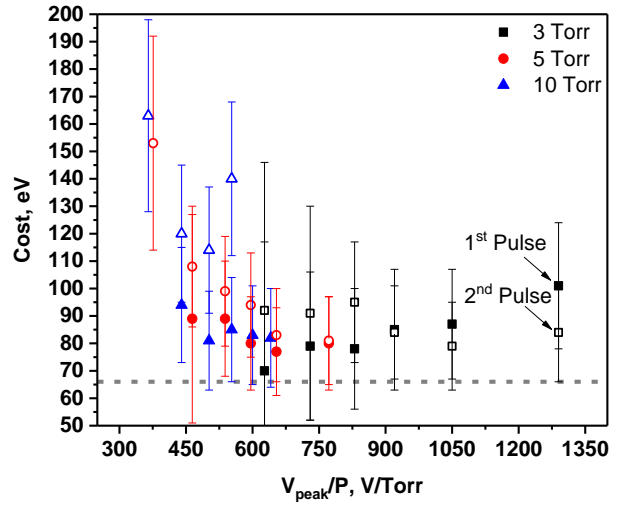


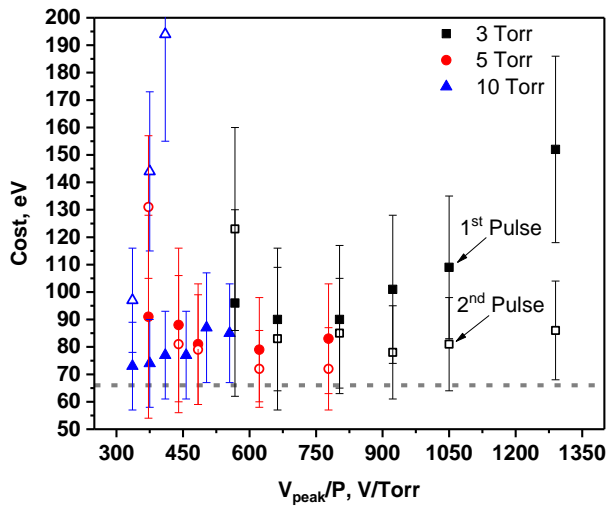
Figure 5.20. Reproduction of figure 5.19 with total cost of ionization included to compare to the 1st and 2nd pulse. The dashed line is the cost associated with Stoletov's point. Error bars have been removed for clarity.



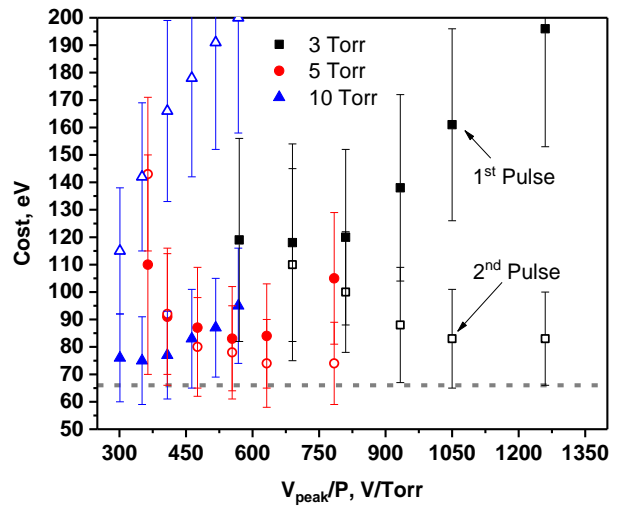
(a) Air, 0.1 kHz



(b) Air, 3 kHz



(c) Air, 10 kHz



(d) Air, 20 kHz

Figure 5.21. Cost of electron ionization for the first and second applied pulse in air plasma. The dashed line is the cost associated with Stoletov's point.

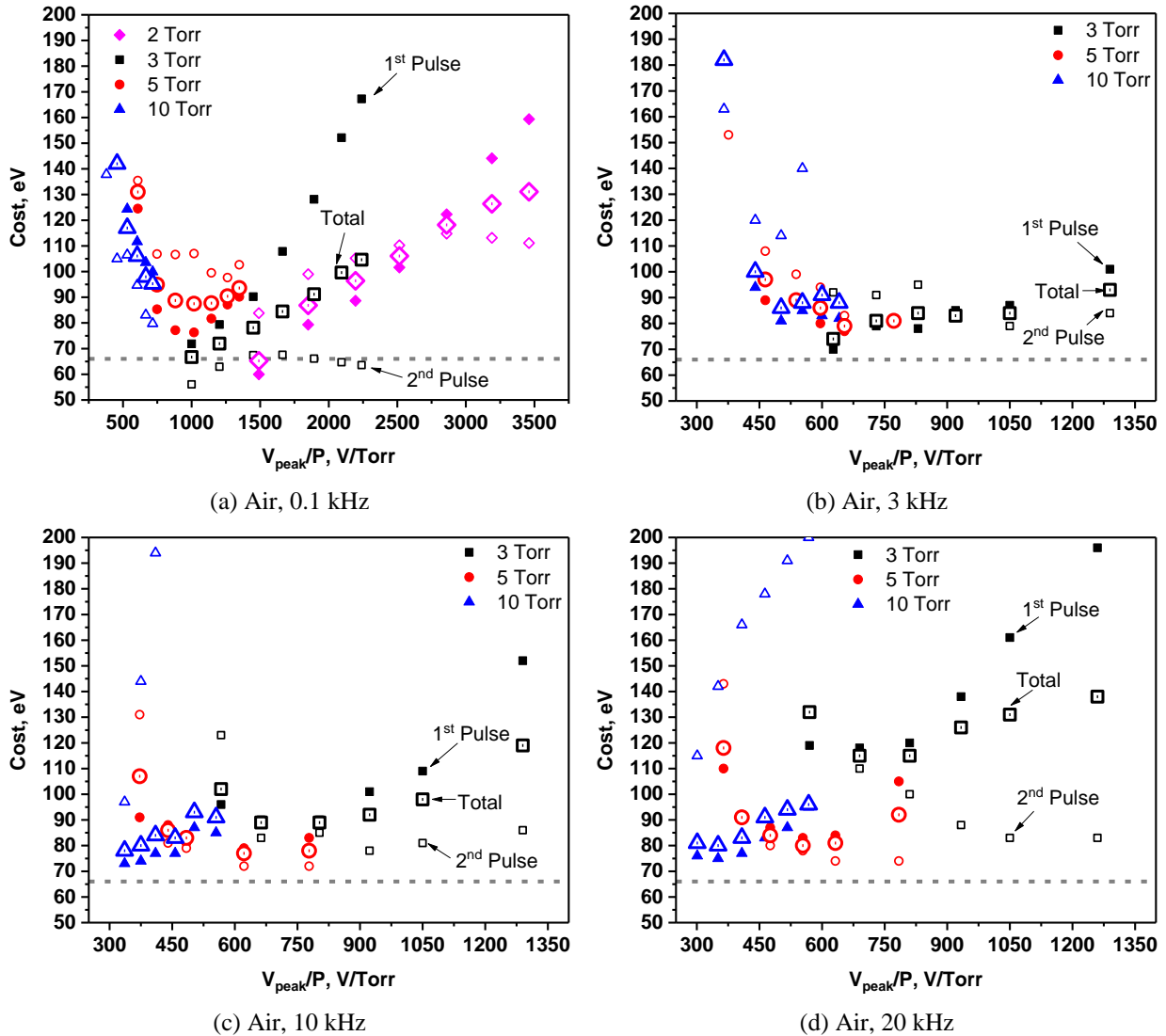


Figure 5.22. Reproduction of figure 5.21 with total cost of ionization included to compare to the 1st and 2nd pulse. The dashed line is the cost associated with Stoletov's point. Error bars have been removed for clarity.

Figure 5.23 shows that the total cost of ionization for air (5.23a-c) and argon (5.23d-f) at the pressures and PRFs tested is within a factor of 2-3 of the cost associated with Stoletov's point. In air, at repetition frequencies of 0.1 and 3 kHz, the total ionization cost tends to increase with pressure at lower voltages. For the same peak voltage, the value of V_{peak}/P decreases with increasing pressure (cf. figure 5.20a and 5.22a). Since voltage is related to the electric field and pressure directly to the gas density, then E/N should also decrease with increasing pressure at these

PRFs. Under these conditions, E/N may be on the left side of Stoletov's minimum (cf. figure 5.2) so that as it decreases, there is an increase in ionization cost. On the other hand, when PRF is increased to 10 and 20 kHz, the cost is higher at 3 Torr (figure 5.23a) than it is at 5 or 10 Torr (figure 5.23b-5.23c) for the same applied voltage. Now, E/N may be on the right side of Stoletov's point and approaches it as E/N falls with increasing pressure causing a reduction in the ionization cost. At 10 Torr, there is no significant variation of cost between 10, 20 and 30 kHz suggesting E/N is similar under these experimental conditions.

In argon, the ionization cost at 0.1 kHz increases with pressure for the same V_{peak}/P (consider costs at V_{peak}/P between 600 and 750 V/Torr in figure 5.20a and figure 5.23d-5.23f). For the same V_{peak}/P , as pressure is increased, V_{peak} increases. The corresponding rise in ionization cost suggests that most of this applied voltage is lost across the cathode sheath [45] with increasing pressure at this PRF. When a repetition frequency of 3 and 10 kHz is applied, the ionization cost is higher at 3 Torr (figure 5.23d) and 10 Torr (figure 5.23f) than at 5 Torr (figure 5.23e) for the same V_{peak}/P (consider costs at V_{peak}/P between 450 and 750 V/Torr). This suggests that the applied voltage at 5 Torr generates an E/N that is closer to Stoletov's point than at 3 and 10 Torr at higher repetition frequencies. Like in air, at 10 Torr, there is no significant variation of cost between 10, 20 and 30 kHz.

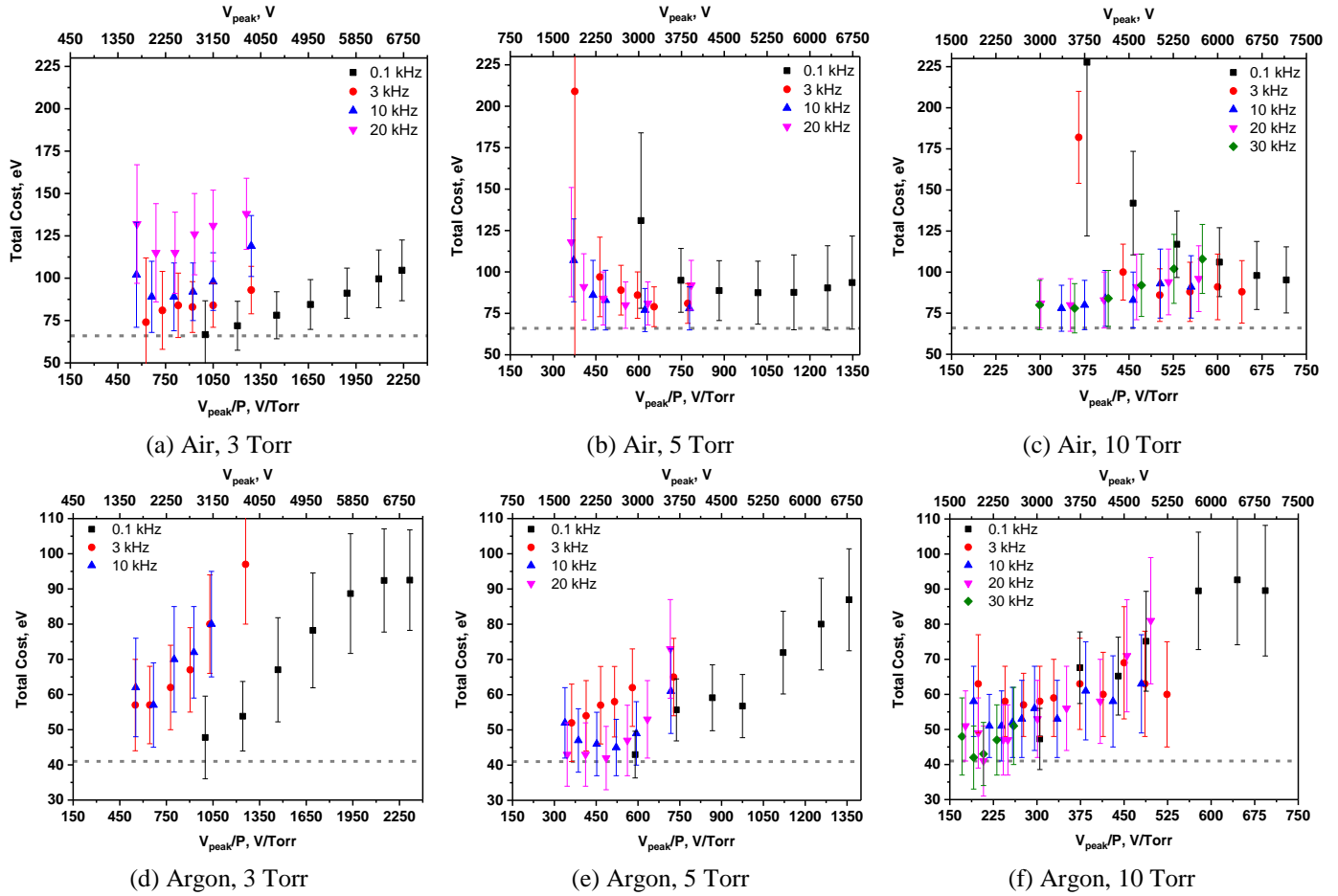


Figure 5.23. Total cost of ionization in air and argon plasma. The top axis shows the V_{peak} corresponding to the V_{peak}/P on the bottom axis.

5.4 Conclusion

Utilizing microwave interferometry for time-accurate measurements of the electron density and two different voltage and current measuring techniques, it was possible to experimentally determine the generated number of electrons and the deposited energy in high voltage nanosecond pulses over a range of pulse repetition rates and gas pressures.

In such parametric studies, increasing the pulse repetition frequency (PRF) for the same commanded voltage considerably reduced the amplitude of the voltage applied to the electrodes. For the same PRF, the shape of the voltage pulse at the electrodes changes with pressure. Changing

these parameters inherently changes the plasma impedance, which makes it difficult to vary the parameters while controlling the voltage pulse shape and magnitude.

In the experiments, the energy deposition varied within an approximate interval of 0.1-1 mJ while the total electron number density, Δn_e , produced per pulse varied from $10^{11} - 7 \times 10^{12} \text{ cm}^{-3}$. The ionization cost in air and argon plasma generated by nanosecond pulses were calculated and found to be within a factor of 2-3 of the theoretical (Stoletov's) minimum. In both gases, varying pulse repetition frequency and gas pressure affect the ionization costs, and changing these parameters may shift E/N either farther from or closer to the optimum regime. In this work, we were able to find a set of conditions in nanosecond pulses that resulted in the ionization cost at its theoretical (Stoletov's) minimum.

An increase in ionization cost at very high voltages suggests that such regime has greater voltage losses across the cathode sheath. To better understand the impact on E/N and voltage loss across the cathode sheath that parameters such as the pulse repetition frequency have, detailed kinetic simulations are needed. The experimental data described in this paper provides a dataset for validation of the models.

6. PLASMA SUSTAINED BY RF BURSTS

Experiments were performed on air plasma sustained by RF bursts to study which conditions were most conducive to producing the highest electron number densities with the lowest cost of ionization. Understanding which operating regime is ideal is imperative to create a plasma antenna that can transmit signals of the driving RF frequency when a plasma is present and receive signals in the plasma afterglow (this is schematically depicted in figure 1.11).

6.1 Experimental Setup

Air plasma at 2 Torr was sustained by RF bursts of 50 MHz sine waves from a Keysight 33600A waveform generator amplified by a 150W A-class RF power amplifier (Amplifier Research, 150A250M3). The output power of, duration of, and decay time between bursts was varied. A Pulsar C50-109-481-1N bi-directional coupler was used to measure the forward and reflected power from which an absorbed power, and in turn the absorbed energy deposited, could be calculated. The electron number density was determined in the same manner as described in 5.2. The experimental setup of figure 5.3a was used and is reproduced in figure 6.1a. The measurement configuration of the directional coupler is shown in figure 6.1b.

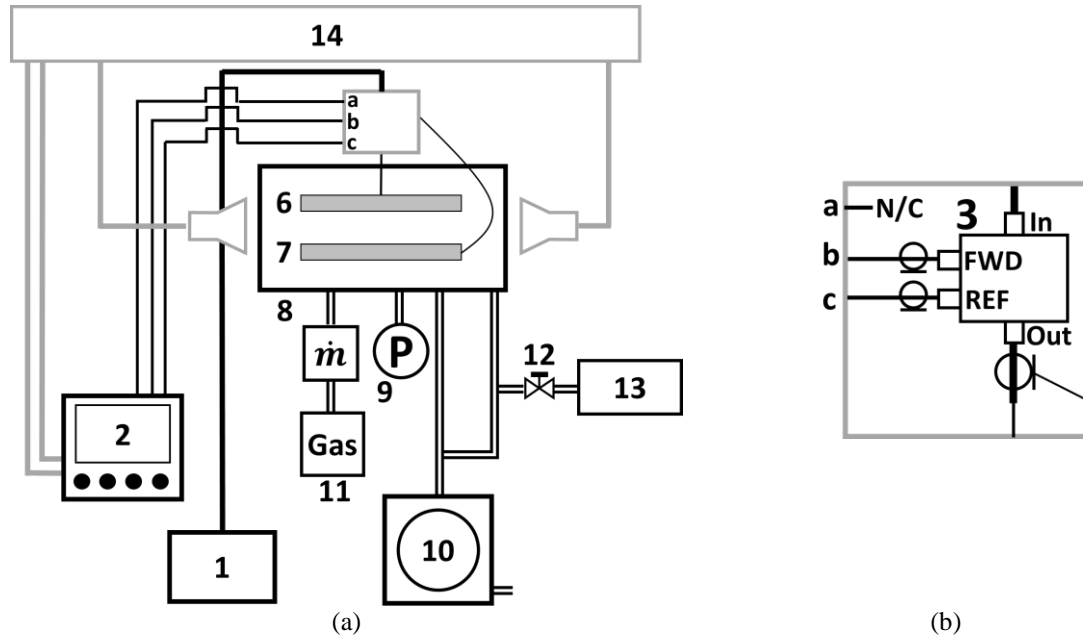


Figure 6.1. (a) Experimental setup (copy of figure 5.3a) and (b) directional coupler used to determine the electron number density and power deposited onto plasma driven by both continuous and pulsed RF waves.

6.2 Results and Discussion

As the commanded power was varied from -6 dBm to -12 dBm for a constant burst duration and frequency, the absorbed power was measured and is shown in figure 6.2a. The measured n_e corresponding to this absorbed power is shown in figure 6.2b. The effects of burst duration and the effects of burst frequency for the same commanded power on absorbed power and electron density are shown in figures 6.3 and 6.4, respectively. A list of the absorbed energy, the change in electron density, and the associated electron cost of ionization per burst for each of these sets of conditions is shown in tables 6.1, 6.2, and 6.3. The data corresponding to 25.1 W from figure 6.2 are shown in black in figures 6.3 and 6.4 to serve as a baseline for comparison.

With increasing commanded power, the maximum average absorbed power increased from 11.4 W to 25.1 W for the same burst duration and time between bursts as seen in figure 6.2a. When commanded power and burst repetition frequency were held constant while burst duration was decreased, figure 6.3a shows that the mean power absorbed increased. Similarly, figure 6.3a shows

the mean absorbed power increases with increasing time between bursts for a constant commanded power and burst duration. Interestingly, in these plots, an overshoot in absorbed power occurs within the first 2-3 μs of the burst, an effect that is most pronounced with increasing power in figure 6.2a and increasing burst repetition frequency in figure 6.3a. The overshoot is most pronounced for the burst duration and frequency that give the lowest initial electron density. In these conditions, it was found that while the incident power was similar, less power was reflected for shorter burst durations and longer time between pulses.

The measured time-averaged n_e increases with power and burst duration while it decreases with increasing burst frequency. Increasing power inherently causes an increase in the energy deposited and therefore the number of produced electrons. Similarly, increasing burst duration allows more time for electrons to be produced, while increasing the time between bursts allows more time for the electrons to recombine.

The ionization cost decreases with increasing absorbed power, increasing time between bursts, and decreasing burst duration. The lowest cost calculated was 8800 eV for 25.1 W of maximum absorbed power applied every 25 μs with a burst duration of 10 μs . This is due to the relatively low energy deposited yet still large electron number density compared to the other conditions tested. For example, in table 6.2, when burst duration is increased from 10 μs to 30 μs , the energy deposited increases by a factor of ~ 2.3 while the Δn_e increases by only a factor of ~ 1.6 . Applying a burst for a longer period wastes more energy without producing more electrons and leads to higher ionization costs.

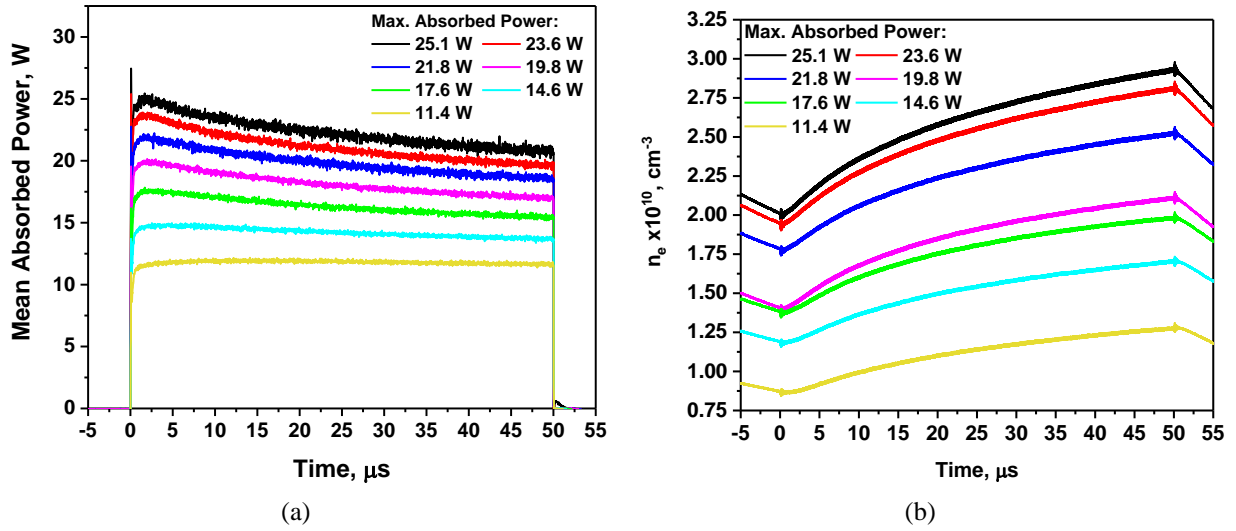


Figure 6.2. Power absorbed and n_e in 2 Torr air plasma sustained by 50 MHz, RF bursts applied every 25 μs for 50 μs .

Table 6.1. The energy deposited, change in electron number density, and ionization cost for the maximum absorbed power indicated. Air plasma at 2 Torr sustained by 50 MHz, 50 μs , RF bursts applied every 25 μs .

Max. Absorbed Power	Energy	$\Delta n_e \times 10^9$	Cost
W	mJ	cm^{-3}	eV
25.1	1.1	9.2	18700
23.6	1.1	8.7	18700
21.8	1.0	7.4	20500
19.8	0.9	6.8	20500
17.6	0.8	6.0	20800
14.6	0.7	5.3	20700
11.4	0.6	4.1	22100

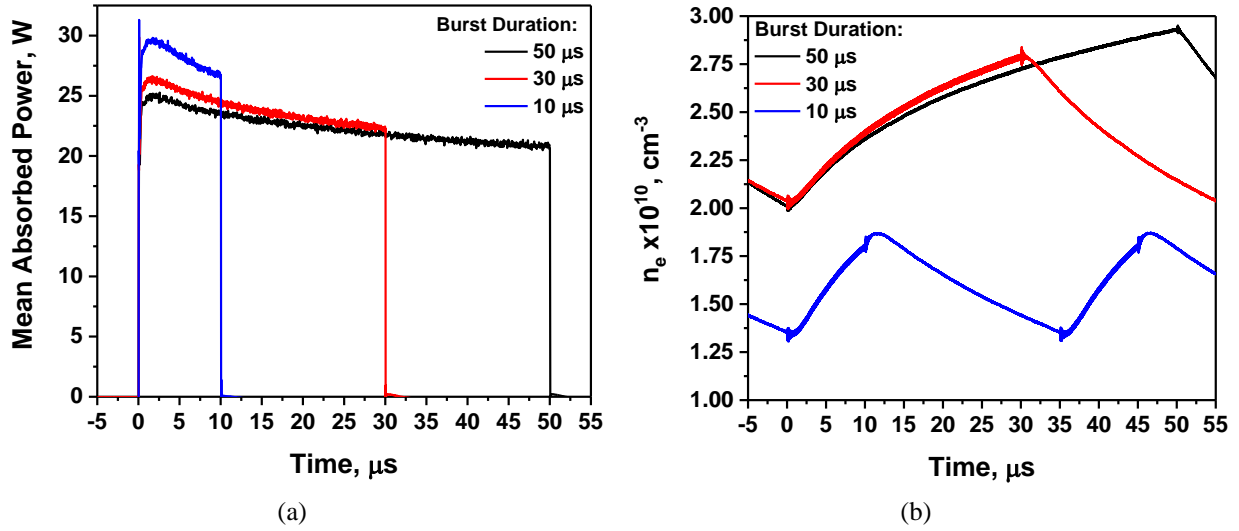


Figure 6.3. Power absorbed and n_e in 2 Torr air plasma sustained by 50 MHz RF bursts applied every 25 μs for 10, 30, and 50 μs . Commanded power was -6 dBm.

Table 6.2. The energy deposited, change in electron number density, and ionization cost for the indicated burst duration. Air plasma at 2 Torr sustained by 50 MHz, RF bursts applied every 25 μs for -6 dBm commanded power (25.1 W maximum absorbed).

Burst Duration	Energy	$\Delta n_e \times 10^9$	Cost
μs	mJ	cm^{-3}	eV
10	0.3	4.9	8800
30	0.7	7.7	14400
50	1.1	9.2	18700

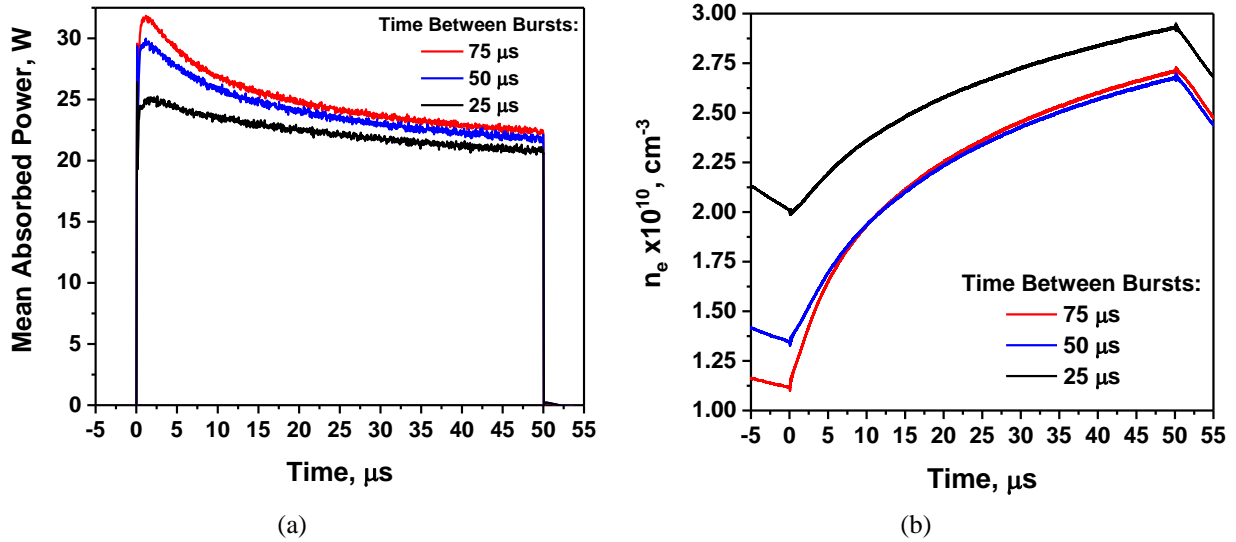


Figure 6.4. Power absorbed and n_e in 2 Torr air plasma sustained by 50 MHz RF bursts applied for 50 μs every 25, 50, and 75 μs . Commanded power was -6 dBm.

Table 6.3. The energy deposited, change in electron number density, and ionization cost for the time between bursts. Air plasma at 2 Torr sustained by 50 MHz, 50 μs RF bursts for -6 dBm commanded power (25.1 W maximum absorbed).

Time Between Bursts	Energy	$\Delta n_e \times 10^9$	Cost
μs	mJ	cm^{-3}	eV
25	1.1	9.2	18700
50	1.2	13.2	14000
75	1.3	15.8	12200

6.3 Conclusion

These experiments in 2 Torr air have shown that it is possible to sustain plasmas with $n_e \approx 10^{10} \text{ cm}^{-3}$ under varying burst conditions. Increasing the power commanded and burst duration while reducing the time between pulses maximizes the electron density. However, this is achieved with high ionization costs in the range of 8000 – 20000 eV. The electron density sustained is comparable to what is produced by low voltage nanosecond pulses (see chapter 2.4) but is 2-3 orders of magnitude less than what is produced at higher peak voltages (see chapter 5.3.3). The ionization

cost of RF bursts is 2-3 orders of magnitude more than what it is for nanosecond pulses (see chapter 5.3.4). Such discrepancy between the two methods may be reduced if higher RF powers are applied at higher pressures and if a different gas, such as argon, is used. At present, the only advantage to nanosecond pulses that plasmas driven by radiofrequency bursts have is that the driving frequency can be transmitted when the pulse is on.

7. PLASMA ANTENNA EXPERIMENTS

7.1 Loop Antenna

Initial experiments with the loop plasma antenna pictured in figure 7.1 have been performed. The antenna was designed to operate at 1.25 GHz and have a thin plasma thickness. This is the traditional approach taken with metallic antennas since the thinner the wire, the more ideally the antenna behaves. The loop was 76 mm in diameter while the Pyrex tubing had an external tube diameter of 6 mm and internal diameter of 4 mm. Neon gas at a pressure of 1 Torr was used. The electrodes are the hollow cylindrical type typically found in neon signs. As evident in figure 7.1, plasma was successfully generated with both FID FPG 10-100MC2-10 and Eagle Harbor NSP-3300-20-F nanosecond pulse generators.

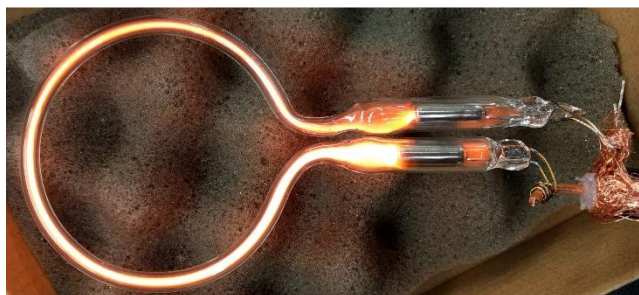


Figure 7.1. The loop plasma antenna designed to operate at 1.25 GHz showing successful ignition of the plasma using a nanosecond pulser.

To measure the electron density, the microwave scattering system described in [86], [87] was used with the help of XingXing Wang in Professor Shashurin's group. The measured quasi-steady averaged n_e within the loop as a function of PRF for a peak pulse voltage of 5 kV using an FID pulser is shown in figure 7.2. As PRF is increased, n_e quickly increases before leveling off. Such saturation occurs because there is insignificant n_e decay between pulses at high repetition frequencies so the quasi-steady, mean n_e should be similar at higher repetition rates. The measured peak n_e within the loop as a function of a single, 100 ns pulse from the Eagle Harbor pulser is

shown in figure 7.3. As expected, n_e increases with voltage. It is unclear why saturation occurs at higher voltages, but one thought is that past a certain n_e , most of the energy of the pulse is lost to joule heating rather than causing further ionization. Both pulsers were able to generate electron densities $\sim 10^{12} \text{ cm}^{-3}$.

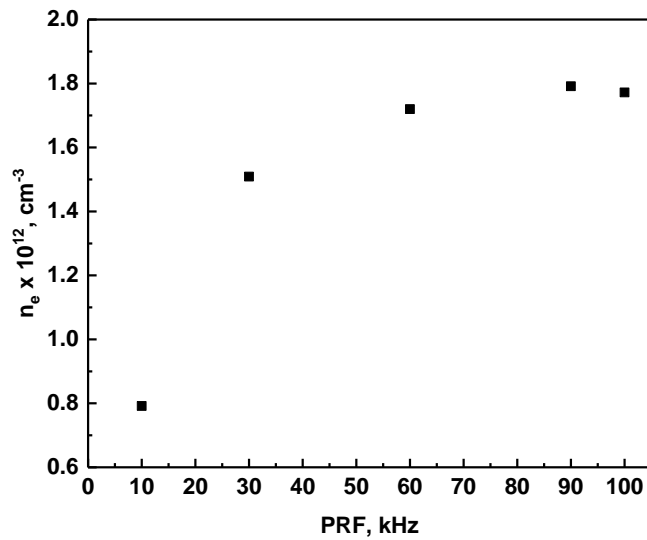


Figure 7.2. n_e as a function of applied PRF. The voltage was fixed at 5 kV with 10 ns pulse width, and an FID pulser was used.

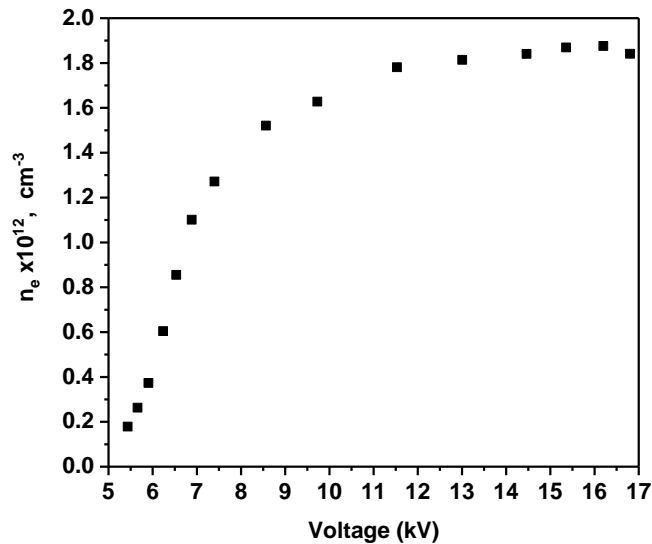


Figure 7.3. n_e as a function of the measured voltage at the electrodes. A single 100 ns pulse was applied at various voltages from the Eagle Harbor pulser.

With preliminary studies showing $n_e \approx 10^{12} \text{ cm}^{-3}$ was achieved, attempts were made to measure S_{11} with a VNA to detect any resonant behavior. A capacitive coupler was made and mounted to the tube as shown in figure 7.4. With the plasma ignited, a frequency sweep from 10s of MHz to a few GHz using a VNA was performed. Unfortunately, no resonant behavior at the design frequency of 1.25 GHz was observed. Several factors may have led to this failure. First, the coupling mechanism was not optimized as no rigorous design process was performed. Furthermore, the components used within the coupler are on such a length scale that they themselves may resonate at GHz frequencies. Moreover, the fast rise time of the ns pulses generates a significant amount of noise that may be inhibiting the detection of a signal. Lastly, the electron number density may not be sufficient to yield a high enough plasma conductivity for resonance to occur.



Figure 7.4. (a) coupler mounted to the plasma antenna and (b) the internal structure of the coupler.

Simulations show that to achieve resonance in the loop antenna with return loss comparable to metallic antennas, an $n_e \geq 10^{13} \text{ cm}^{-3}$ is needed. In literature, others have been able to create functioning plasma antennas with $n_e \approx 10^{10} - 10^{11} \text{ cm}^{-3}$ [12], [28]. They were able to achieve this because, for a given gas pressure, plasmas inherently have higher conductivities for RF frequencies in the MHz range compared to GHz. Moreover, while using thin wires in standard antennas may be ideal for performance, using a plasma column that is too thin may be detrimental. Plasmas have several orders of magnitude smaller conductivities than metals. Since the resistance per unit length, R/l , is inversely proportional to the product of conductance and cross-sectional area, σA , when σ is

comparable in magnitude to A , R/l will be very sensitive to the value of A . Therefore, using thicker tubes should enable us to achieve resonance at lower n_e . Further discussion of this effect is presented in chapter 7.2.3.

7.2 Monopole Antenna

Following attempts to measure the resonant frequency of the loop antenna, the focus shifted to developing a monopole antenna for which more literature exists [9]–[12], [14]. A circuit was developed to measure the reflection coefficient with proper isolation from the high-power excitation source. Initial experiments with light bulbs were performed to test the circuit and find an appropriate coupling scheme. To facilitate simulations of the experiments, it was important to have a plasma antenna with known dimensions in which the gas type and pressure could be controlled. With this variable pressure antenna, measurements of the reflection coefficient as well as the transmission and reception gains were made. Through experiments with a plasma antenna composed of argon at 0.3 Torr, it was found that the plasma antenna return loss could be tuned over a span of 80 MHz by varying the applied power. The antenna gain could also be varied with applied power; when it exceeded 40 W, at some frequencies the gain approached within 3 dB of a standard reference antenna.

7.2.1 Measuring the Reflection Coefficient

To sustain a plasma and make signal measurements through one port, the high-power circuitry shown in figure 7.5 and schematically represented in figure 7.6 was used. Eliminating the need for a dedicated secondary port for signal measurement reduces any parasitic capacitive cross-coupling that may occur between the coupler of each port. By using a directional coupler (Commscope C-10-TCPUSE-N), attenuators (6 dB Weinschel 72-6-43 and a 3 dB, 2 W attenuator), and a

high-pass filter (Mini-Circuits SHIP 300+), the portion of the circuit through which measurement signals travel to and from the plasma antenna is isolated from the high-power source.

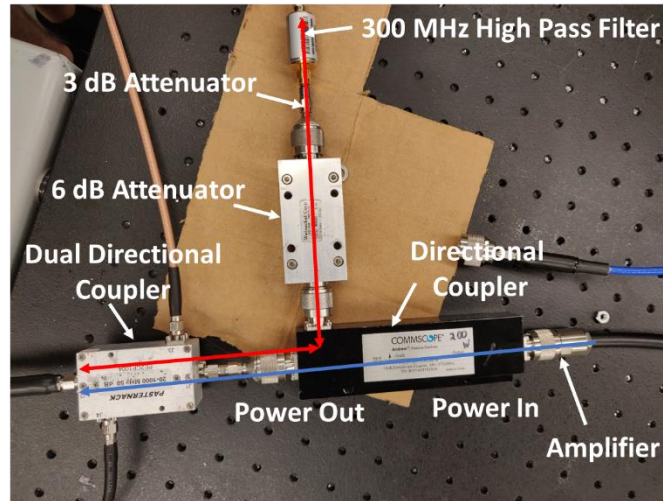


Figure 7.5. Circuitry used to apply the power to the plasma antenna, measure the reflection coefficient, measure the power received by the plasma antenna, and measure the power deposited into the plasma. The blue arrow indicates the path of the excitation signal and the red arrow the path of the antenna signal.

An Agilent E5062A network analyzer was used to measure the reflection coefficient (S_{11}) of the plasma antenna through this circuit. The excitation frequency, f_{ex} , and power, P_{ex} , used to generate the plasma were controlled by a Rhode & Schwartz SM300 signal generator. It was connected to an AR 150A250M3 RF amplifier which can operate at a maximum frequency of 250 MHz and output a nominal power of 150 W. The amplifier was set to its maximum gain so that the power applied was controlled only by the signal generator. The deposited power was measured using a Pasternack PE2CP1004 dual directional coupler and a Lecroy 735Zi oscilloscope. The power and the signals were directly connected to the plasma antenna SMA port without the use of a matching network.

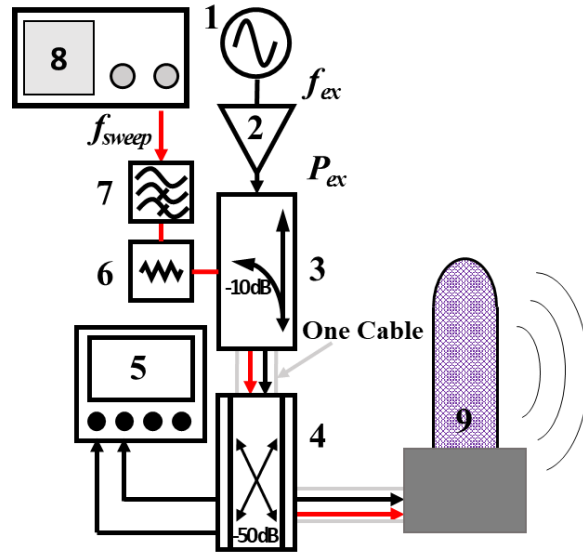
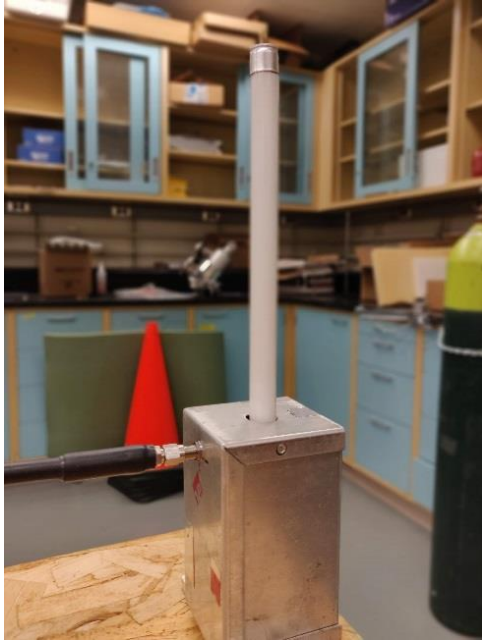


Figure 7.6. Experimental schematic for measuring the S_{11} of the plasma antenna. (1) RF signal generator: excitation frequency (f_{ex}) source; (2) RF power amplifier; (3) directional coupler; (4) dual directional coupler; (5) oscilloscope; (6) attenuator; (7) high-pass filter; (8) VNA; (9) plasma antenna

Fluorescent Light Bulb Monopole

Initially, a 22 cm long light bulb with a 1.3 cm diameter was repurposed as a plasma antenna, as shown in figure 7.7. An aluminum shielding box was used with 16.1 cm of the light bulb protruding from the top. Others have used light bulbs to perform their research on plasma antennas as they are inexpensive and readily available [13], [19], [20], [65]. Using a light bulb provided a means of testing the circuit shown in figure 7.6 and 7.7, and to ensure the coupling scheme could both sustain the plasma and be used to perform measurements. However, since the gas type and pressure could only be guessed, any theoretical or numerical analysis would be inaccurate.



(a)



(b)

Figure 7.7. (a) Fluorescent light bulb repurposed as plasma antenna used for initial monopole tests and (b) the coupling scheme used to both generate the plasma and make measurements.

Plasma was sustained by an excitation frequency of 120 MHz through the coupling scheme shown in figure 7.7b. The S_{11} was measured over the frequency range of 300-2500 MHz and is shown in figure 7.8. It was found that increasing the deposited power caused a decrease in the observed resonance frequency. Increasing the power causes an increase in the plasma column height and electron number density. As the plasma column grows and becomes more conductive, its electrical length approaches its physical length. Since the resonant frequency is inversely proportional to this electrical length, as the length increases, the resonant frequency decreases. Having shown successful surface wave ignition of the plasma, successfully measuring the reflection coefficient, and achieving tunability in resonance frequency, a new antenna was constructed in which all the test parameters could be controlled.

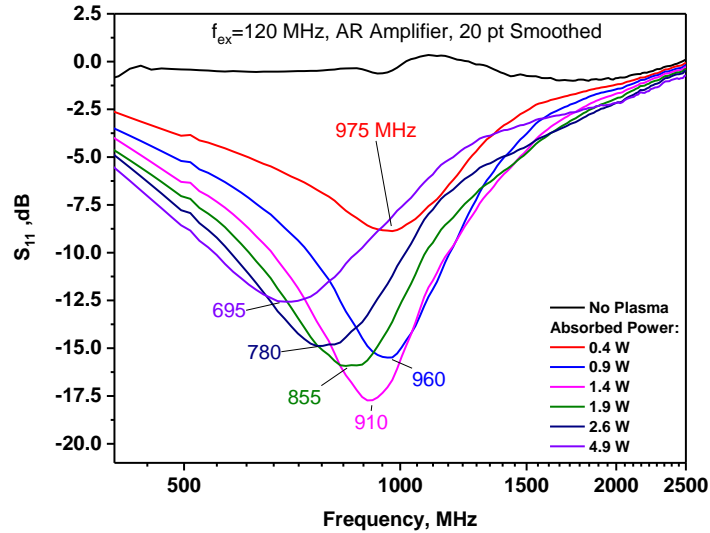


Figure 7.8. S_{11} measurements for indicated deposited power at excitation frequency of 120 MHz.

Variable Pressure Antenna

To conduct parametric studies on a plasma antenna, the system shown in figure 7.9 was constructed, a schematic and dimensions of which are shown in figure 7.10. The plasma antenna itself consists of a 25 mm diameter Pyrex tube connected to a conflat vacuum flange through a glass-to-metal seal. The diameter of the tube was chosen to be thicker than that shown in figure 7.1 or 7.7 in order to improve the conductivity of the plasma column and to match a size commonly found in literature. Moreover, the diameter of the tube was the same as the available glass-to-metal seal on the CF flange.

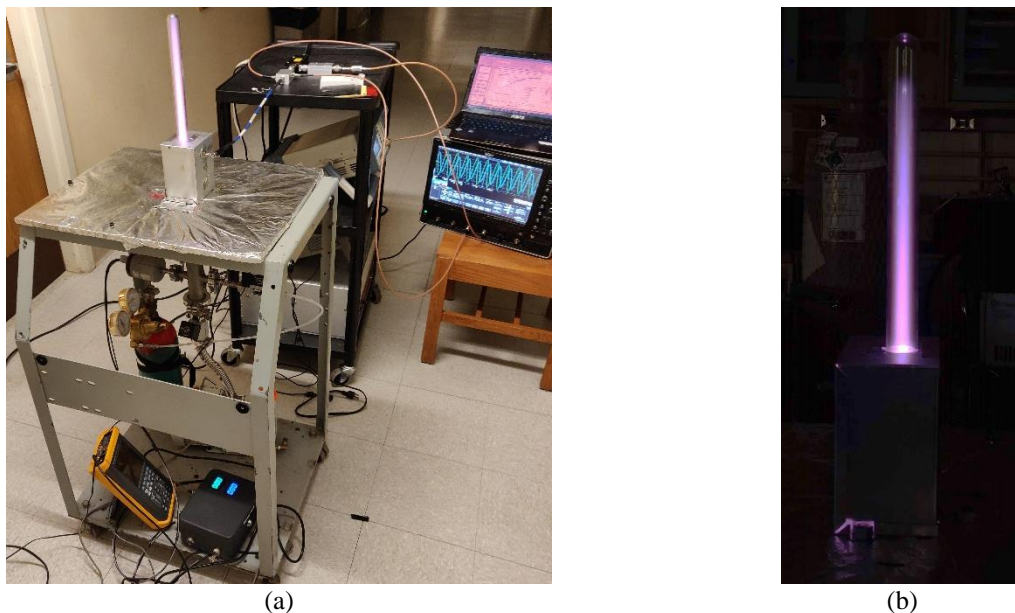


Figure 7.9. The actual variable pressure system used for experiments. (a) shows the system in its entirety during hallway testing with the plasma present while (b) shows a partially ignited plasma column.

The antenna was attached to a 4-way vacuum cross as shown in figure 7.10b. Gas was evacuated using an Edwards E2M-1 rotary vane vacuum pump while pressure was controlled using an Alicat MC-200 flow controller in conjunction with a throttling valve (modified VAT 265 KF16 Valve). Pressure was measured using an MKS 626C capacitance manometer. Argon gas with 99.995% purity was introduced through the mass flow controller.

It was necessary to ensure that any air present in the hose between the gas cylinder and mass flow controller was removed before flowing argon. To do so, the mass flow controller was set to its maximum flow rate with the gas cylinder closed and the vacuum pump on. When the pressure inside the plasma antenna system reached below 10 mTorr, argon was introduced. The system was flushed for 20 minutes at 4.3 Torr before the mass flow rate was reduced to achieve the desired pressure.

The ground plane consisted of aluminum foil wrapped around plywood and secured to a metallic cart (cf. figure 7.9a). The height and alignment of the Pyrex tube above the ground plane

were controlled by adjusting nuts on three pieces of all-thread secured to the plywood. An aluminum shielding box enclosed the bottom of the Pyrex tube above the ground plane. Inside was a coupler constructed from copper tape and soldered to an SMA cable as shown in figure 7.11. It was connected to an SMA bulkhead through which the excitation and measurement signals were applied.

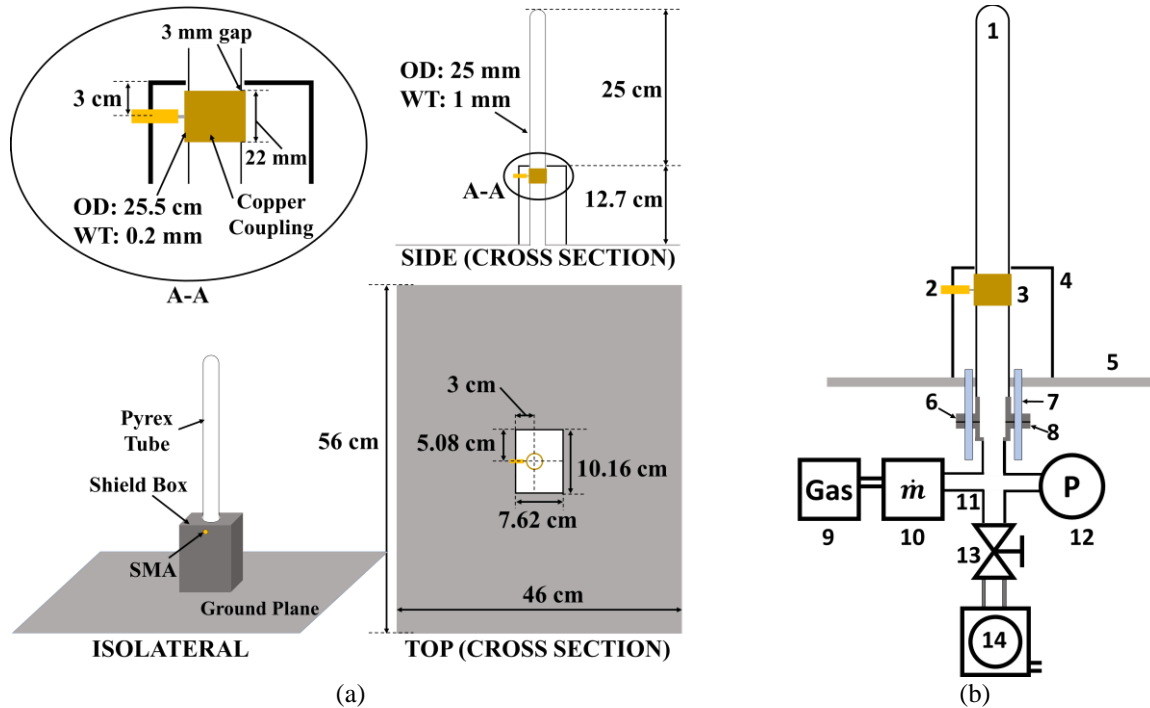


Figure 7.10. Schematic of the variable pressure plasma antenna system. System dimensions are shown in (a) and relevant components in (b). In (b): (1) Pyrex glass tube; (2) SMA connector; (3) copper coupling sleeve; (4) aluminum shield box; (5) ground plane; (6) CF 2.75 glass-to-metal sealed flange; (7) threaded rod; (8) CF 2.75 to KF-40 adapter; (9) argon gas supply; (10) mass flow controller; (11) KF-40 to KF-16 4-way cross reducer; (12) pressure gauge; (13) modified open-close valve; (14) vacuum pump

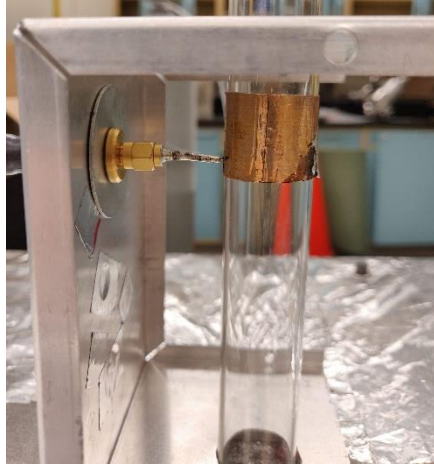


Figure 7.11. Copper coupler soldered to SMA cable and connected to a SMA bulkhead.

With this system constructed, initial tests were performed to find an optimum pressure and frequency to conduct the parametric studies with the AR amplifier. It was found that with the excitation frequencies tested, operating at pressures approaching 1 Torr caused plasma striations to form. To avoid them, the operating pressure was chosen to be 0.3 Torr (at a flow rate of 0.0115 ± 0.0005 g/min). It has also been shown that lower collision frequencies are beneficial to surface wave propagation and plasma antenna operation [9]–[11], [33]].

Other coupling schemes and shielding box configurations, such as that shown in figure 7.12, were also considered and tested. However, it was found that while the entire column could be filled with plasma, no significant S_{11} measurements could be made regardless of coupler positioning above or below the ground plane. This coupling scheme, among others, should be tested with higher excitation frequencies applied through an impedance matching network.

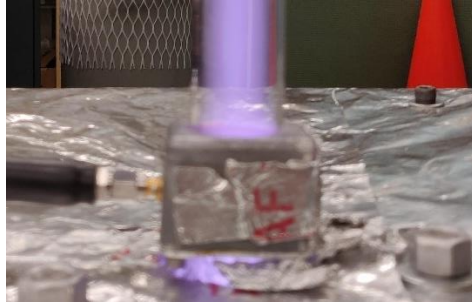


Figure 7.12. Alternative coupler tested.

To ensure the coupler worked as intended, a thin layer of aluminum foil was wrapped around the length of the Pyrex tube. A frequency sweep between 150 MHz and 250 MHz was applied by the VNA through the measurement circuit of figure 7.5, without the SHP-300+ filter. A resonant frequency of 196 MHz was measured, as shown in figure 7.13. This frequency corresponds to a quarter-wavelength of 38.1 cm which was in fact the length of the tube. This verified the reliability of our coupling scheme.

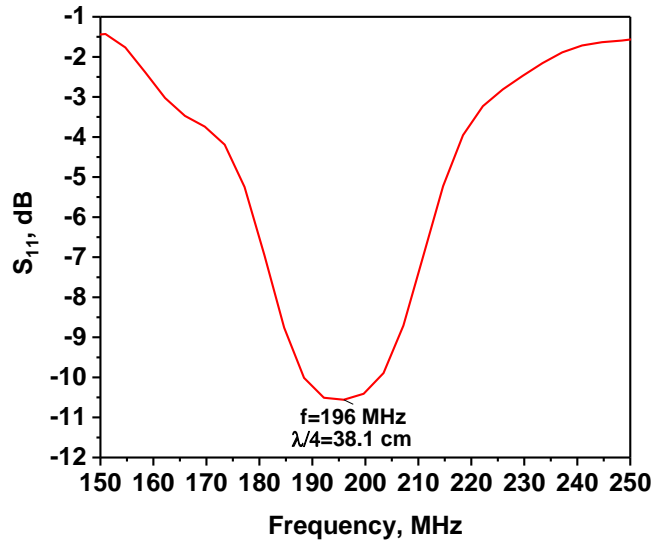


Figure 7.13. Results from Aluminum foil wrapped Pyrex tube to validate S_{11} measurement setup.

S_{11} data was acquired by performing a 1000-point frequency sweep from 300-600 MHz at a VNA probing power of 10 dBm. Lower frequencies weren't used since the SHP-300+ high pass filter limited detecting reflection coefficients corresponding to frequencies below 300 MHz.

Frequencies above 600 MHz showed no resonance under the conditions tested. 100-point averaging was used on the acquired data to reduce noise.

The S_{11} response varied with frequency and power applied to the plasma. Consider figure 7.10 which shows the response of the system at an excitation frequency of 98 MHz (figure 7.10a) and 154.5 MHz (figure 7.10b). In each plot, the deposited power measured is different; however, in both cases, the commanded, incident power was the same. It was not possible to reach the maximum powers deposited by $f_{ex}=98$ MHz with $f_{ex}=154.5$ MHz. At $f_{ex}=154.5$ MHz, a 15 W variation in deposited power (from 56 W to 71 W) caused about a 60 MHz shift in resonant frequency (from 320 MHz to 380 MHz). At $f_{ex}=98$ MHz, to get the similar 60 MHz shift (in this case, from 385 MHz to 445 MHz), the deposited power was increased by 34 W (from 10.5 W to 44.5 W). This suggests that into an unmatched plasma load, the excitation frequency with which a plasma is sustained changes the plasma impedance. In turn, the deposited energy and the antenna performance vary for the same sweep frequency range.

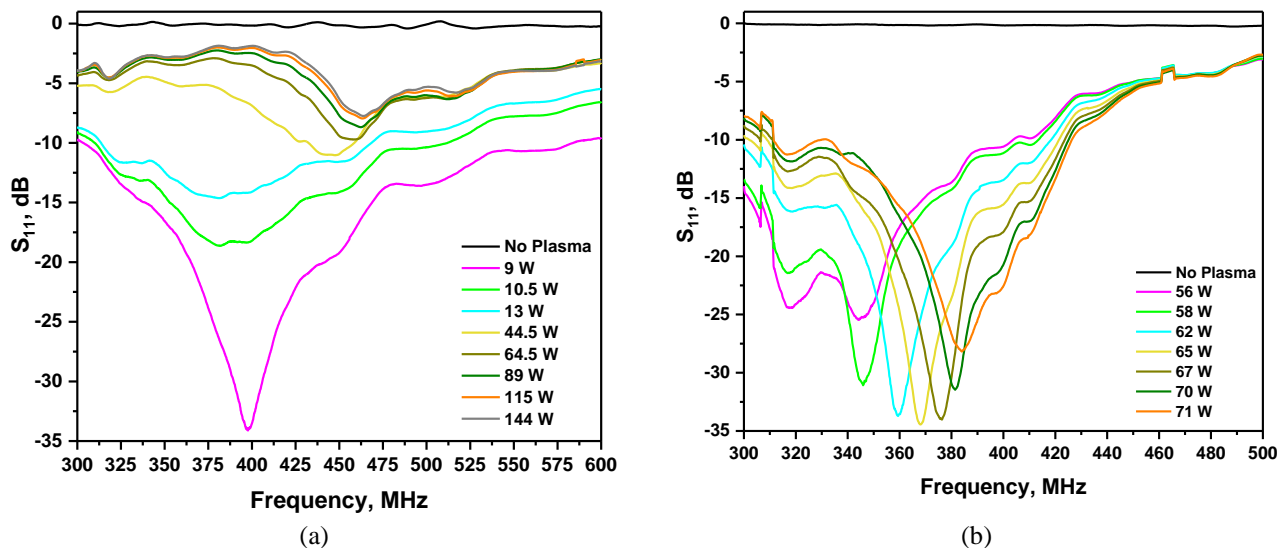


Figure 7.14. S_{11} response measured for excitation frequencies of (a) 98 MHz and (b) 154.5 MHz at the indicated deposited powers into an argon plasma at 0.3 Torr. The sudden peaks at 309 and 463 MHz in (b) correspond to the 2nd and 3rd harmonics of the excitation frequency leaking into the measurement system.

For both excitation frequencies in figure 7.14, the resonance frequency increases with increasing power, a trend different from what was observed in figure 7.8 with the light bulb plasma antenna. This occurs even after the entire 25 cm length of the column above shielding box is filled with plasma. Since the plasma conductivity is proportional to n_e , the electrical length and plasma column length may differ.

In standard antennas, the frequency at which S_{11} has a minimum corresponds to the antenna's resonant frequency. However, a plasma antenna may absorb a signal in addition to transmitting it. Moreover, the plasma antenna's input impedance can vary with power, frequency, gas type, and pressure. The S_{11} measured may therefore correspond to the frequency at which the antenna impedance matches that of the transmission line rather than the antenna resonance frequency and should be further investigated through modelling. Therefore, to experimentally understand if the plasma column behaves as an antenna, it was necessary to measure its gain.

7.2.2 Determining Gain

Reference Antenna

The gain of an antenna describes how much power is transmitted or received from the direction of peak radiation and is a combined measure of its directivity and efficiency. To determine the gain of our reference antenna (Taoglas FW.45.B.SMA.M), the Friis Transmission equation was used. It relates the antenna's transmitted and received powers to their gains, to the signal frequency, and to the free space distance. The relation is valid so long as the receiving antenna is in the far-field of the transmitting antenna and no objects obstruct the signal's path. It is given by

$$P_{Rx} = P_{Tx} G_{Tx} G_{Rx} \left(\frac{c}{4\pi r f} \right)^2 \quad (7.1)$$

where P_{Rx} is the received antenna power, P_{Tx} is the transmitted antenna power, G_{Rx} is the receiving antenna gain, G_{Tx} is the transmitting antenna gain, c is the speed of light, r is the distance between the two antennas, and f is the signal frequency. Dividing by P_{Tx} and converting into decibels gives

$$10 \log \left(\frac{P_{Rx}}{P_{Tx}} \right) = G_{Tx} + G_{Rx} + 20 \log \left(\frac{c}{4\pi r f} \right) \quad (7.2)$$

If the transmitting and receiving antenna are identical, then $G_{Tx} = G_{Rx} = G_{Ref}$. Therefore, if r , P_{Rx} and P_{Tx} are all known, the antenna gain can be determined:

$$5 \log \left(\frac{P_{Rx}}{P_{Tx}} \right) - 10 \log \left(\frac{c}{4\pi r f} \right) = G_{Ref} \quad (7.3)$$

For this experiment the antennas were spaced with a line of sight distance of $r=7.2$ m. Due to the long wavelengths at the frequencies tested and the limited amount of space to conduct these experiments, the hallway walls were located within the antenna near-field.

To determine the transmitted and received power, the configuration shown in figure 7.15 was used. It is the same as that displayed in figure 7.9 except that the VNA has been replaced with an Agilent E4408B spectrum analyzer, the Rhode and Schwartz SM300 was now used to sweep over the transmitted frequencies, f_{Tx} , and a Keysight 33600A waveform generator was used to control f_{ex} and P_{ex} . To account for cable and measuring losses, the spectrum analyzer was used to determine the circuit loss as a function of frequency (~ 19.2 dB on average) for a known P_{Rx} . This loss was then accounted for in post-processing. P_{Tx} was directly measured by the spectrum analyzer at the antenna input.

The transmitted frequency was swept from 400-480 MHz with a 100 kHz step size and 16 ms dwell time per step for various P_{Tx} . Different powers were used in order to verify consistency in the reference gain profile and its independence on P_{Tx} . The spectrum analyzer was swept over the same frequency range with a 300 kHz RBW and VBW, and a 4 ms dwell time. Therefore, the

spectrum analyzer would take four samples per frequency for a given sweep and the MAX HOLD function was used to keep the maximum. Multiple measurement sweeps were performed to ensure the proper signal is detected since there was no way to synchronize the two devices.

Equation (7.3) was used to generate the reference antenna gain profile shown in figure 7.16a by using the measured powers and accounting for system losses. A comparison of the reference antenna's measured gain to its gain profiles provided in the manufacturer's datasheet is shown in figure 7.16b. The measured gain profile maintains its shape regardless of transmitted signal strength. The maximum measured gain is between 5 and 6 dBi suggesting that the reference antenna in this configuration is not omnidirectional. Most likely this is due to reflections from the walls present in the near-field on two sides of the reference antennas. These reflections and the circuit used to measure the received power are believed to explain the ripples in the gain profile. Such environmental conditions may also explain the differences between the measured and datasheet-provided gain profiles.

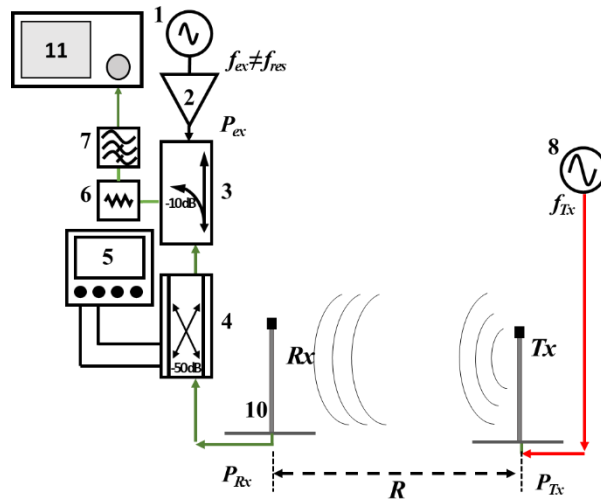


Figure 7.15. Configuration used to determine the gain of the reference antenna. (1) RF signal generator: excitation frequency (f_{ex}) source; (2) RF power amplifier; (3) directional coupler; (4) dual directional coupler; (5) oscilloscope; (6) attenuator; (7) high-pass filter; (8) RF signal generator: frequency sweep (f_{Tx}) source; (10) reference antenna; (11) spectrum analyzer

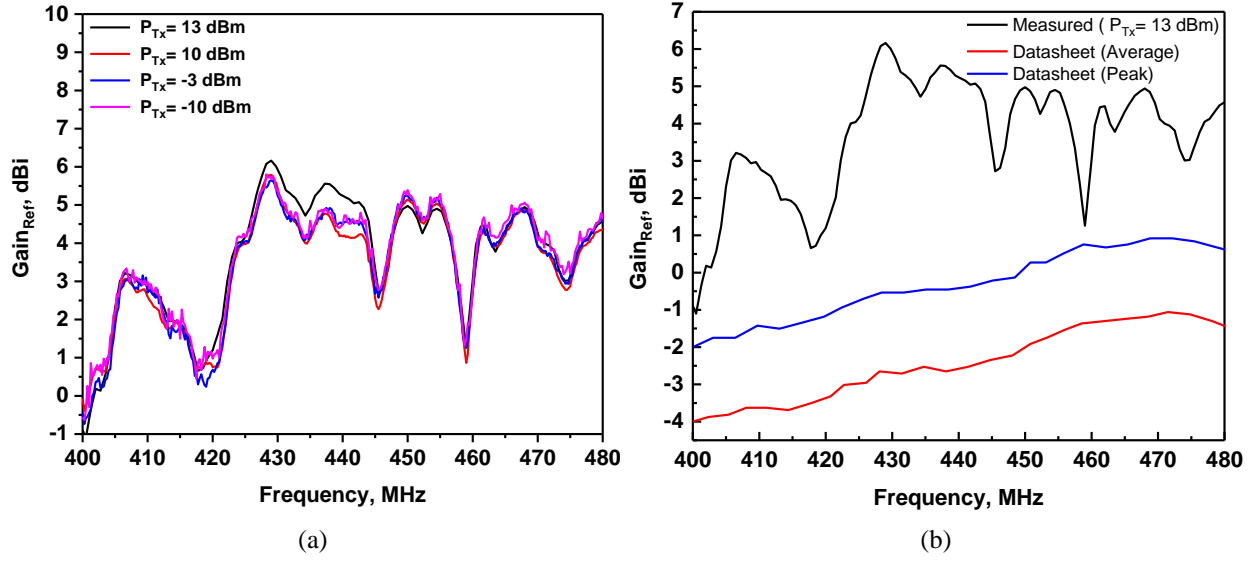


Figure 7.16. (a) Measured gain of the reference antenna for varying transmitted powers, and (b) a comparison of the reference antenna's measured gain to its gain profile in the antenna datasheet.

Variable Pressure Plasma Antenna

The gain of the plasma antenna both as transmitter and a receiver was measured using the comparison technique, shown schematically in figure 7.17. First, the plasma antenna is used to transmit a signal of known power and an antenna with known gain is used to receive it. Next, a reference antenna, also with known gain, is put at the exact same location and the process is repeated. Consider equation (7.1) written in terms of the plasma antenna

$$P_{Rx,PTx} = P_{Tx} G_{Rx} G_{PTx} \left(\frac{c}{4\pi r f} \right)^2 \quad (7.4)$$

and in terms of the reference antenna

$$P_{Rx,RTx} = P_{Tx} G_{Rx} G_{RTx} \left(\frac{c}{4\pi r f} \right)^2 \quad (7.5)$$

where $P_{Rx,PTx}$ and $P_{Rx,RTx}$ is the power measured by the receiving antenna for a signal transmitted by the plasma and reference antenna, respectively, while G_{PTx} and G_{RTx} is the transmission gain of the plasma and reference antenna, respectively. G_{Rx} is the gain of the receiving antenna.

Since the receiving antenna and reference antenna are identical, their gains are identical. Therefore, $G_{RTx}=G_{Rx}=G_{Ref}$. Using these relations and taking the ratio between equation (7.4) and (7.5) gives

$$\frac{P_{Rx,PTx}}{P_{Rx,RTx}} = \frac{G_{PTx}}{G_{Ref}} \quad (7.6)$$

which can then be rearranged to give the transmission gain profile of the plasma antenna

$$\frac{P_{Rx,PTx}}{P_{Rx,RTx}} G_{Ref} = G_{PTx} \quad (7.7)$$

For convenience, equation (7.7) can be transformed into units of dB

$$10 \log \left(\frac{P_{Rx,PTx}}{P_{Rx,RTx}} \right) + G_{Ref} [dB] = G_{PTx} [dB] \quad (7.8)$$

This same procedure, with just a few modifications, is performed to determine the gain profile of a plasma receiver. Equations (7.4) and (7.5) become, respectively,

$$P_{PRx,RTx} = P_{Tx} G_{Tx} G_{PRx} \left(\frac{c}{4\pi r f} \right)^2 \quad (7.9)$$

$$P_{RRx,RTx} = P_{Tx} G_{Tx} G_{RRx} \left(\frac{c}{4\pi r f} \right)^2 \quad (7.10)$$

where $P_{PRx,Tx}$ and $P_{RRx,Tx}$ is the power received by the plasma and reference antenna, respectively, while G_{PRx} and G_{RRx} is the reception gain of the plasma and reference antenna, respectively. G_{Tx} is the gain of the antenna transmitter. Since the receiving antenna and transmitting reference antenna are identical, $G_{RRx}=G_{Tx}=G_{Ref}$. Performing the same operations as previously described gives G_{PRx} in units of dB

$$10 \log \left(\frac{P_{PRx,Tx}}{P_{RRx,Tx}} \right) + G_{Ref} [dB] = G_{PRx} [dB] \quad (7.11)$$

The measured transmitter and receiver gain of the plasma antenna is shown in figure 7.18a and 7.18b, respectively, for an argon plasma column sustained by various powers at a pressure of

0.3 Torr and excitation frequency of 98 MHz. A plot of the gain as a function of deposited power for three different signal frequencies under the same conditions is plotted in figure 7.19. For the transmission gain, $P_{R_x, P_{T_x}} = 10$ dBm was used since it was identical to the VNA power when measuring S_{11} . For the reception gain, $P_{T_x} = 13$ dBm (the maximum power output of the SM300) in order to maximize the signal strength received by the plasma antenna. Subsequent experiments utilized $P_{T_x} = -3$ dBm and -10 dBm to determine how weak of a signal the plasma antenna could detect. These results are shown in figure 7.20.

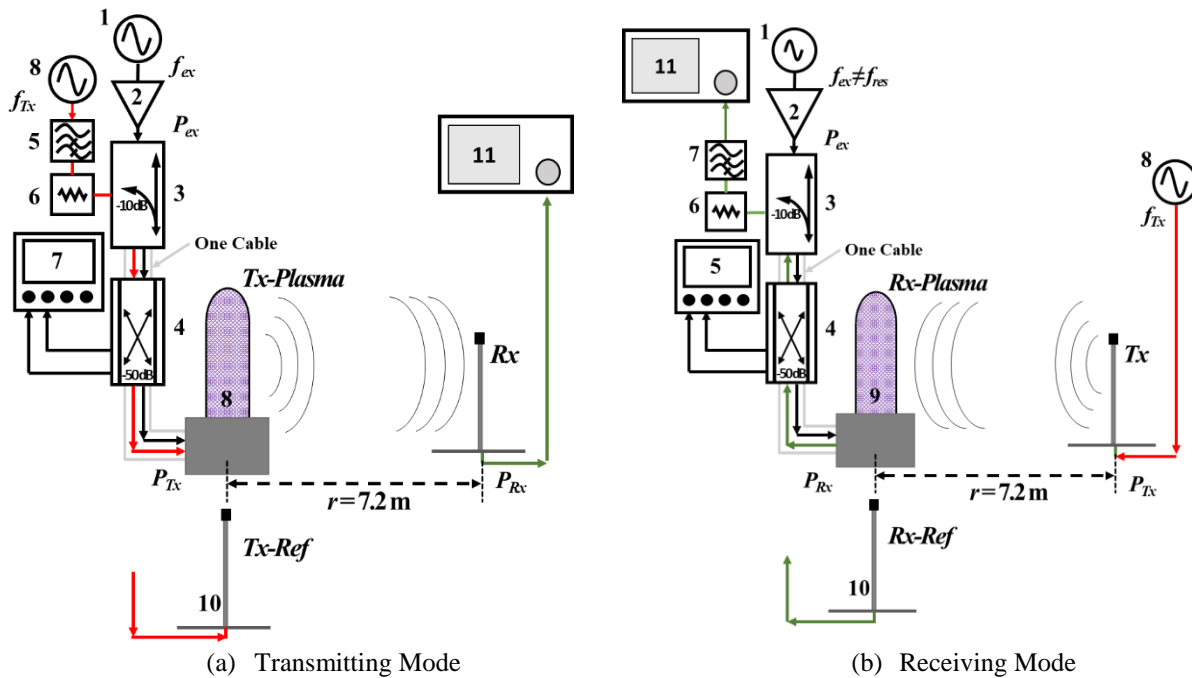


Figure 7.17. Experimental schematic for measuring the (a) transmitted (P_{T_x}) and (b) received power (P_{R_x}) by the plasma and reference antennas to determine antenna gain. (1) RF signal generator: excitation frequency (f_{ex}) source; (2) RF power amplifier; (3) directional coupler; (4) dual directional coupler; (5) oscilloscope; (6) attenuator; (7) high-pass filter; (8) RF signal generator: frequency sweep (f_{Tx}) source; (9) plasma antenna; (10) reference antenna; (11) spectrum analyzer

From both figure 7.18a and 7.18b, as deposited power is increased, the overall gain increases as well. Increasing deposited power increases n_e which causes an increase in the plasma conductivity. As the plasma becomes more conductive, the antenna signals can more easily propagate along the plasma column with less attenuation. The antenna is thus more efficient and

has an improved gain with increasing power. However, as depicted more clearly in figure 7.19, beyond a certain applied power, in this case 40 W, the gain plateaus. Exceeding this threshold power only serves to heat the plasma without drastically improving antenna performance, thereby wasting energy. A similar leveling off effect was previously observed by Naito et. al. in their studies of antenna gain for the radiation of the surface wave (f_{ex}) [11].

Figure 7.18 also shows the formation of a clear peak at ~ 417 MHz in both transmitting and receiving modes when the deposited power exceeds 10.5 W. This peak is indicative of the antenna's resonant frequency. By increasing the power supplied to the column even after the Pyrex tube was entirely filled with plasma, it is possible to improve, and thereby tune, the resonant strength of the antenna. For deposited powers of 64.5 W and above, the transmission gain at a frequency ≈ 417 MHz is within 1 dB and the reception gain is within 3 dB of the reference antenna. On the other hand, in the absence of plasma, this resonant peak disappears, the overall gain profiles do not exceed -18 dBi, and the structure is no longer an antenna. This resonance frequency is different from the ≈ 460 MHz determined by the VNA measurement of the reflection coefficient for the same power (cf. figure 7.14), the reasoning for which should be further explored.

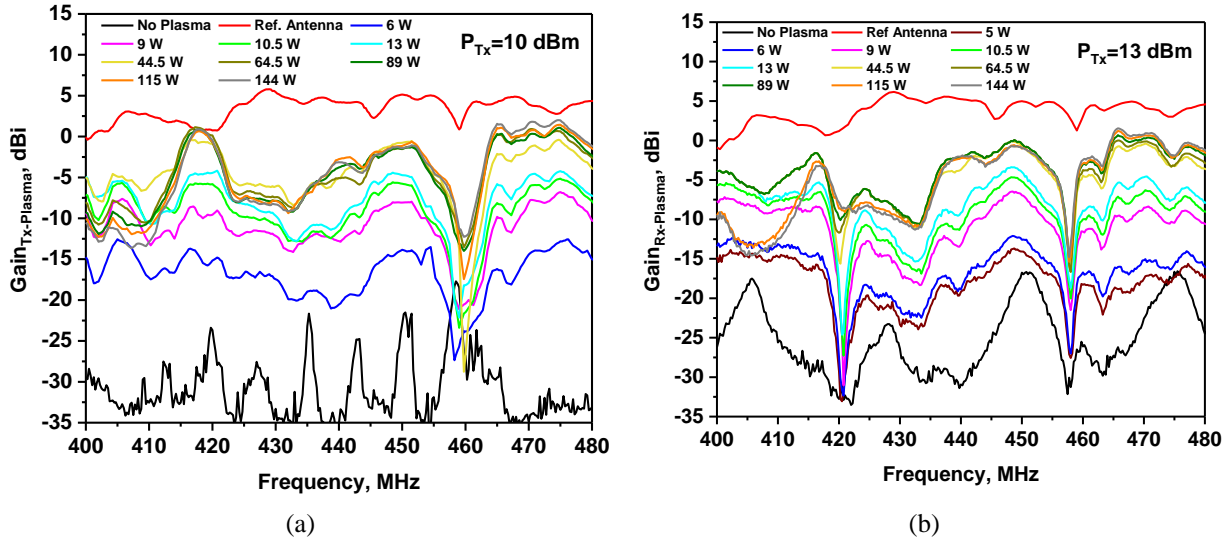


Figure 7.18. The measured (a) transmitting and (b) receiving gain profile for the plasma antenna. An argon plasma at 0.3 Torr was sustained by the indicated deposited power at $f_{ex}=98$ MHz.

In figure 7.19, a clear jump in deposited power is seen between 18 W and 40 W. Visually, an increase in the plasma brightness was observed with this power increase. Such behavior is believed to be caused by the impedance matching of the plasma antenna to the transmission line at the surface wave excitation frequency. As shown in figure 7.22 in the next section, the electron number density of the plasma increases with applied power. For a constant signal frequency, the real part of the plasma impedance decreases with increasing n_e (i.e. its resistance decreases). As the resistance approaches the 50Ω value of the transmission, less power is reflected. At some point, the reactive part of the impedance may also approach zero. These effects cause the plasma to be better matched and more power to be deposited.

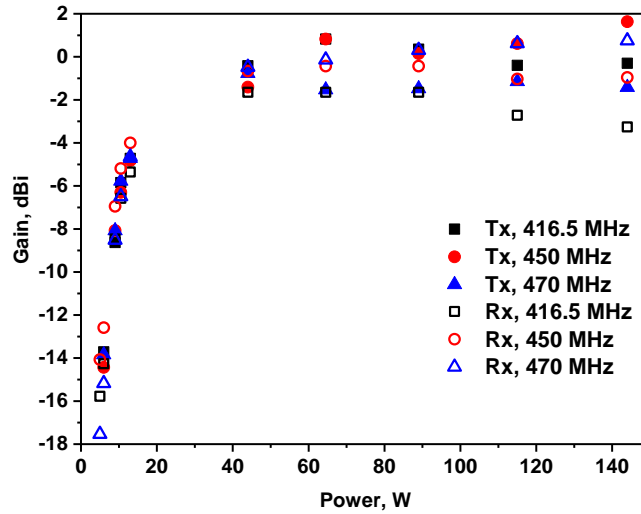


Figure 7.19. The measured transmitting and receiving gain as a function of applied power at a few different signal frequencies. An argon plasma with gas pressure of 0.3 Torr was sustained at $f_{ex}=98$ MHz in each case.

Figure 7.20 shows that regardless of the transmitted power, the overall gain profile of the plasma antenna as a receiver is similar. Though, as the transmitted power is decreased, the noise of the measured signal increases. It is believed this occurs because the signal strength is becoming comparable to the thermal noise of the plasma antenna.

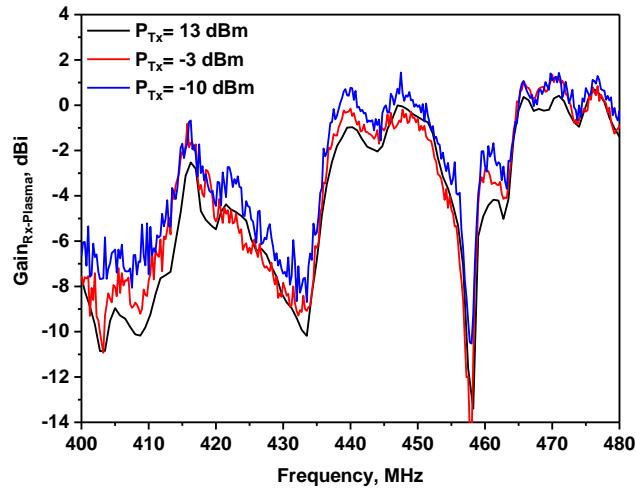


Figure 7.20. Gain profile of a plasma antenna as a receiver for varying transmission output powers. An argon plasma with gas pressure of 0.3 Torr was sustained by 64.5 W at $f_{ex}=98$ MHz in each case.

7.2.3 Antenna Resistance and Skin Depth Analysis

As seen in figure 7.18, if the power is high enough, the gain of the plasma antenna can match that of the reference metallic antenna. There is considerable uncertainty (at least several dB) in the measurements of the two antennas' gain because of the hallway walls present in the antenna near-field. A more precise comparison statement is that the plasma antenna gain is within 6-10 dB of that of the reference antenna. This may seem somewhat surprising, since the electrical conductivity of the plasma is many orders of magnitude lower than the conductivity of a metal. However, the resistances of the plasma column, as well as of a metal rod, are also affected by the skin effect.

In metals, the skin depth is given by

$$\delta = \sqrt{\frac{\rho}{\pi f \mu_o \mu_r}} \quad (7.12)$$

where ρ is the resistivity of the metal, f the wave frequency, and μ_o and μ_r the free space and relative permeability, respectively. According to the antenna datasheet, the antenna material is steel. It is assumed that the average resistivity of steel is $\rho_{steel} = 43 \mu\Omega\text{-cm}$ and μ_r in the range of 100 – 1000.

In the frequency range of 400 – 480 MHz, an argon plasma sustained at 0.3 Torr with $n_e \approx 3 \times 10^{11} \text{ cm}^{-3}$ (cf. figure 7.27) has a permittivity whose imaginary party is less than the magnitude of the real part, as seen in figure 7.21. Therefore, the effective skin depth is given by a penetration depth defined as

$$\delta_{penetration} = \frac{\lambda}{2\pi\sqrt{|\epsilon_r|}} \quad (7.13)$$

where λ is the wavelength in free space and ϵ_r the real part of the permittivity given by

$$\epsilon_r = 1 - \frac{\omega_p^2}{\omega^2 + \nu_m^2} \quad (7.14)$$

where ν_m is the electron-neutral collision frequency, ω_p the plasma frequency, and ω the angular frequency of the propagating wave. At 0.3 Torr argon, $\nu_m \approx 1.59 \times 10^9 \text{ s}^{-1}$. At $n_e \approx 3 \times 10^{11} \text{ cm}^{-3}$, $\omega_p = 3.09 \times 10^{10} \text{ s}^{-1}$. The calculated skin depths of the antennas used are shown in figure 7.22.

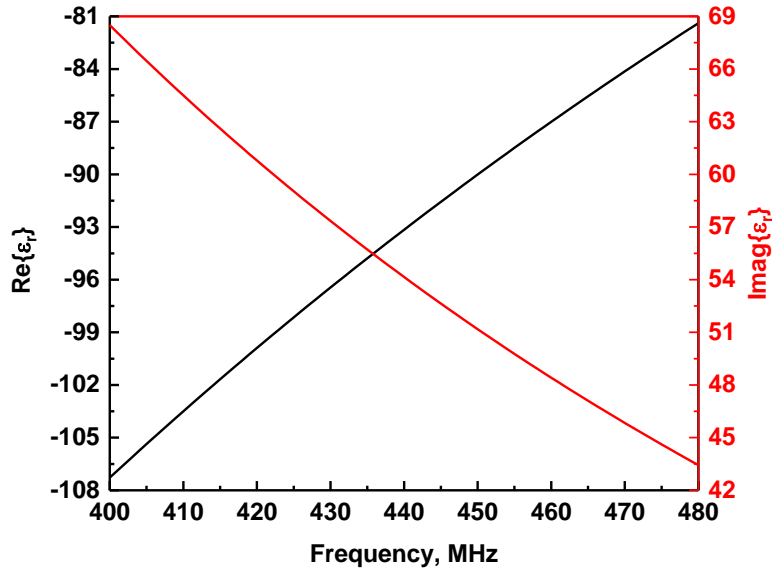


Figure 7.21. Real and imaginary parts of the plasma permittivity for an argon plasma at 0.3 Torr with $n_e \approx 3 \times 10^{11} \text{ cm}^{-3}$.

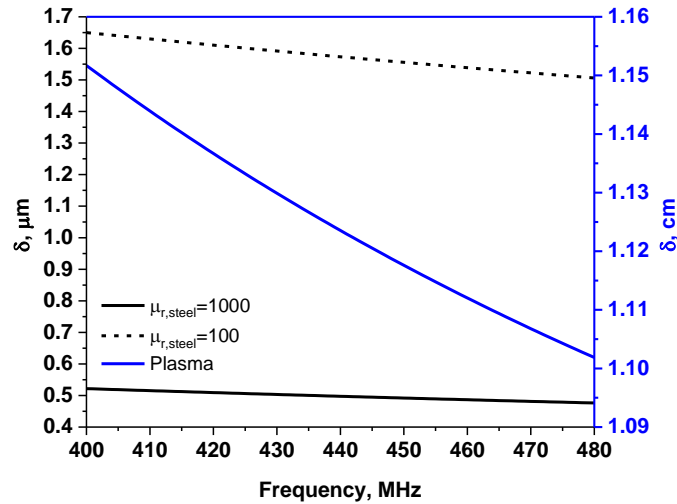


Figure 7.22. Calculated skin depths for the reference and plasma antenna.

The resistance of a given material is defined as

$$R = \frac{L}{\sigma A} \quad (7.15)$$

where L is its length, σ is its conductivity and A is its cross-sectional area. The plasma antenna length is 25 cm while the reference antenna length is 29 cm. For metals, the conductivity is $1/\rho$ while for plasmas it is

$$\sigma = \varepsilon_o \nu_m \frac{\omega_p^2}{\omega^2 + \nu_m^2} \quad (7.16)$$

where ε_o is the vacuum permittivity. A plot of the plasma antenna conductivity as well as its ratio with the reference antenna conductivity is shown in figure 7.22. For a given frequency, A depends on the skin depth and varies as

$$A = \frac{\pi(OD^2 - (OD - 2\delta)^2)}{4} \quad (7.17)$$

where OD is the outer diameter of the conducting medium. The OD is 25 mm and ~6.2 mm for the plasma antenna and reference antenna, respectively.

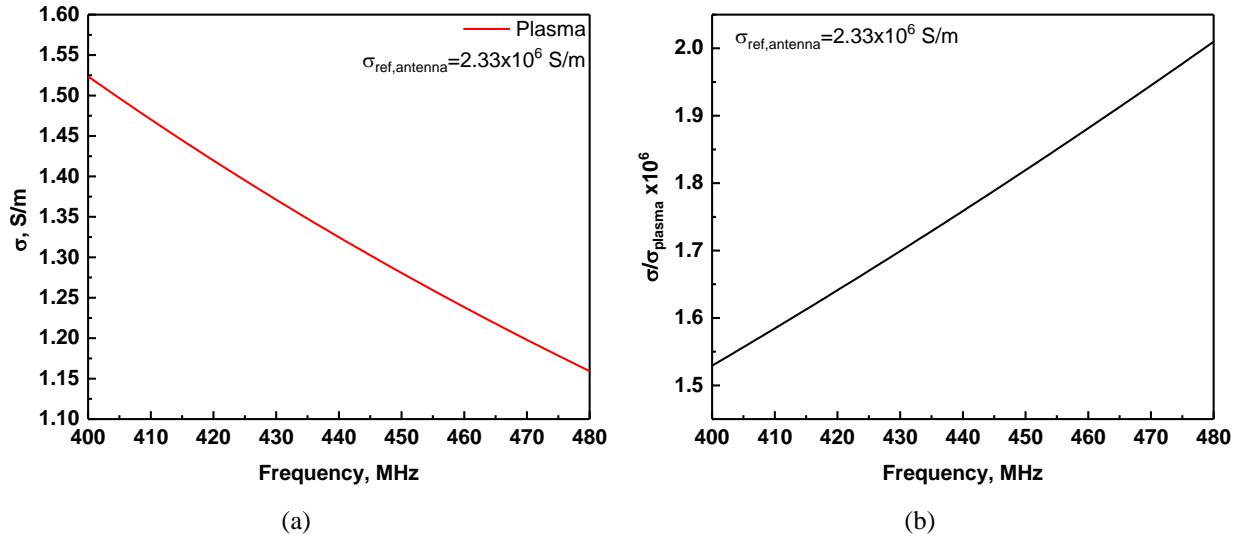


Figure 7.23. (a) The plasma antenna conductivity as a function of frequency and (b) the ratio of the reference antenna to the plasma antenna conductivity. The reference antenna conductivity is invariant with frequency.

After solving equations (7.12) and (7.13), the cross-sectional area is found from equation (7.17). For a given set of conditions, the plasma conductivity is found in equation (7.16). Equation (7.15) is solved with these parameters to give the resistance for both the metal and plasma antenna, a plot of which is presented in figure 7.24.

From figure 7.23 it is apparent that the conductivity of the reference antenna is $\approx 10^6$ times larger than the plasma antenna while from figure 7.22 its skin depth is $\approx 10^4$ times less. It is this large skin depth of the plasma antenna that compensates for its poor conductivity and gives an overall resistance within an 1-2 orders of magnitude of a metallic antenna. This is readily seen in figure 7.24 where the plasma antenna resistance is 30-100 times that of the reference antenna.

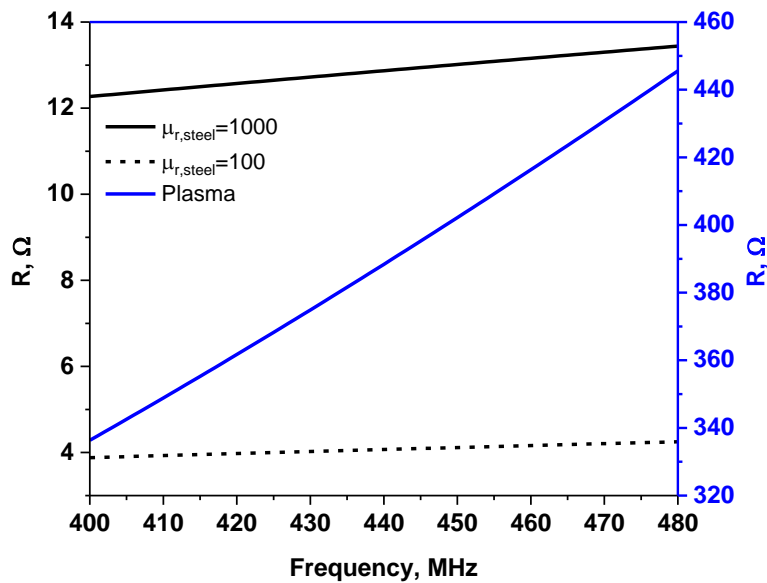


Figure 7.24. The calculated resistance for the reference and plasma antenna.

The relative gain between the two antennas can be estimated with the calculated values of resistances. The gain of an antenna is defined as

$$G = D_o \frac{R_r}{R_r + R_L} \quad (7.18)$$

where D_o is the antenna directivity, R_r is the antenna radiation resistance, and R_L is the loss resistance. Since both the plasma and reference antenna are omnidirectional quarter-wavelength monopoles, it is reasonable to assume that D_o and R_r are the same for both. For an ideal $\lambda/4$ monopole, $R_r=36.5 \Omega$ [88]. Taking the ratio of the reference antenna gain to the plasma antenna gain, the relative gain is determined in dB by

$$G_{Ref,Antenna} - G_{Plasma} = 10 \log \left(\frac{R_r + R_{Plasma}}{R_r + R_{ref}} \right) \quad (7.19)$$

where R_{Plasma} is the resistance of the plasma column and R_{ref} the resistance of the reference antenna. Using the calculated values of R_{Plasma} and R_{ref} shown in figure 7.24, a plot of relative gain is given in figure 7.25.

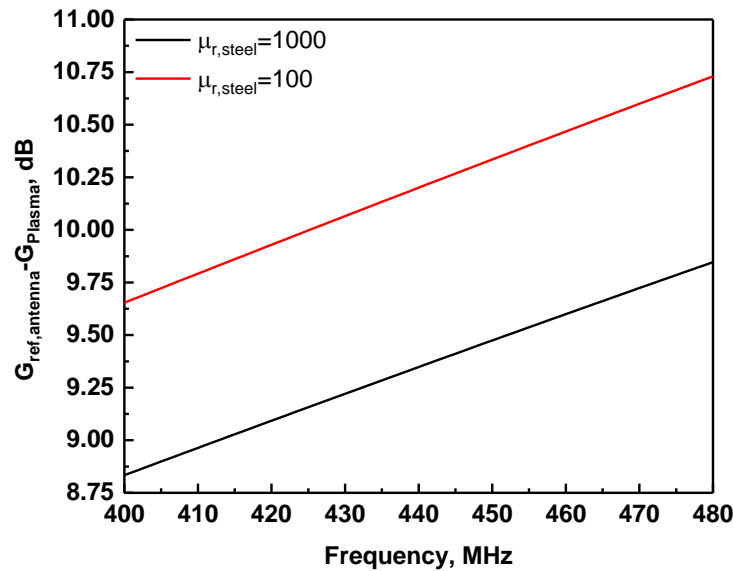


Figure 7.25. The estimated relative gain between the plasma and reference antenna.

As seen in figure 7.25, the plasma antenna gain is estimated to be about 10 dB lower than that of the reference steel antenna. This is almost within the combined error bar of the current gain measurements. Perhaps additional factors, such as impedance matching, may bring the plasma

antenna gain even closer to that of the reference antenna. To better understand this, more accurate experiments and electromagnetic simulations should be performed.

7.2.4 Measuring Variable Pressure Antenna n_e

The electron number density of the argon plasma as a function of power for excitation frequencies of 90 MHz and 500 MHz at pressures ranging from 0.3 to 1 Torr was measured using the microwave interferometry system described in [66]. A difference from that system is that in order ensure only the microwave beam travelling through the plasma is detected, a Mast MF11-0002-00 foam absorber was used. It was rolled to form two, 6-inch-long cylinders each with a ~2 cm internal diameter. Each cylinder was then wrapped in aluminum foil and placed into a 2-inch PVC pipe that acted as the housing. At one end of one PVC cylinder, a variable aperture was glued. As the microwave travels through the configuration shown in figure 7.26 diffraction around the Pyrex tube, beams traveling around the tube, and any other reflections of the microwave are absorbed.

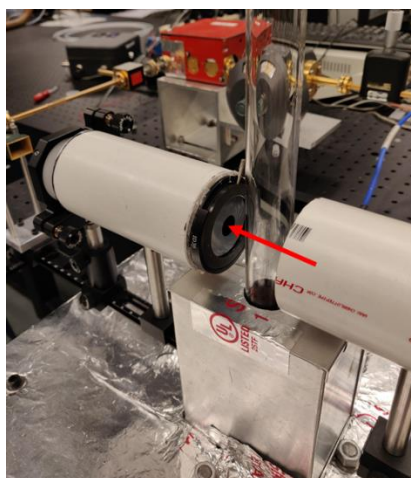


Figure 7.26. Microwave interferometer used to measure electron number density at $z=3.6$ cm above the shielding box. The red arrow shows the direction of the microwave beam.

Because the plasma column had a diameter of 2.3 cm, the aperture was set to 1 cm. This diameter was chosen to reduce diffraction effects through the aperture (microwave wavelength

~0.5 cm) and because any smaller diameter caused the measured signal to be too weak and uncertainty too high. Even with this aperture size, n_e measurements were found to be repeatable only within a factor of 2. All measurements were taken at a height of 3.6 cm above the shielding box. It was impossible to measure the axial distribution directly as neither the microwave interferometer nor the plasma antenna could be moved vertically.

In [9], Rayner et. al. showed that for a plasma sustained by a surface wave, the electron density scales with deposited power P_o as

$$n_e \approx A(p)\sqrt{P_o} \quad (7.20)$$

where $A(p)$ is a constant for a given pressure defined as

$$A(p) = \sqrt{\frac{2C\nu_m(p)}{K(p)}} \quad (7.21)$$

where C is an empirically determined constant related to the attenuation coefficient, ν_m is the momentum collision frequency, and $K(p)$ is a function depending on pressure (for a specific electron temperature) and geometry. If n_e and P_o can be experimentally measured, then plotting them in the form of equation (7.20) would allow for $A(p)$ to be inferred from the slope. ν_m can be estimated for a certain pressure. $K(p)$ can be calculated for a certain electron temperature and pressure with an electron number density balance. With these parameter, C can be determined and used to estimate the axial distribution of n_e as described in [9].

The argon plasma was sustained by a 90 MHz surface wave using both the AR and Aethercomm SSPA 0.020-1.000-100 amplifier and a 500 MHz surface wave using only the Aethercomm amplifier. The 500 MHz excitation frequency also required a Microlab S3-05N triple-stub tuner for impedance matching since the plasma could not otherwise be ignited or sustained. The tuner was used to ensure less than 1% of the incident power was reflected and

allowed for the deposited powers to be identical between the two excitation frequencies. The n_e results for both excitation frequencies are shown in figure 7.27a (90 MHz) and 7.27b (500 MHz). Table 7.1 presents the $A(p)$ extracted from a linear fit of figure 7.27.

For both excitation frequencies, the electron number density increases with gas pressure and applied power, as expected. The correlation between n_e and $\sqrt{P_o}$ is indeed linear as described in equation (7.20), and the slope, $A(p)$, increases with increasing pressure. $A(p)$ at 0.3 Torr is more than twice the magnitude when it was excited by the AR amplifier instead of the Aethercomm amplifier. While some of this difference can be attributed to experimental error, it may also be due to the performance of the Aethercomm amplifier which is plagued by strong higher order harmonics when there is a mismatched load, such as a plasma.

A comparison between the two excitation frequencies at the same pressure, same deposited power, and same amplifier source is shown in figure 7.28. With higher excitation frequency, the minimum electron number density to sustain surface wave propagation increases, as explained in chapter 1.1.2. Therefore, for the same deposited power and pressure, it is expected that n_e should be larger for higher excitation frequencies.

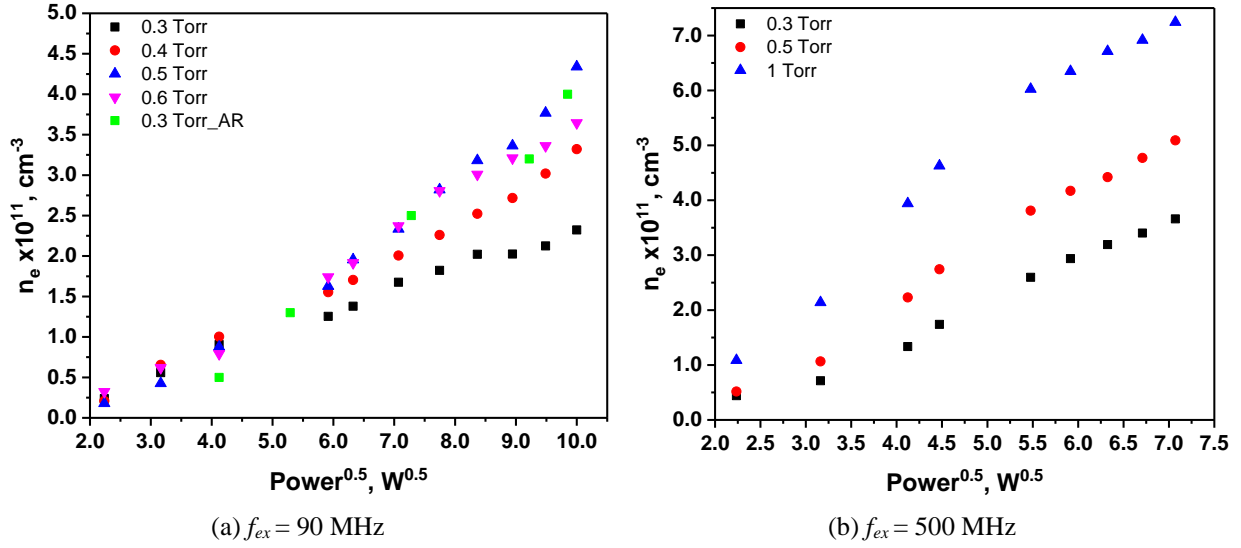


Figure 7.27. Measured electron number density of an argon plasma at the indicated pressure and excitation frequency as function of power. All data was taken with the Aethercomm amplifier, unless marked with AR which indicates the AR amplifier was used.

Table 7.1. The slope inferred from a linear fit of the data in figure 7.27.

$f_{ex}=90$ MHz			$f_{ex}=500$ MHz		
P	A(p)	\pm Fit Error	P	A(p)	\pm Fit Error
Torr	$\text{cm}^{-3}\text{W}^{-1/2}$	$\text{cm}^{-3}\text{W}^{-1/2}$	Torr	$\text{cm}^{-3}\text{W}^{-1/2}$	$\text{cm}^{-3}\text{W}^{-1/2}$
0.3	2.6	0.09	0.3	7.2	0.31
0.3*	5.7	0.42	0.5	9.9	0.33
0.4	3.8	0.09	1	13.0	0.75
0.5	5.3	0.21			
0.6	4.5	0.15			

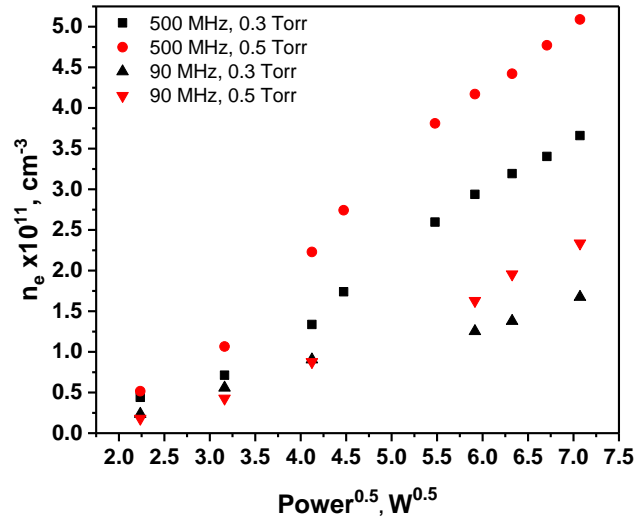


Figure 7.28. Comparison of the measured n_e in argon plasma between $f_{ex}=90$ MHz and $f_{ex}=500$ MHz at 0.3 Torr and 0.5 Torr.

8. FUTURE WORK

8.1 Fundamental Experiments

Initial experimentation and kinetic modeling of nanosecond pulses applied to parallel plate electrodes have yielded promising results. Microwave interferometry measurements indicate that a quasi-steady plasma with high n_e is achievable and kinetic modeling indicates that the presence of trace amounts of water vapor is enough to rapidly thermalize electrons in the afterglow of an argon plasma. These results provide a direction for future experimental work.

To minimize outgassing and better control gas composition, a new stainless steel vacuum chamber with electrodes embedded in an Teflon-insulated support structure has been assembled. The vacuum chamber assembly is shown in figure 8.1a while the electrode configuration in figure 8.1b. Plasma has successfully been sustained with nanosecond pulses. This configuration allows for voltage, current, gas composition (with an RGA), and electron number density to be measured.

The microwave interferometry measurements showed a significant portion of the probing signal travels around the plasma rather than through it because the longer path length of the beam allowed it to diverge more as it traveled through the vacuum chamber. Reflections of the signal from the metallic wall (something not present before) also contribute to the measured signal.

Mast MF11-0002-00 foam absorbers were purchased to mitigate the detection of stray signals (see chapter 7.2.3). With figure 8.2 showing the updated microwave system, as previously described, these absorbers were rolled into 6-inch-long cylinders and placed inside of 2-inch diameter PVC pipe. However, the path of the probing signal should be lengthened in order to physically fit it outside of the chamber. Alternative configurations in which the absorber is placed inside of the vacuum chamber should also be explored. The signal strength of the microwave beam should be increased regardless of the configuration used.

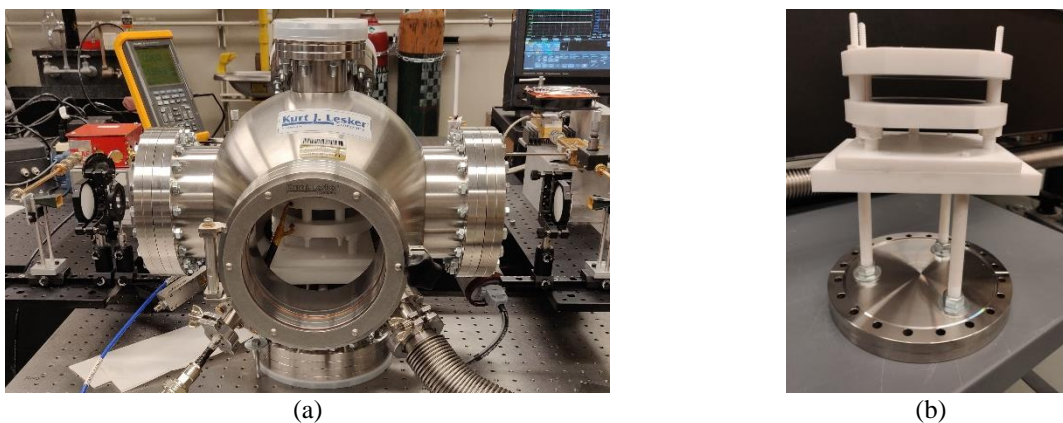


Figure 8.1. (a) Assembled stainless steel vacuum chamber system configured for microwave interferometry, voltage, and current measurements and (b) the teflon insulated electrode structure with embedded aluminum electrodes.

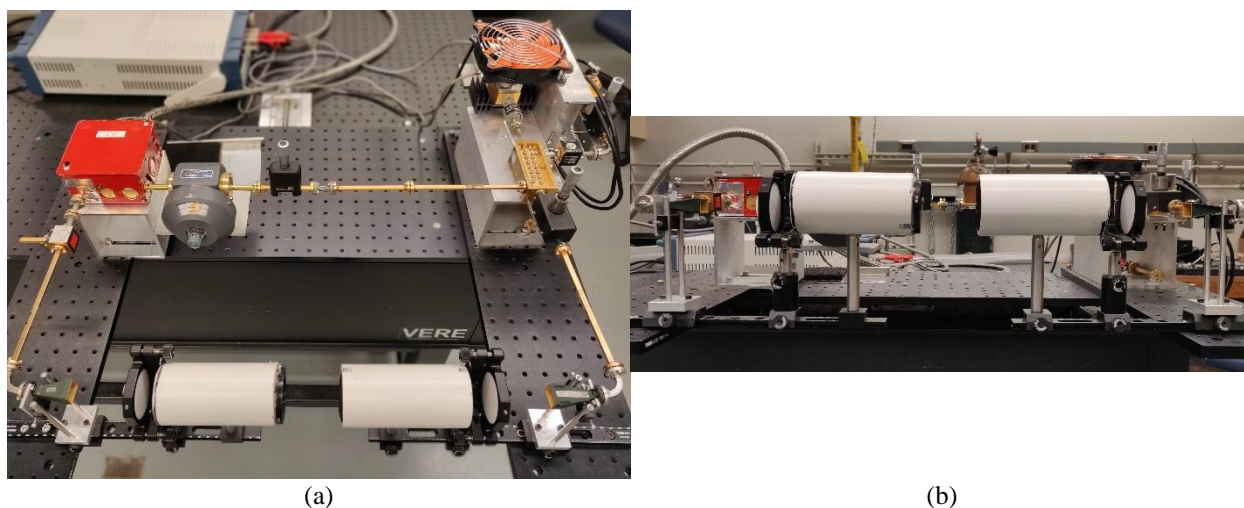


Figure 8.2. (a) Top and (b) front view of microwave interferometry system with 6 in. long foam absorbers inside of the PVC pipe.

After upgrading the microwave system, experiments should be conducted with the controlled introduction of trace amounts of water and nitrogen into argon gas. Parametric studies with nanosecond pulse voltages up to 10 kV and a pressure range of 100 mTorr to 10-30 Torr should be performed. Also, to improve our kinetic model of the plasma afterglow, single pulse experiments should be performed to ensure only neutral species exist before pulse onset. This would enable a better estimation of initial ion densities in the kinetic model.

Attempts to directly measure the collision frequency with the 58.1 GHz microwave interferometer and extract electron temperature were unsuccessful. Even with electron number densities $>10^{12} \text{ cm}^{-3}$ the attenuation of the microwave signal was still too weak to detect. Next steps should include using lower microwave frequencies, ω , to probe the plasma since attenuation is inversely proportional to ω^2 [52]. Alternative measurement techniques such as Thompson scattering, pulsed Langmuir probes, or optical emission spectroscopy should also be explored.

8.2 Plasma Antenna Future Work

Surface Wave Driven Plasma

With the experimental setup of figure 7.9 and 7.10, future tests to measure the antenna gain and resonant frequency should be performed at higher excitation frequencies. Under these conditions, impedance matching can be achieved with the triple-stub tuner and higher electron number densities can be generated. This should lead to better conductivity of the plasma column which in turn will improve overall antenna performance.

As described in chapter 1.1.2, the diameter of the Pyrex tube must satisfy the condition of $fR \leq 2 \text{ GHz-cm}$ for 0-mode surface wave propagation. With the existing tube diameter, this condition is only satisfied for $f_{ex} \leq 1.7 \text{ GHz-cm}$. Thinner tubes with internal diameter of $\sim 1.3 \text{ cm}$ and a glass-to-metal seal like that described in figure 10b should be used in order to facilitate a new maximum $f_{ex} = 3.1 \text{ GHz}$ and investigate the effects of tube diameter on antenna performance. Moreover, antenna height, gas type and pressure should also be varied to experimentally observe their impact.

Better coupling of the excitation and antenna signals to the plasma column should be explored. Improved coupler design should increase the efficiency with which plasma is generated

in the column and thereby increase the electron density produced for a given power and excitation frequency. The design of the shielding box and surrounding metal components may also affect this coupling. As such, experiments should be performed with the shielding box located below the ground plane and with a closed, electrodeless glass tube consisting of a known gas mixture at one pressure.

Nanosecond Pulsed Driven Plasma

Now a proof-of-principal monopole plasma antenna has been created, more focus should be placed on utilizing nanosecond pulses for sustaining a plasma column. Due to the coupling sleeve design and the glass thickness of the current variable pressure plasma antenna, a significant voltage drop occurs when igniting the plasma with the FPG 10-100MC2-10 pulser. The first step should be to apply pulses with higher voltages to this electrodeless design, such as with the FID FPG 10-1MHN pulser. The second should be to further investigate a direct-electrode design in which nanosecond pulses can be better utilized. Preliminary efforts on such a design have been successful with light bulbs with the form factor shown in figure 8.4. To reduce electrode degradation, parametric studies with voltage and pulse repetition frequency should be performed.

In conjunction with these efforts, a circuit (like the one described in figures 7.5 and 7.6) should be designed that can safely isolate the measurement device from the pulser's high voltage. A method to synchronize the measurement device with the pulse repetition rate should also be developed to allow for time-resolved noise data to be acquired in the plasma afterglow.

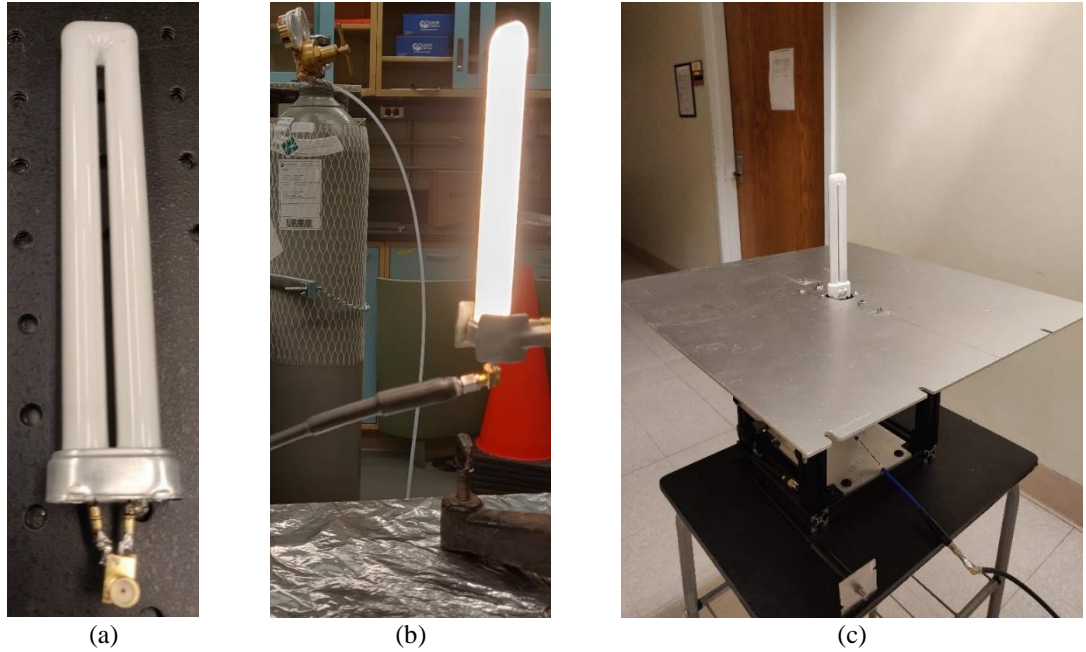


Figure 8.3. Preliminary tests with a nanosecond pulsed, direct electrode excitation. (a) antenna consists of an SMA connector soldered to the electrodes of a light bulb, (b) successful ignition with nanosecond pulses of this antenna, (c) setup with ground plane that will allow the light bulb to serve as a plasma antenna. A technique to make S_{11} measurements still needs to be developed.

APPENDIX A. CONDUCTIVITY AND PERMITTIVITY IN PURE ARGON

Conductivity and permittivity in pure argon was also explored. A simple kinetic model for pure argon was developed assuming a gas temperature of 300 K. The influence of pressures, p , tube diameter, D , and initial electron number densities, $n_{e,o}$, on σ and ϵ_r were explored over a range of frequencies of $f = 30$ MHz - 1 GHz. We considered $p=0.01$ -30 Torr, $n_{e,o}=1 \times 10^{10}$ - 1×10^{13} cm⁻³, and tube diameters of 0.4 and 2.5 cm. Quasi-neutrality was assumed, so $n_{i,o} = n_{e,o}$, and it was assumed the initial ions present after a pulse at $t=0$ are only Ar⁺. The electron temperature was determined as described in chapter 3.3 without considering the presence of H₂O. The only loss mechanisms considered were three-body recombination (R5), dissociative recombination (R2), Ar₂⁺ formation (R6), and ambipolar diffusion. These reactions with their rate constants are presented in table 3.1 in chapter 3.2. For ambipolar diffusion, the inverse characteristic diffusion length of $1/\Lambda_D^2 = 2.4/R^2$ was estimated using a Bessel approximation for a cylindrical geometry assuming the tube length is much larger than its radius, $L \gg R$ [43] and the mobility of Ar⁺, given in chapter 3.4, is used.

The model was solved in the same manner as described in Chapter 3 and equations 4.3-4.5 used to derive conductivity and permittivity in pure argon. The effects pressure and tube diameter on the calculated n_e decay profile are shown in figure A.1. As pressure is increased, the decay rate decreases up to 1 Torr and then increases beyond it. This occurs because at low pressures of 0.01 and 0.1 Torr, electrons are lost at the wall due to ambipolar diffusion which happens faster than three-body recombination with Ar⁺ and dissociative recombination with argon dimer ions since ion-conversion is a long process at such low pressures. These processes are still slow enough at 1 Torr that electrons are long living. With increasing pressure, the time for Ar⁺ to convert into Ar₂⁺ decreases since the number of argon neutrals increase. As the density of argon neutrals increase

with pressure, the collision frequency also increases, as seen in figure A.2, since there are now more molecules with which electrons can collide. In turn, the time for electrons to thermalize decreases with increasing ν_m meaning that the rate constants of Ar_2^+ dissociative recombination and three-body recombination will also increase, causing a more rapid decay in n_e .

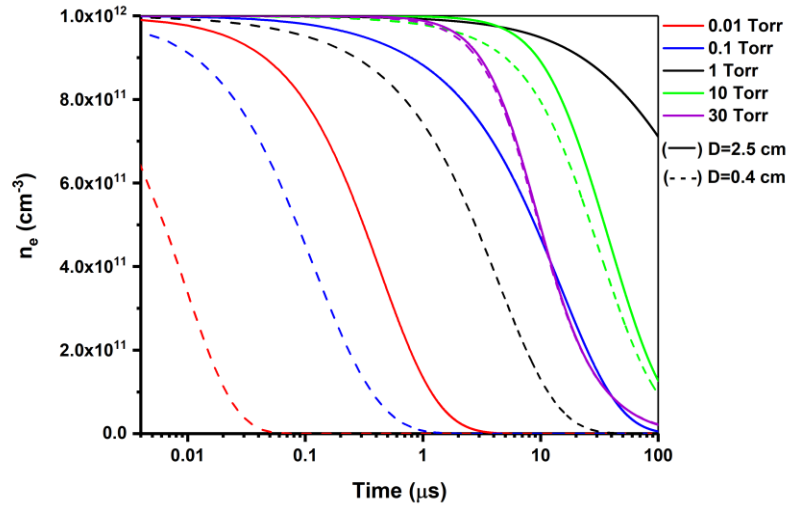


Figure A.1. The modeled decay of n_e in argon plasma afterglow for various pressures and tube diameters.

Figure A.1 also shows the effect of tube diameter on the decay rate of n_e . At $p < 10$ Torr, n_e decays several times faster when the tube diameter is 0.4 cm than for a tube diameter of 2.5 cm. The characteristic length scale for ambipolar diffusion is 10 times smaller at $D=0.4$ cm compared to $D=2.5$ cm. Therefore, electrons will more readily be lost to collisions to the wall. However, as pressure is increased, ambipolar diffusion is suppressed and the effect of tube diameter becomes negligible, as is clearly the case when $p=30$ Torr.

The conductivity and permittivity in the plasma afterglow for various radio frequencies is shown in figure A.3. At 30 MHz and 100 MHz, σ increases in the plasma afterglow, more than doubling in the case of 30 MHz. At 300 MHz it slightly decreases but experiences an order of magnitude drop in 100 μs at 1 GHz. At all radio frequencies simulated, ϵ_r becomes more negative,

falling by a factor of 10 at 30 MHz, 3 at 100 MHz, and 2 at 300 MHz. It is relatively constant at 1 GHz.

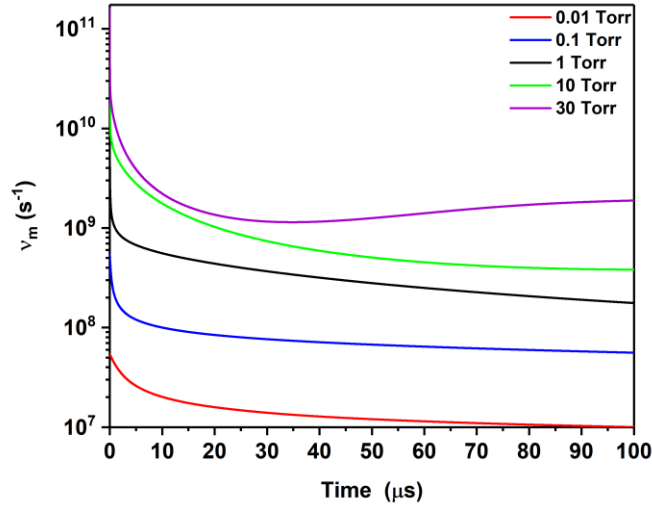


Figure A.2. Decay of v_m in the afterglow of argon plasma at various pressures.

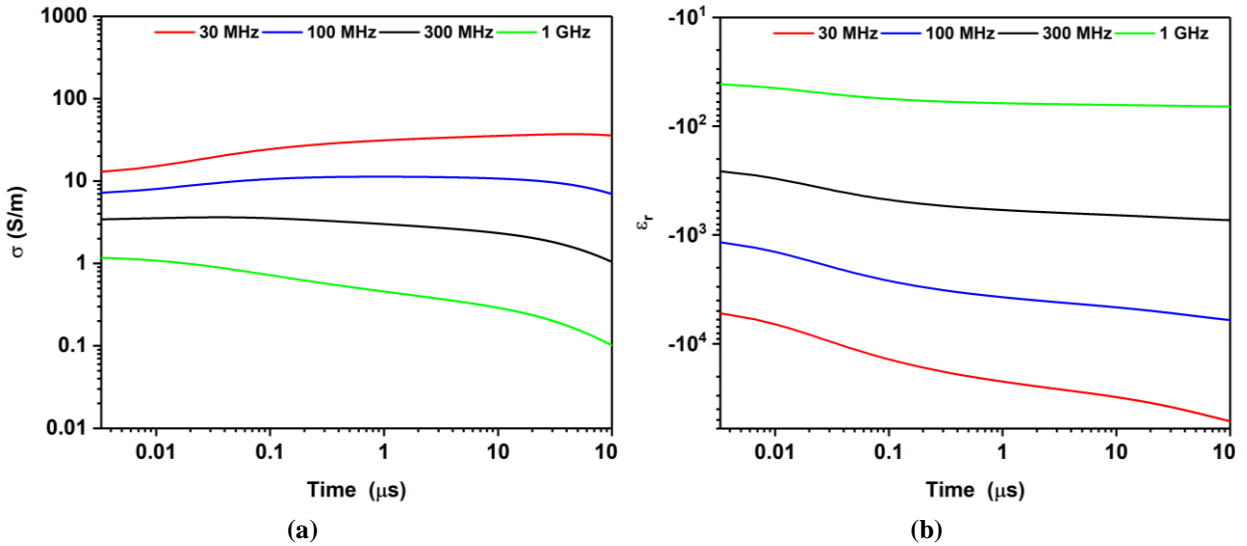


Figure A.3. The modeled (a) conductivity and (b) permittivity at various radio frequencies in the afterglow of argon plasma at $p=1$ Torr, $n_{e,0}=10^{12}$ cm^{-3} in a tube with $D=2.5$ cm.

For a fixed signal frequency of 30 MHz, the effect of pressure on conductivity and permittivity is shown in figure A.4. σ is maximized at 1 Torr due to that being the condition with slowest n_e decay rate, but the maximum increase in the afterglow occurs at 10 and 30 Torr where it rises by about an order of magnitude in 100 μs . This occurs due to the large collision frequencies,

and consequently faster rate of electron thermalization, at these pressures. The conductivity at 0.01 Torr is not shown since it is close to 0 in the plasma afterglow due to the rapid decay of electrons at this condition. ϵ_r is negative and decreases in the afterglow for all pressures except for 0.01 Torr. At this pressure, ϵ_r is positive and remains at ≈ 0.9 . The decrease in σ and increase in ϵ_r at $p=30$ Torr at $t \approx 40 \mu\text{s}$ corresponds to the increase in v_m at that time.

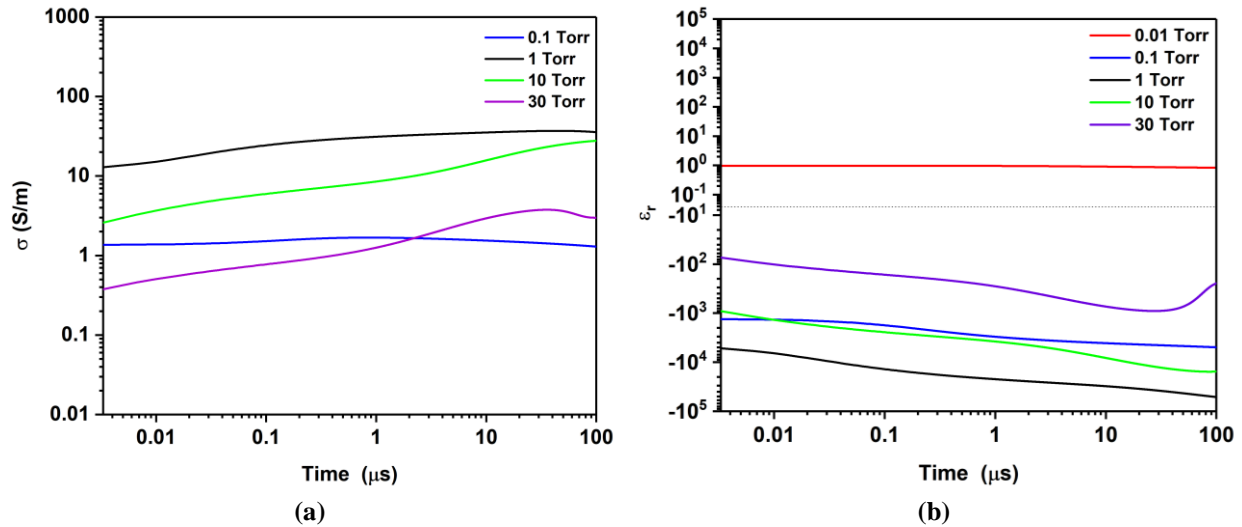


Figure A.4. The modeled (a) conductivity and (b) permittivity at various radio frequencies in the afterglow of argon plasma at $f=30$ MHz, $n_{e,o}=10^{12} \text{ cm}^{-3}$ at various pressures in a tube with $D=2.5$ cm.

Figure A.5 shows σ and ϵ_r in the afterglow at various initial electron number densities, at 1 Torr and signal frequency of 30 MHz and 1 GHz. Compared to 30 MHz, an order of magnitude larger n_e must be reached for a 1 GHz signal to achieve the same conductivity. ϵ_r is negative for all of the initial electron densities at both signal frequencies except for at $n_{e,o}=10^{10} \text{ cm}^{-3}$ at 1 GHz where it is positive.

From the results, it is observed that the conductivity in the plasma afterglow can double at signal frequencies of 30 MHz and increase or remain constant for frequencies up to ≈ 300 MHz. This makes it difficult to operate at frequencies approaching 1 GHz since no benefit of the afterglow increase in σ is achieved implying operation is only possible at very high electron

densities. Of the pressures modeled, conductivity is maximized at 1 Torr but the largest increase in σ over 100 μs period at 10 Torr. Therefore, an optimum pressure that both maximizes and provides the greatest change σ after a pulse should be between 1-10 Torr.

Most conditions yield a result where the plasma has very large negative values of ϵ_r , implying that it will be able to sustain a surface wave for plasma antenna purposes. The positive permittivity present at 1 GHz for $n_{e,o}=10^{10} \text{ cm}^{-3}$ as seen figure A.5d reveals that operating at such high signal frequencies, one can easily shift from a positive to negative permittivity by simply increasing the number of electrons produced in a pulse. However, conditions in which ϵ_r is positive cannot sustain a surface wave disabling the ability to capacitively couple to any plasma antenna.

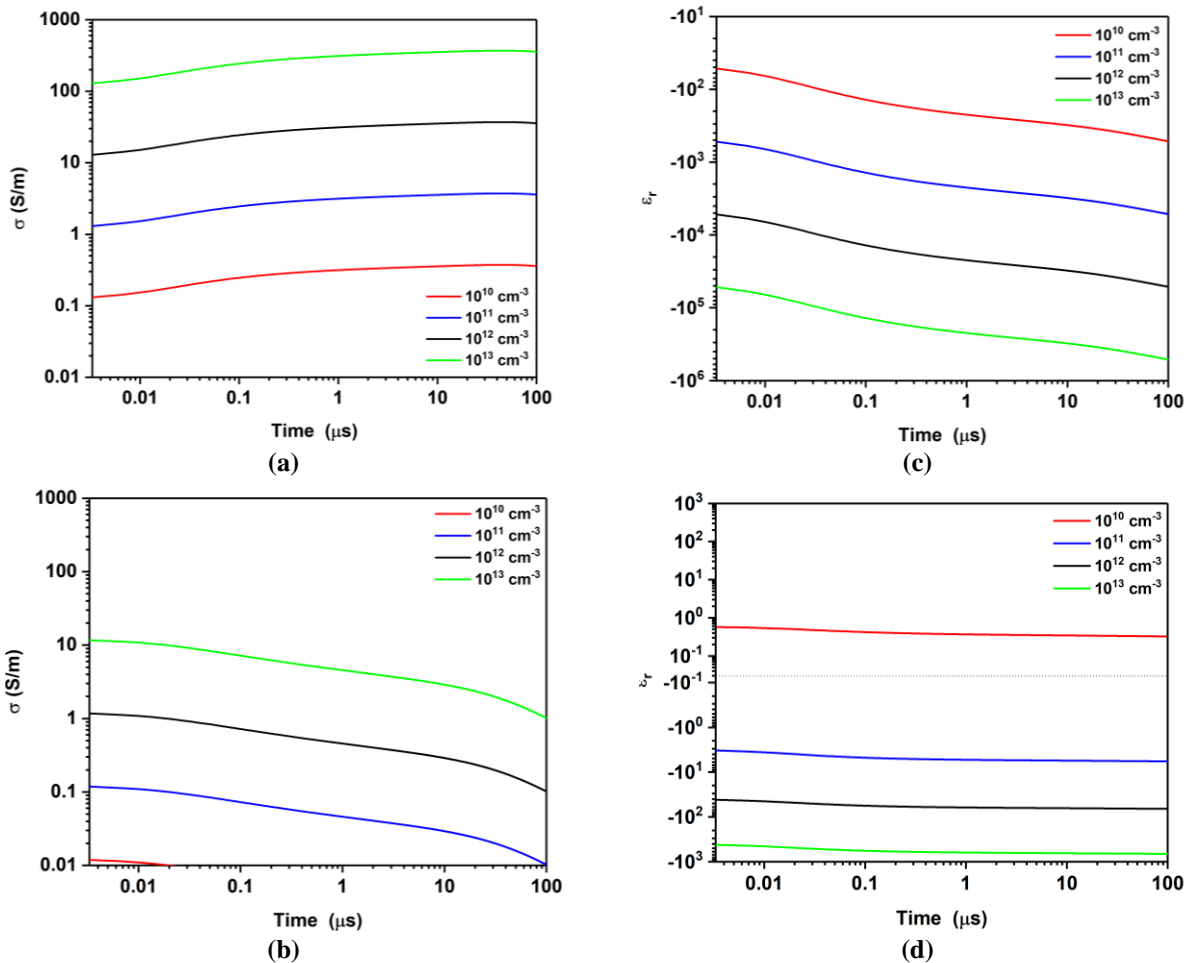


Figure A.5. The modeled (a,b) conductivity and (c,d) permittivity at various $n_{e,o}$ in the afterglow of argon plasma at 1 Torr in a tube with $D=2.5 \text{ cm}$. (a) and (c) $f=30 \text{ MHz}$, (b) and (d) $f=1 \text{ GHz}$.

APPENDIX B. ARGON IONIZATION COST VOLTAGE AND CURRENT MEASUREMENTS

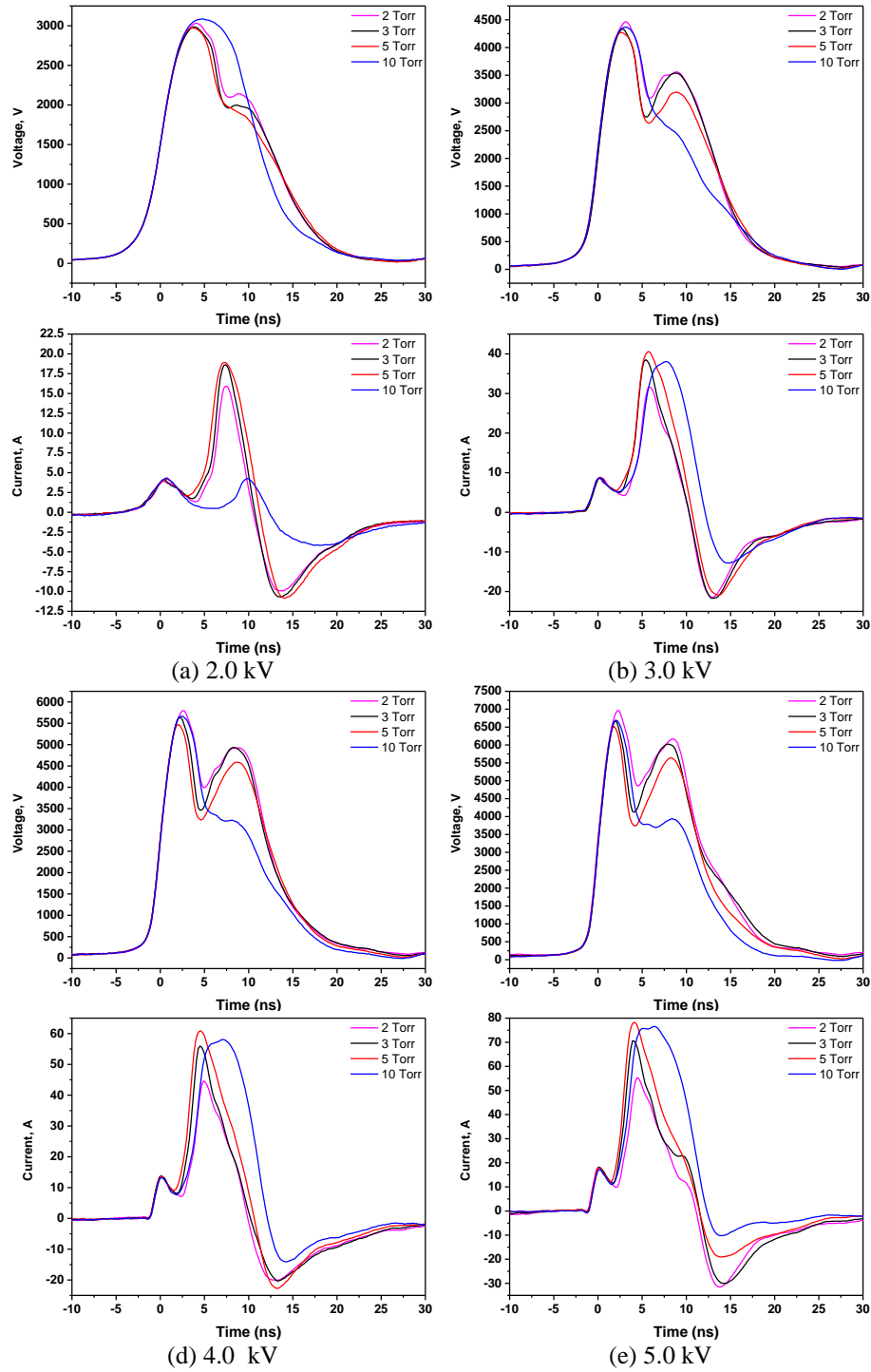


Figure B.1. Reconstructed applied voltage and current profiles for indicated commanded voltage pulsed at a repetition frequency of 0.1 kHz onto argon plasma at the indicated pressures.

REFERENCES

- [1] J. Hettinger, "Aerial Conductor for Wireless Signaling and Other Purposes," 1309031, 1919.
- [2] L. M. Vallese, "Laser Beam Antenna," 3404403, 1966.
- [3] J. Vaill, "Laser Beam Techniques," 3719829, 1973.
- [4] M. Moisan, A. Shivarov, and A. Trivepiece, "Experimental investigations of the propagation of surface waves along a plasma column," *Plasma Physics*, vol. 24, no. 11, 1982.
- [5] Y. I. Burykin, S. M. Levitskiy, and V. G. Martynenko, "The Radiation of Electromagnetic Waves by a Variable Cross Section Cylindrical Plasma Waveguide," *Radio Eng. Electron. physics*, vol. 20, pp. 86–91, 1975.
- [6] K. M. Chen and C. C. Lin, "Enhanced Radiation from a Plasma-Imbedded Antenna," *Proc. IEEE*, vol. 56, no. 9, pp. 1595–1597, 1968.
- [7] W. Kang, M. Rader, and I. Alexeff, "A Conceptual Study of Stealth Plasma Antenna," in *A Conceptual Study of Stealth Plasma Antenna*, 1996, p. 261.
- [8] J. Zhao, Y. Chen, Y. Sun, H. Wu, Y. Liu, and Q. Yuan, "Plasma antennas driven by 5-20 kHz AC power supply," *AIP Adv.*, vol. 5, no. 12, 2015.
- [9] J. P. Rayner, A. P. Whichello, and A. D. Cheetham, "Physical Characteristics of Plasma Antennas," *IEEE Trans. Plasma Sci.*, vol. 32, no. 1, pp. 269–281, 2004.
- [10] T. Naito *et al.*, "Theoretical and experimental investigation of plasma antenna characteristics on the basis of gaseous collisionality and electron density," *Jpn. J. Appl. Phys.*, vol. 54, no. 1, p. 016001, 2015.
- [11] T. Naito, S. Yamaura, Y. Fukuma, and O. Sakai, "Radiation characteristics of input power from surface wave sustained plasma antenna," *Phys. Plasmas*, vol. 23, no. 9, 2016.
- [12] G. G. Borg *et al.*, "Plasmas as antennas: Theory, experiment and applications," *Phys. Plasmas*, vol. 7, no. 5, pp. 2198–2202, 2000.
- [13] I. Alexeff, T. Anderson, S. Parameswaran, E. P. Pradeep, J. Hulloli, and P. Hulloli, "Plasma Antennas," *Ieee Trans. Plasma Sci.*, vol. 34, no. 2, pp. 166–172, 2006.
- [14] F. Sadeghikia, M. Talafi Noghani, and M. R. Simard, "Experimental study on the surface wave driven plasma antenna," *AEU - Int. J. Electron. Commun.*, vol. 70, no. 5, pp. 652–656, 2016.

- [15] N. G. Gusein-Zade, I. M. Minaev, A. A. Rukhadze, and K. Z. Rukhadze, "Physical principles of plasma antenna operation," *J. Commun. Technol. Electron.*, vol. 56, no. 10, pp. 1207–1211, 2011.
- [16] H. M. Zali *et al.*, "A monopole fluorescent tube antenna with Wi-Fi Router," in *2014 21st International Conference on Telecommunications, ICT 2014*, 2014, no. December, pp. 358–362.
- [17] S. S. Golazari, N. Amiri, and F. H. Kashani, "Design, simulation and measurement of loop plasma antenna in UHF band," in *2016 24th Telecommunications Forum (TELFOR)*, 2016, pp. 1–4.
- [18] V. Kumar, M. Mishra, and N. K. Joshi, "Study of a Fluorescent Tube as Plasma Antenna.," *Prog. Electromagn. Res. Lett.*, vol. 24, no. May, pp. 17–26, 2011.
- [19] Z. Longgen, C. Lihui, and Z. Zhigang, "Study on the gain of plasma antenna," in *ISAPE 2008 - The 8th International Symposium on Antennas, Propagation and EM Theory Proceedings*, 2008, pp. 222–224.
- [20] I. Alexeff, T. Anderson, E. Farshi, N. Karnam, and N. R. Pulasani, "Recent results for plasma antennas," *Phys. Plasmas*, vol. 15, no. 5, p. 057104, May 2008.
- [21] R. Kumar and D. Bora, "A reconfigurable plasma antenna," *J. Appl. Phys.*, vol. 107, no. 5, p. 053303, Mar. 2010.
- [22] R. Kumar and D. Bora, "Wireless communication capability of a reconfigurable plasma antenna," *J. Appl. Phys.*, vol. 109, no. 6, p. 063303, Mar. 2011.
- [23] Z. Anshi, C. Zili, W. Jianbin, and Z. Yunhui, "Study on Pattern Reconfiguration of Plasma Antenna Excited by Surface Wave," *TELKOMNIKA Indones. J. Electr. Eng.*, vol. 12, no. 9, pp. 6658–6666, 2014.
- [24] V. V. Ovshyanikov, "Broadband Microwave Emitter on a Basis of Gas Discharge Plasma *," *Telecommun. Radio Eng.*, vol. 61, no. 10, pp. 822–831, 2004.
- [25] T. Anderson, "Theory, measurements, and prototypes of plasma antennas," in *2014 IEEE Antennas and Propagation Society International Symposium (APSURSI)*, 2014, pp. 567–568.
- [26] T. Anderson *et al.*, "An operating intelligent plasma antenna," in *2007 16th IEEE International Pulsed Power Conference*, 2007, pp. 353–356.
- [27] D. C. Jenn, "Plasma Antennas: Survey of Techniques and the Current State of the Art," 2003.

- [28] R. Kumar, S. V. Kulkarni, and D. Bora, “Cylindrical stationary striations in surface wave produced plasma columns of argon,” *Phys. Plasmas*, vol. 14, no. 12, 2007.
- [29] Y. Brelet *et al.*, “Radiofrequency plasma antenna generated by femtosecond laser filaments in air,” *Appl. Phys. Lett.*, vol. 101, no. 26, pp. 2008–2011, 2012.
- [30] M. M. Abbasi and S. Asadi, “Theoretical and experimental investigations of surface-waves plasma column and microwave plasma source for applications in reconfigurable plasma antenna,” *Indian J. Sci. Technol.*, vol. 59, no. 4, pp. 806–811, 2016.
- [31] G. Cerri, R. De Leo, V. Mariani Primiani, and P. Russo, “Measurement of the properties of a plasma column used as a radiating element,” *IEEE Trans. Instrum. Meas.*, vol. 57, no. 2, pp. 242–247, 2008.
- [32] P. Russo, V. M. Primiani, G. Cerri, R. De Leo, and E. Vecchioni, “Experimental Characterization of a Surface-Wave Fed Plasma Antenna,” *IEEE Trans. Antennas Propag.*, vol. 59, no. 2, pp. 425–433, Feb. 2011.
- [33] M. Moisan, J. Margot, and Z. Zakrzewski, “Surface Wave Plasma Sources,” in *High Density Plasma Sources*, O. Popov, Ed. William Andrew Publishing, 1995, pp. 191–250.
- [34] A. W. Trivelpiece and R. W. Gould, “Space charge waves in cylindrical plasma columns,” *J. Appl. Phys.*, vol. 30, no. 11, pp. 1784–1793, 1959.
- [35] A. Shivarova and I. Zhelyazkov, “Surface waves in a homogeneous plasma sharply bounded by a dielectric,” *Plasma Phys.*, vol. 20, no. 10, pp. 1049–1073, 1978.
- [36] C. M. Ferreira, “Theory of a plasma column sustained by a surface wave,” *J. Phys. D. Appl. Phys.*, vol. 14, no. 10, pp. 1811–1830, Oct. 1981.
- [37] Z. Zakrzewski, M. Moisan, V. M. M. Glaude, C. Beaudry, and P. Leprince, “Attenuation of a surface wave in an unmagnetized R.F. plasma column,” *Plasma Phys.*, vol. 19, no. 2, pp. 77–83, Feb. 1977.
- [38] M. Moisan and Z. L. B.-M. Zakrzewski, “Plasma sources based on the propagation of electromagnetic surface waves,” *J. Phys. D. Appl. Phys.*, vol. 24, no. 7, p. 1025, 1991.
- [39] N. N. Bogachev, I. L. Bogdankevich, N. G. Gusein-zade, and A. A. Rukhadze, “Surface wave and linear operating mode of a plasma antenna,” *Plasma Phys. Reports*, vol. 41, no. 10, pp. 792–798, 2015.
- [40] M. Moisan, C. Beaudry, and P. Leprince, “A small microwave plasma source for long column production without magnetic field,” *IEEE Trans. Plasma Sci.*, vol. 3, no. 2, pp. 55–59, 1975.

- [41] G. G. Borg, J. H. Harris, D. G. Miljak, and N. M. Martin, "Application of plasma columns to radiofrequency antennas," *Appl. Phys. Lett.*, vol. 74, no. 22, pp. 3272–3274, 1999.
- [42] R. Kumar and D. Bora, "Experimental study of parameters of a plasma antenna," *Plasma Sci. Technol.*, vol. 12, no. 5, pp. 592–600, 2010.
- [43] Y. P. Raizer, *Gas Discharge Physics*. Springer-Verlag Berlin Heidelberg, 1991.
- [44] T. R. Anderson, "Electromagnetic noise from frequency driven and transient plasmas," *IEEE Int. Symp. Electromagn. Compat.*, vol. 1, pp. 498–501, 2002.
- [45] S. O. Macheret, M. N. Shneider, and R. C. Murray, "Ionization in strong electric fields and dynamics of nanosecond-pulse plasmas," *Phys. Plasmas*, vol. 13, no. 2, pp. 1–10, 2006.
- [46] I. V. Adamovich *et al.*, "Plasma assisted ignition and high-speed flow control: Non-thermal and thermal effects," *Plasma Sources Sci. Technol.*, vol. 18, no. 3, 2009.
- [47] S. M. Starikovskaia, "Plasma-assisted ignition and combustion: Nanosecond discharges and development of kinetic mechanisms," *J. Phys. D. Appl. Phys.*, vol. 47, no. 35, 2014.
- [48] D. F. Opaits *et al.*, "Experimental investigation of dielectric barrier discharge plasma actuators driven by repetitive high-voltage nanosecond pulses with dc or low frequency sinusoidal bias," *J. Appl. Phys.*, vol. 104, no. 4, 2008.
- [49] A. Y. Starikovskii, A. A. Nikipelov, M. M. Nudnova, and D. V. Roupasov, "SDBD plasma actuator with nanosecond pulse-periodic discharge," *Plasma Sources Sci. Technol.*, vol. 18, no. 3, 2009.
- [50] G. Correale, T. Michelis, D. Ragni, M. Kotsonis, and F. Scarano, "Nanosecond-pulsed plasma actuation in quiescent air and laminar boundary layer," *J. Phys. D. Appl. Phys.*, vol. 47, no. 10, 2014.
- [51] A. Klochko, "Excited species chemistry in homogeneous nanosecond discharges with high specific energy deposition," *École Doctorale de l'École Polytechnique, Laboratoire de Physique des Plasmas*, 2014.
- [52] M. Heald and C. Wharton, *Plasma Diagnostics with Microwaves*. New York: Wiley, 1965.
- [53] M. A. Cappelli, N. Gascon, and W. A. Hargus, "Millimetre wave plasma interferometry in the near field of a Hall plasma accelerator," *J. Phys. D. Appl. Phys.*, vol. 39, no. 21, pp. 4582–4588, 2006.
- [54] C. C. Dobson, J. E. Jones, and D. G. Chavers, "Instrument reflections and scene amplitude modulation in a polychromatic microwave quadrature interferometer," *Rev. Sci. Instrum.*, vol. 75, no. 3, pp. 674–683, 2004.

- [55] G. Neumann, U. Bänziger, M. Kammeyer, and M. Lange, “Plasma-density measurements by microwave interferometry and Langmuir probes in an rf discharge,” *Rev. Sci. Instrum.*, vol. 64, no. 1, pp. 19–25, 1993.
- [56] L. J. Overzet and M. B. Hopkins, “Comparison of electron-density measurements made using a Langmuir probe and microwave interferometer in the gaseous electronics conference reference reactor,” *J. Appl. Phys.*, vol. 74, no. 7, pp. 4323–4330, 1993.
- [57] K. Akhtar, J. E. Scharer, S. M. Tysk, and E. Kho, “Plasma interferometry at high pressures,” *Rev. Sci. Instrum.*, vol. 74, no. 2, pp. 996–1001, 2003.
- [58] N. L. Aleksandrov, S. V. Kindysheva, A. A. Kirpichnikov, I. N. Kosarev, S. M. Starikovskaia, and A. Y. Starikovskii, “Plasma decay in N₂, CO₂ and H₂O excited by high-voltage nanosecond discharge,” *J. Phys. D. Appl. Phys.*, vol. 40, no. 15, pp. 4493–4502, 2007.
- [59] R. C. Murray, S. H. Zaidi, M. S. O. Macheret, and R. B. Miles, “Microwave diagnostics of a repetitive, short-pulse-sustained, weakly ionized, air plasma under the influence of a magnetic field,” *IEEE Trans. Plasma Sci.*, vol. 34, no. 3 PART 3, pp. 1004–1012, 2006.
- [60] M. Mesko *et al.*, “Electron density measurements in afterglow of high power pulsed microwave discharge,” *Plasma Sources Sci. Technol.*, vol. 13, no. 4, pp. 562–568, 2004.
- [61] M. Laroussi, “Relationship between the number density and the phase shift in microwave interferometry for atmospheric pressure plasmas,” *Int. J. Infrared Millimeter Waves*, vol. 20, no. 8, pp. 1501–1508, 1999.
- [62] F. J. Mehr and M. A. Biondi, “Electron-temperature dependence of electron-ion recombination in Argon,” *Phys. Rev.*, vol. 176, no. 1, pp. 322–326, 1968.
- [63] Y. Shiu and M. A. Biondi, “Dissociative recombination in argon: Dependence of the total rate coefficient and excited-state production on electron temperature,” *Phys. Rev. A*, vol. 17, no. 3, pp. 868–872, 1978.
- [64] W. F. Liu and D. C. Conway, “Ion--molecule reactions in Ar at 296, 195, and 77° K,” *J. Chem. Phys.*, vol. 62, no. 8, pp. 3070–3073, 1975.
- [65] T. Anderson, *Plasma Antennas*. Artech House, 2011.
- [66] V. Podolsky, A. Khomenko, and S. Macheret, “Time-resolved measurements of electron number density in argon and nitrogen plasmas sustained by high-voltage, high repetition rate, nanosecond pulses,” *Plasma Sources Sci. Technol.*, vol. 27, no. 10, p. 10LT02, 2018.
- [67] R. S. Moss, “Breakdown Measurements in Argon and Xenon Applicable To Metal Halide High Intensity Discharge Lamps,” University of Illinois at Urbana-Champaign, 2002.

- [68] H. W. Ellis, P. Y. Pai, E. W. McDaniel, E. A. Mason, and L. A. Viehland, "Transport Properties of Gaseous Ions Over a Wide Energy Range," *At. Data Nucl. Data Tables*, no. 3, pp. 177–210, 1976.
- [69] A. Tavant and M. A. Lieberman, "Hybrid global model of water cluster ions in atmospheric pressure Ar/H₂O RF capacitive discharges," *J. Phys. D. Appl. Phys.*, vol. 49, no. 46, p. 465201, 2016.
- [70] T. Shirafuji and T. Murakami, "Contribution of electrons, Ar(3P_{0,2}), H₂O⁺, and H₃O⁺ to production of OH(A₂Σ⁺) in a micro- dielectric barrier discharge of Ar/H₂O," *Jpn. J. Appl. Phys.*, vol. 54, no. 01AC03, 2015.
- [71] See, "Biagi-v7.1 database, www.lxcat.net, retrieved on May 8, 2018."
- [72] J. Tennyson, N. F. Zobov, R. Williamson, O. L. Polyansky, and P. F. Bernath, "Experimental energy levels of the water molecule," *J. Phys. Chem. Ref. Data*, vol. 30, no. 3, pp. 735–831, 2001.
- [73] P. F. Zittel and D. E. Masturzo, "Vibrational relaxation of H₂O from 295 to 1020 K," *J. Chem. Phys.*, vol. 90, no. 2, pp. 977–989, 1989.
- [74] Y. Celik, T. V. Tsankov, M. Aramaki, S. Yoshimura, D. Luggenhölscher, and U. Czarnetzki, "Electron cooling in decaying low-pressure plasmas," *Phys. Rev. E - Stat. Nonlinear, Soft Matter Phys.*, vol. 85, no. 4, pp. 1–6, 2012.
- [75] F. X. Liu, X. M. Guo, and Y. K. Pu, "Electron cooling and plasma density decay in early afterglow of low pressure argon plasmas," *Plasma Sources Sci. Technol.*, vol. 24, no. 3, p. 34013, 2015.
- [76] R. P. McEachran and A. D. Stauffer, "Momentum transfer cross sections for the heavy noble gases," *Eur. Phys. J. D*, vol. 68, no. 6, 2014.
- [77] Y. Itikawa and N. Mason, "Cross sections for electron collisions with water molecules," *J. Phys. Chem. Ref. Data*, vol. 34, no. 1, pp. 1–22, 2005.
- [78] N. A. Dyatko *et al.*, "Experimental and theoretical study of the transition between diffuse and contracted forms of the glow discharge in argon," *J. Phys. D. Appl. Phys.*, vol. 41, no. 5, p. 055204, 2008.
- [79] L. A. Viehland and E. A. Mason, "Transport properties of gaseous ions over a wide energy range. Part IV.pdf," *At. Data Nucl. Data Tables*, vol. 60, no. 1, pp. 37–95, 1995.
- [80] I. V. Adamovich, M. Nishihara, I. Choi, M. Uddi, and W. R. Lempert, "Energy coupling to the plasma in repetitive nanosecond pulse discharges," *Phys. Plasmas*, vol. 16, no. 11, p. 113505, 2009.

- [81] S. M. Starikovskaia, "Plasma assisted ignition and combustion," *J. Phys. D. Appl. Phys.*, vol. 39, no. 16, 2006.
- [82] A. Semnani *et al.*, "Low temperature plasma for tunable resonant attenuation," *IEEE MTT-S Int. Microw. Symp. Dig.*, vol. 2016-Augus, no. 1, pp. 3–6, 2016.
- [83] S. O. Macheret, M. N. Shneider, and R. B. Miles, "Modeling of air plasma generation by repetitive high-voltage nanosecond pulses," *IEEE Trans. Plasma Sci.*, vol. 30, no. 3, pp. 1301–1314, 2002.
- [84] S. O. Macheret, M. N. Shneider, R. B. Miles, and R. J. Lipinski, "Electron-beam-generated plasmas in hypersonic magnetohydrodynamic channels," *AIAA J.*, vol. 39, no. 6, pp. 1127–1138, 2001.
- [85] V. Podolsky and S. Macheret, "Plasmas sustained by repetitive nanosecond pulses: recombination mechanisms in Ar with trace amounts of H₂O," *Plasma Sources Sci. Technol.*, vol. 28, no. 5, p. 055008, 2019.
- [86] X. Wang and A. Shashurin, "Study of atmospheric pressure plasma jet parameters generated by DC voltage driven cold plasma source," *J. Appl. Phys.*, vol. 122, no. 6, pp. 1–6, 2017.
- [87] X. Wang, P. Stockett, R. Jagannath, S. Bane, and A. Shashurin, "Time-resolved measurements of electron density in nanosecond pulsed plasmas using microwave scattering," *Plasma Sources Sci. Technol.*, vol. 27, no. 7, 2018.
- [88] C. A. Balanis, *Antenna Theory Analysis and Design*, Third. Hoboken, New Jersey: John Wiley & Sons, Inc., 2005.

PUBLICATIONS

- 1) V. Podolsky, A. Khomenko, and S. Macheret, "Time-resolved measurements of electron number density in argon and nitrogen plasmas sustained by high-voltage, high repetition rate, nanosecond pulses," *Plasma Sources Sci. Technol.*, vol. 27, no. 10, p. 10LT02, 2018.
- 2) V. Podolsky and S. Macheret, "Plasmas sustained by repetitive nanosecond pulses: recombination mechanisms in Ar with trace amounts of H₂O," *Plasma Sources Sci. Technol.*, vol. 28, no. 5, p. 055008, 2019.
- 3) T. Piskin, V. Podolsky, J. Poggie, S. Macheret, "Challenges in numerical simulation of nanosecond-pulse discharges," *J. Phys. D: Appl. Phys.*, vol. 52, p. 304002, 2019.
- 4) V. Podolsky and S. Macheret, "The conductivity and permittivity of a plasma in the pulse afterglow," (manuscript in preparation).
- 5) V. Podolsky, A. Khomenko, and S. Macheret, "Ionization costs in air and argon plasmas sustained by high voltage, repetitive nanosecond pulses," (manuscript in preparation).
- 6) V. Podolsky, A. Semnani and S. Macheret, "Gain reconfigurability of a resonant plasma antenna sustained by a CW surface wave discharge," (manuscript in preparation).